

Theoretical Studies of Catalyst Structure and Kinetics in the MTO Process

Zur Erlangung des akademischen Grades eines
DOKTORS DER NATURWISSENSCHAFTEN
(Dr. rer. nat.)

von der KIT-Fakultät für Chemie und Biowissenschaften
des Karlsruher Instituts für Technologie (KIT)

genehmigte
DISSERTATION
von

M.Sc. Ashley Smith

1. Referent: Prof. Dr. Felix Studt
2. Referentin: apl. Prof. Dr. Karin Fink
Tag der mündlichen Prüfung: 20.07.2021

Abstract

Crude oil is the cornerstone of the global economy and chemical industry. The knowledge that it is a non-renewable resource has driven a decades long search for alternative ways to produce chemical feedstocks and fuels from renewable sources. The methanol-to-hydrocarbons (MTH) process which can be tuned towards olefins in the methanol-to-olefins (MTO) process and gasoline in the methanol-to-gasoline process is a promising contender in this search. The process takes place in zeolite catalysts and is already viable on the industrial scale. It is highly tuneable and depends intricately on factors such as catalyst strength, structure and shape. Crucially the input methanol itself can easily be derived via the syngas route from many different gasifiable carbon sources such as biomass, coal and natural gas.

Nowadays density functional theory (DFT) calculations are a cost-effective and commonly accepted way to predict physical and chemical trends. This thesis uses energies found via DFT and via higher level methods such as Møller–Plesset perturbation theory to 1) make kinetic predictions about the MTO process and 2) to study how it is affected by catalyst structure.

Firstly, a microkinetic model is implemented for 42 reactions from the initiation stage of the MTO process and 63 from the olefins cycle. The results indicate that, despite high barriers of over 200 kJ/mol, the dominant initiation pathway in H-SSZ-13 is the dehydrogenation of MeOH to produce CO followed by methylation of CO which leads to the formation of the first C-C bond.

Next diffusion limitations in H-SSZ-13 zeolite are explored with the diffusion barriers to pass through the 8-ring being found for a range of symmetric molecules of increasing molecular diameter. Small molecules such as ethene are not diffusion limited and can easily pass between the zeolite cavities. Above an effective diameter of 5.3 Å the barrier heights are found to scale linearly with species such as benzene likely being immobile.

The effects of changing the Si/Al ratio upon catalytic activity are explored for the well-studied methanol dehydration pathway in H-SSZ-13 zeolite. The reactions are modelled at a fixed first Brønsted acid site (BAS) with an additional BAS being placed at different neighbour distances. Motifs with the second site placed at the 3rd-nearest neighbour across the six-membered ring are found to be particularly reactive whereas 2nd-nearest neighbour across the four-membered ring are found to be particularly unreactive.

Lastly, the reactivity of the 12 different symmetry inequivalent sites in H-ZSM-5 are compared for 5 key reactions from the MTO process. It is found that the T12 site commonly used for modelling is indeed a good choice with most reactions occurring there having a comparably low barrier height.

Kurzfassung

Erdöl spielt eine entscheidende Rolle in der Weltwirtschaft und in der chemischen Industrie. Es ist jedoch nicht erneuerbar und schädlich für die Umwelt. Dies hat eine jahrzehntelange Suche nach alternativen Möglichkeiten zur Herstellung von chemischen Rohstoffen und Kraftstoffen aus erneuerbaren Quellen vorangetrieben. Der Methanol-zu-Kohlenwasserstoff (MTH)-Prozess, der auf Olefine im Methanol-zu-Olefin (MTO) Prozess und Benzin im Methanol-zu-Benzin-Prozess abgestimmt werden kann, ist ein vielversprechender Anwärter bei dieser Suche. Der Prozess findet in Zeolith-Katalysatoren statt und ist bereits im industriellen Maßstab praktikabel. Er ist in hohem Maße abstimmbare und hängt stark von Faktoren wie Katalysatorstärke, Zusammensetzung und Form ab.

Heutzutage sind Berechnungen mit der Dichtefunktionaltheorie (DFT) eine kostengünstige und weithin akzeptierte Methode, um chemische Vorhersagen zu treffen. In dieser Arbeit werden dft-Berechnungen verwendet, um 1) kinetische Vorhersagen über den MTO-Prozess zu machen und 2) zu untersuchen, wie dieser durch die Katalysatorzusammensetzung beeinflusst wird.

Zunächst wird ein mikrokinetisches Modell für 42 Reaktionen aus der Initiierungsphase des MTO-Prozesses und 63 aus dem Olefinzyklus implementiert. Die Ergebnisse zeigen, dass trotz hoher Barrieren von über 200 kJ/mol der dominante Initiierungsweg in H-SSZ-13 die Dehydrierung von MeOH zur Erzeugung von CO ist, gefolgt von der Methylierung von CO, die zur Bildung der ersten C-C-Bindung führt.

Als nächstes werden die Diffusionsbeschränkungen in H-SSZ-13 Zeolith untersucht, wobei die Diffusionsbarrieren zum Passieren des 8-Rings für eine Reihe von symmetrischen Molekülen mit zunehmendem Moleküldurchmesser gefunden werden. Kleine Moleküle wie zum Beispiel Ethen sind nicht diffusionsbegrenzt und können leicht zwischen den Zeolith-Hohlräumen hindurchtreten. Oberhalb eines effektiven Durchmessers von 5,3 Å skalieren die Barrierenhöhen linear, wobei Spezies wie Benzol wahrscheinlich immobil sind.

Die Auswirkungen einer Änderung des Si/Al-Verhältnisses auf die katalytische Aktivität werden für den gut untersuchten Methanol-Dehydratisierungsweg in H-SSZ-13-Zeolith untersucht. Die Reaktionen werden an einer festen ersten Brønsted-Säure-Stelle (BSS) modelliert, wobei eine zusätzliche BSS in unterschiedlichen Nachbarabständen platziert wird. Motive, bei denen die zweite Stelle an der drittnächsten Nachbarstelle über dem sechsgliedrigen Ring platziert ist, erweisen sich als besonders reaktiv, während die zweitnächste Nachbarstelle über dem viergliedrigen Ring besonders unreaktiv ist.

Schließlich wird die Reaktivität der 12 verschiedenen symmetrieungleichen Stellen in H-ZSM-5 für 5 Schlüsselreaktionen aus dem MTO-Prozess verglichen. Es zeigt sich, dass die für die Modellierung häufig verwendete T12-Stelle tatsächlich eine gute Wahl ist, da die meisten dort ablaufenden Reaktionen eine vergleichsweise niedrige Barrierenhöhe aufweisen.

Contents

Abstract	i
Kurzfassung	iii
1 Introduction	1
1.1 The MTO process	1
1.1.1 General overview	1
1.1.2 Zeolites frameworks	2
1.1.3 The reaction mechanism	4
1.1.4 Modelling the MTO process	8
2 Outline and scope	11
3 Methods	12
3.1 Electronic structure methods	12
3.1.1 The multi-particle Schrödinger equation	12
3.1.2 The Born-Oppenheimer approximation	13
3.1.3 The variational principle	13
3.1.4 Molecular orbital theory	14
3.1.5 Slater determinants	14
3.1.6 The Hartree-Fock method	15
3.1.7 Self-consistent field solutions	17
3.1.8 The complete basis set limit	18
3.1.9 Post Hartree-Fock methods	19
3.1.10 Scaling of density functional theory with system size	20
3.1.11 Hohenberg-Kohn theorems	21
3.1.12 Kohn-Sham equations	21
3.1.13 Choice of functional	22
3.1.14 Plane wave basis sets	23
3.1.15 Pseudopotentials	24
3.1.16 Grimme's D3 correction	25
3.2 Characteristics of energy surfaces	27
3.2.1 Geometry optimisation	27
3.2.2 Transition state searching	28
3.2.3 Vibrational analysis	30
3.3 Thermochemistry	31
3.3.1 The Harmonic limit	31
3.3.2 The ideal gas limit	32
3.4 Kinetic modelling	34
3.4.1 Transition state theory	34
3.4.2 Microkinetic modelling	35
3.4.3 Kinetic Monte Carlo	36
3.4.4 Multiscale modelling	38

4	Modelling the formation of the first olefins in the MTO process	39
4.1	Introduction	39
4.2	Results and Discussion	40
4.3	Methods	46
4.4	Conclusion	47
5	Diffusion limitations in H-SSZ-13 zeolite	48
5.1	Introduction	48
5.2	Results and Discussion	49
5.3	Methods	56
5.4	Conclusion	57
6	Trends in reactivity due to proximate acid sites in H-SSZ-13	58
6.1	Introduction	58
6.2	Results and discussion	59
6.3	Methods	66
6.4	Conclusion	67
7	Trends in reactivity due to changing the choice of T-site in H-ZSM-5	68
7.1	Introduction	68
7.2	Results and discussion	69
7.3	Methods	75
7.4	Conclusion	75
8	Final outlook and conclusions	76
	References	83
	Appendix	vi
A	Modelling the formation of the first olefins in the MTO process	vi
B	Diffusion limitations in H-SSZ-13 zeolite	xi
C	Trends in reactivity due to proximate acid sites in H-SSZ-13	xvi
D	Trends in reactivity due to changing the choice of T-site in H-ZSM-5	xxiii

1 Introduction

Many of the bulk chemicals and transportation fuels needed for modern society to function are derived from crude oil. We are so dependent on crude oil because it is carbon rich, high in energy density and there is already a centuries old infrastructure in place to use it. We cannot continue to use it so heavily because 1) its reserves are finite and 2) its combustion produces CO_2 which, at its current concentration in the global atmosphere, is a key contributor to climate change. Alternatives need to be explored which could include utilising biomass, recapturing carbon and finding renewable energy alternatives such as wind, hydro and solar power. The process of converting biomass into fuels and platform chemicals can be divided into two very broad and often overlapping steps 1) de-construction and fractionation of raw feedstocks and 2) refining and upgrading of the resulting products. De-construction and fractionation can be achieved via thermal conversion, for example via, combustion, pyrolysis and gasification or via biochemical conversion for example anaerobic digestion, fermentation and composting. The products can then be refined into target chemicals either thermo or bio chemically. This thesis is concerned with how methanol, which can reasonably straight forwardly be produced via gasification of biomass, can be upgraded into olefins/alkenes.

1.1 The MTO process

1.1.1 General overview

The methanol-to-hydrocarbons process (MTH) [1–8] aims to produce a variety of fuels and chemical feed-stocks starting from methanol or a methanol dimethyl ether (DME) mixture. This is typically done at a temperature of around 350-400 °C and at standard pressure. The process has been run on industrial scale for many years already [9, 10], notably for ethene and propene production [11]. It can be steered towards gasoline rich products in the methanol-to-gasoline process and towards olefins in the methanol-to-olefins (MTO) process.

Methanol itself can be synthesised from a mixture of carbon dioxide, hydrogen and carbon monoxide known as Syngas which is easily produced from an abundance of different hydrocarbon feedstocks, many of which are renewable. Hence, the MTH process is considered to be a promising way to reduce our reliance on diminishing crude oil reserves [12]. Some authors even go so far as to imagine that in a post oil society we will have a methanol economy where methanol is used both for energy storage and as a feedstock for the majority of our societies needs [13]. Figure 1.1 presents a simple scheme to showing some of the different possible feedstocks and products related to the MTH process.

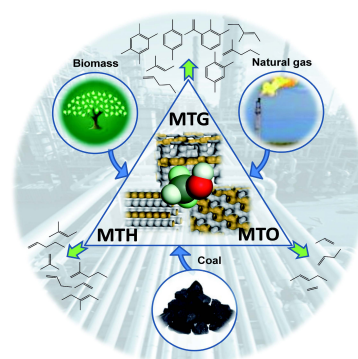


Figure 1.1: Reprinted coveragepage from ref. [7], Copyright (2012), with permission from John Wiley and Sons.

1.1.2 Zeolites frameworks

The MTO process is catalysed by zeolites which are microporous aluminosilicate framework materials. They belong to the tectosilicates class of materials which can be described by the chemical formula

$$[A_x B_y O_{2x+2y}]^{x-} \quad (1.1)$$

A and B stand for variables in the above. Usually A=Al and B=Si but many other [15] atomic substitutions are possible. Figure 1.2 presents a variety of commonly used zeolite frameworks. The frameworks used in this work are CHA in its H-SSZ-13 form and MFI in its H-ZSM-5 form.

Zeolites form 3D frameworks of TO_4 tetrahedra with a 1:2 ratio of T to O. The tetrahedra combine to form a periodic system of cavities which are connected to each other via pores. The cavities are often many Å wide and able to accommodate guest molecules. The pores are large enough for diffusion to be possible and are often characterised by rings that comprise them. Common rings sizes are 8, 10 and 12 (tetrahedra), which are considered small, medium and large respectively. The pores themselves are often characterised by being straight with the path through them simply being a straight line or sinusoidal when the consecutive rings along the path are not aligned with each other. The classification of zeolites is heavily based upon the number of symmetry unique T-sites they contain. If two fourfold-coordinated atoms of type T can be related to each other by symmetry operations this could be for example, reflection in a plane or improper rotation then they are not symmetry unique. CHA [16] is an appealing zeolite to study because all T-atoms in the structure are symmetry equivalent, MFI on the other hand has

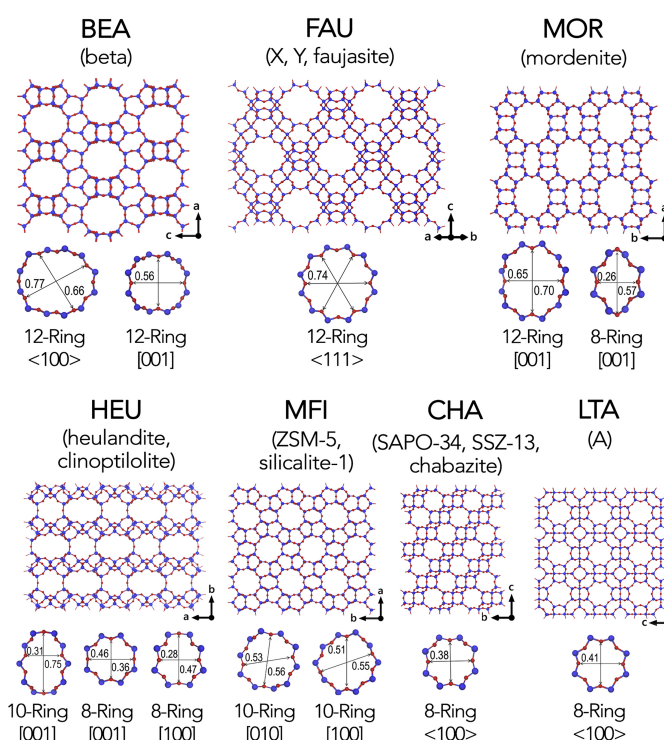


Figure 1.2: Reprinted from ref. [12], Copyright (2017), with permission from Elsevier: "Selected Widely Used Zeolite Framework Types. For each framework type, the three-letter code assigned by the International Zeolite Association (in bold), the names of zeolites belonging to the corresponding framework type, the ball-stick atomic model, and the pore windows are given. Blue spheres denote T atoms, and red spheres represent oxygen atoms. The size of the ring (in nm) and the pore directions are also given."

Much of the information in this section which is related to zeolite topology can be found in the database maintained by The Structure Commission of the International Zeolite Association (<http://www.iza-structure.org/databases/>) [14].

12 different T-sites [17]. Figure 1.3 presents the different T-sites in the MFI framework.

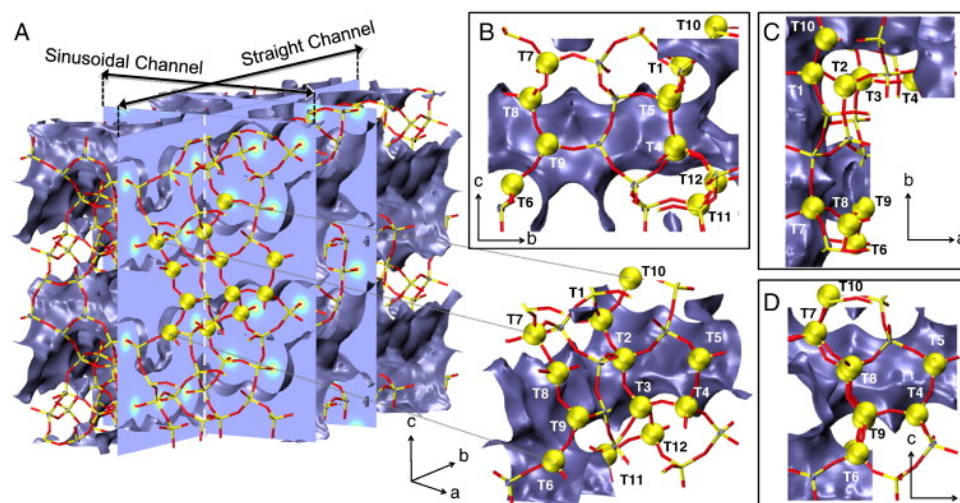


Figure 1.3: Reprinted from ref. [18], Copyright (2014), with permission from Elsevier: "(A) 3-dimensional (3D) overview of the siliceous MFI framework (Si — yellow, O — red). The sinusoidal channel along the a direction and the straight channel along the b direction are approximated by an isosurface (purple) of the calculated charge density at $0.004 \frac{e}{\text{\AA}^3}$. The two parallel planes normal to the b direction cut through the center of two adjacent sinusoidal channels. The plane normal to the a direction cuts through the center of a straight channel. All 12 crystallographically distinct T sites are marked in the enlarged version of the 3D representation and in the corresponding 2D projections in all three directions (panels B–D)."

The number of zeolites in existence has continually increased throughout the years. According to the Atlas of zeolite Frameworks [19], in 1970 there were 27, in 1982 there were 85 and in 2001 there were 133. This has prompted some to ask where is the upper limit is for the number of possible structures [20, 21]. Some authors suggest that we are far from the upper limit with millions of possible structures potentially existing. Around 350,000 theorised structures have formation energies within 30 kJ/mol of α -quartz, indicating they have a stability well within the range of synthesised materials [21]. The ultimate aim of such an approach would be to have a database of all possible structures which helps one screen for the perfect catalyst for a given application [22]. For now, out of the structures 250+ which have been synthesised already only a small percentage are used commercially [23]. These structures are extensively used however, for example, as ion exchangers, for gas separation and also for catalysis [24]. Within oil refining alone zeolites are used in light naphtha isomerization, olefin alkylation, reforming, cracking and hydrocracking [23, 25]. Practically every diesel car exhaust has a catalytic converter which may contain a zeolite which is used for exhaust gas aftertreatment. Owing to their high adsorption capacity zeolites are also used to treat nuclear waste, for example, after the Fukushima disaster large sacks containing zeolites were put into the water near the reactor site in order to absorb as much nuclear material as possible [24]. The fact that zeolites are so widely used in industry is a consequence of their physical and chemical properties. They possess high chemical stability in a large variety of environments and high thermal stability at elevated temperatures [12]. One can choose from large variety of frameworks for one's purpose, for example choosing zeolites with a given pore size in order to use the zeolite as a molecular sieve [26, 27]. Furthermore, they remain stable

upon many different types of substitution with these substitutions able to drastically alter their chemical properties.

1.1.3 The reaction mechanism

The catalyst for the MTO process is a H zeolite which often consists of an inorganic oxygen silicon framework that contains a small quantity of aluminium. The extra charges from trivalent alumina are balanced by charge compensating protons to produce Brønsted acid sites (BASs) [28]. BASs catalyse the MTO process by protonating guest species, binding intermediate species and by being reprotonated after a given reaction has occurred. They are widely considered to be responsible for a large majority of the catalytic activity in the MTO process. The framework is chemically stable with the position of the alumina mainly governed by how the zeolite was synthesised (see [3] for details on zeolite synthesis). The charge compensating proton on the other hand can sit on any of the four oxygen's connected to an aluminium. The protons can easily transfer between the sites with the assistance of proton shuffling species such as water and methanol [29].

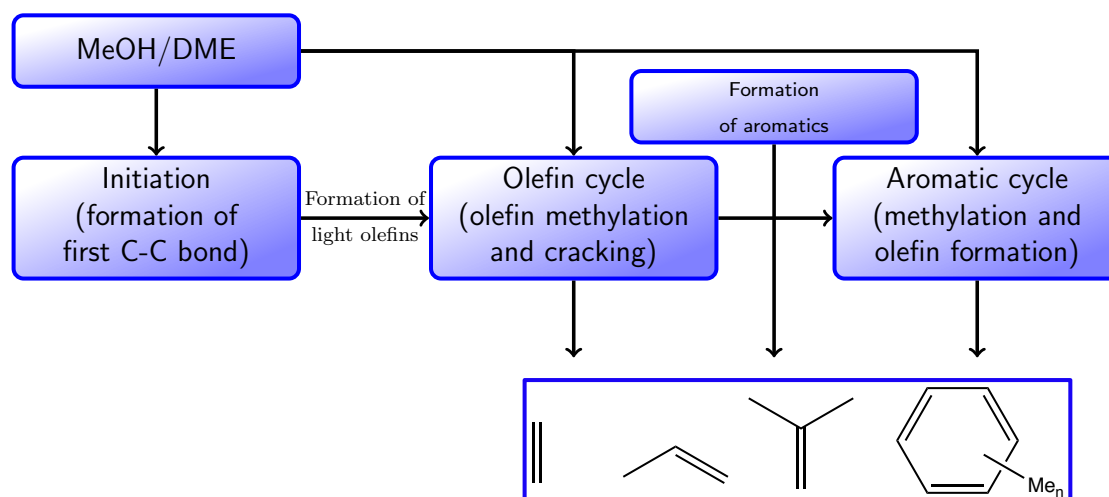
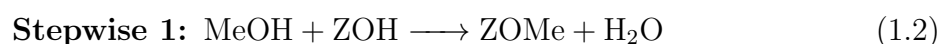


Figure 1.4: Schematic overview of the MTO process starting from a pure MeOH/DME feed.

The MTO process can be broadly divided into three different parts 1) initiation 2) the olefin cycle which is also commonly referred to as the alkene cycle and 3) the aromatic cycle, this is shown schematically in Figure 1.4. Starting from methanol guest species can be successively methylated and gradually grow in size with successive methylations. Equations 1.2-1.4 show the stepwise and concerted (synonymously dissociate and associative) pathways for a generalised olefin O_n being methylated to O_{n+1} . Z stands for the zeolite framework and Me for a methyl group.



A multitude of different initiation mechanisms have been proposed in the literature [6] including a zoo of different intermediates. The reaction mechanisms explored in this work commonly have carbocations, oxonium ions and surface methoxy species (SMS) as key intermediates. However, mechanisms based upon other families such as carbenes, oxonium ylides and free radicals have also been explored. In a recent study [2] a direct mechanism from methanol to propylene was proposed which proceeds via the formation of carbon monoxide. The mechanism is shown in Figure 1.5. The proposed mechanism was shown to be more likely than a methane-formaldehyde type mechanism. Furthermore, the authors demonstrated its viability via a simple two step kinetic model which mimics the autocatalytic nature of the MTO process.

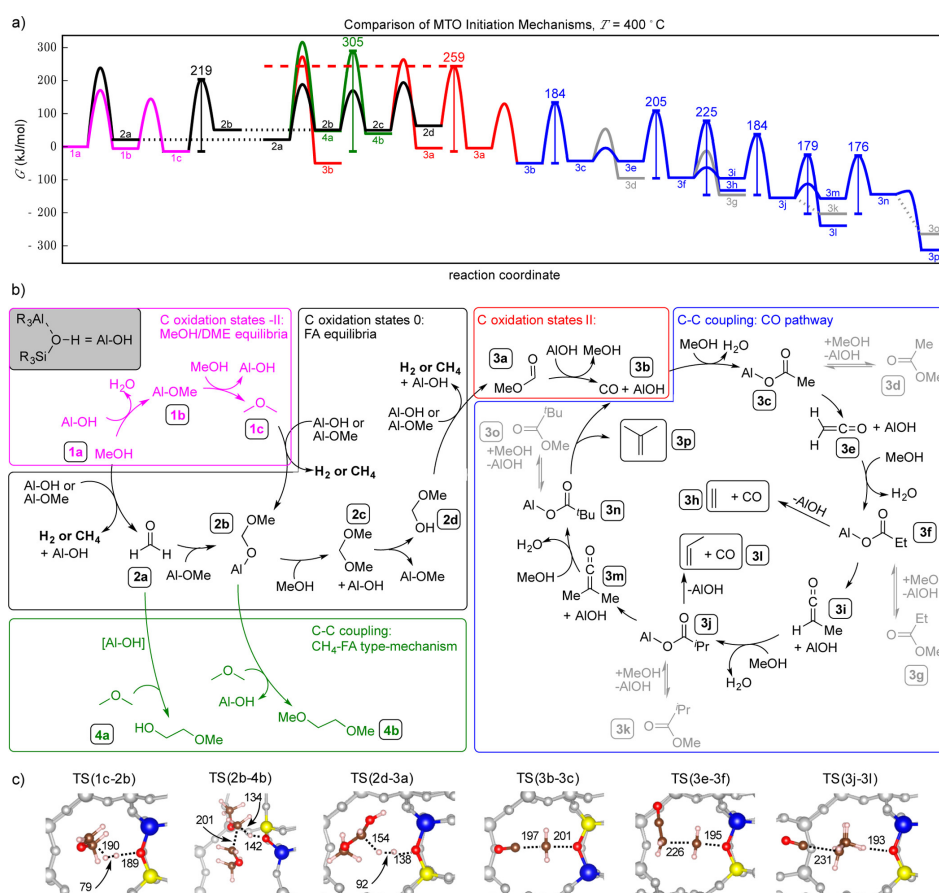


Figure 1.5: Reprinted from ref. [2], Copyright (2017), with permission from the American Chemical Society:”(a) Free energy diagram of the possible pathways for initiation of the MTO reaction shown in (b). For important activation barriers, the value is given in kJ/mol relative to the most stable prior intermediate, as indicated by the vertical lines under these barriers. (b) Overview of the most relevant initiation mechanisms of the MTO reaction. Al-OH and Al-OMe are used to abbreviate bridging hydroxyl and methoxy groups (for example Al-OH-Si). Mechanisms are grouped into boxes according to the oxidation state of carbon. Formation of the surface methoxy group is shown explicitly only for the reaction 1a to 1b and is omitted for clarity in all subsequent reactions since it is not rate-limiting. In the reaction of 3f to 3h, the intermediate formation of Al-OEt is omitted. (c) Structure of the most relevant transition states. Formed and broken bonds are indicated with dotted lines, and distances are given in pm; the color code is H, white; Si, yellow; Al, blue; O, red; C, brown. Framework atoms that do not participate directly in the reaction are shown in gray.”

Eventually light olefins such as ethene and propene are formed which can then be further methylated. Olefins are then able to grow in chain length before cracking once again yielding light olefins. Species which are continually regenerated via cracking are known as hydrocarbon pool (HP) species [30–34]. In the MTO process it is widely observed there is an induction period where product formation remains low for some time before "lighting off" when enough key HP intermediates have been formed. Similarly, in the aromatic cycle cyclic species can develop side-chain groups which grow in size via successive methylations before being eliminated. Furthermore, in pairing type mechanisms 5 member rings able to expand into 6 member rings and vice versa again with short chain side groups being eliminated along the way. It is widely accepted that the MTO process has a dual-cycle mechanism where the olefin cycle and the aromatic cycle are intricately intertwined [35]. For example, the olefin products from the aromatic cycle can often function as active intermediates during the olefin cycle. Figure 1.6 illustrates a dual-cycle type reaction mechanism.

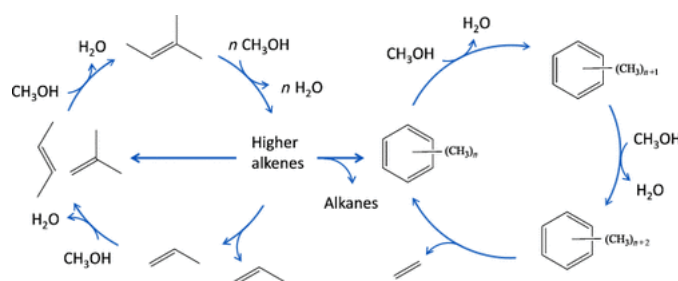


Figure 1.6: Reprinted from ref. [7], Copyright (2012), with permission from John Wiley and Sons: "Suggested dual-cycle concept for the conversion of methanol over H-ZSM-5."

How exactly the first HP species form, which species constitute the HP and their relative importance are topics which are still hotly debated. Some suggest that the first HP species are formed directly from methanol via direct C-C bond formation while others suggest that the first HP species may arise due to impurities in the feed [36]. Part of the difficulty in unravelling the details of the mechanism stems from its dual-cycle nature but also the number of different possible elementary reaction steps involved in the reaction scheme. One proposed reaction mechanism can quickly become extremely large when considering successive methylations, isomerisations, cracking processes and so on [2, 37, 38]. Furthermore, important quantities such as activity and selectivity can be highly dependent on the subtle and difficult to measure interplay between the catalyst topology, catalyst acidity and the reaction conditions [1, 39].

One of the unique characteristics of the MTO process is that it is highly dependent upon the type of zeolite framework used. Figure 1.7 shows results from an experiment run at almost identical conditions except for the shape of the of catalyst. In the upper part H-SSZ-13 (CHA framework) is used and in the lower part H-ZSM-5 (MFI framework) is used. Even though framework itself does not directly take part in reactions changing it leads to a dramatically different final product distribution. In general zeolites exert a high degree of shape selectivity on the initial, intermediate and final states of a reaction [26] and confinement effects are central to determining what the product distribution will be for a given zeolite. The type of zeolite framework is also highly connected to how they deactivate. One of the main ways deactivation occurs is via coking [40, 41] which occurs when long chain and often unreactive hydrocarbons and polyaromatics build up in the cavities and on the surface of the catalyst. As an example, in ethene and propene production H-SAPO-34 (CHA topology) is particularly susceptible to coking due having large cavities compared its pore diameter and must be replenished regularly [42]. It is however, when tuned properly, much more selective to the desired products than other common catalysts such as H-ZSM-5.

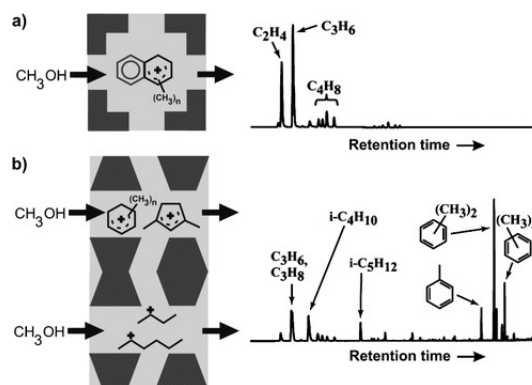


Figure 1.7: Reprinted from ref. [1], Copyright (2013), with permission from John Wiley and Sons: "Representation of the main HP species in H-SAPO-34 (a) and H-ZSM-5 (b). n refers to the number of methyl substituents on the aromatic rings. Corresponding chromatograms illustrate the product selectivity for both materials under identical conditions.(taken from ref. [7]; experiments using 300 mg of catalyst operated at 723 K, products sampled 1.5 s following pulse introduction of 10.2 μL of methanol)"

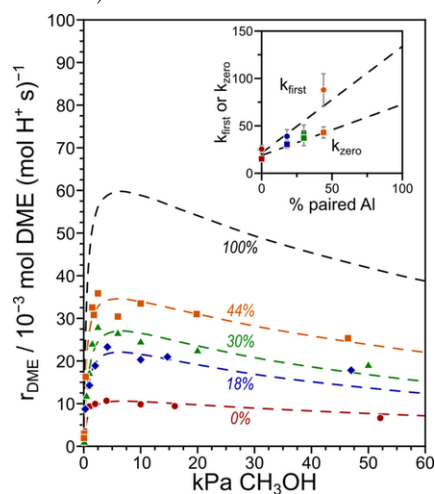


Figure 1.8: Reprinted from ref. [45], Copyright (2020), with permission from John Wiley and Sons: "DME formation rates (per H^+ , 415 K) as a function of methanol pressure on H-CHA with 0% (circles, red), 18% (diamonds, blue), 30% (triangles, green), 44% (squares, orange), and the extrapolation to 100% (black) 6 MR paired Al. Inset: first-order (k_{first} , circles, 10^{-3} mol DME ($\text{kPa mol H}^+ \text{s})^{-1}$) and zero order (k_{zero} , squares, 10^{-3} mol DME ($\text{mol H}^+ \text{s})^{-1}$) rate coefficients as a function of the percentage of 6 MR paired Al. Adapted from prior work [46]"

Another way to tune the MTO process is by controlling the number and proximity of BASs that the zeolite catalyst contains. Commercially synthesised zeolites can be made with a wide variety of different Si/Al ratios and it is possible to tune a zeolites acidity based on synthesis conditions [43, 44]. Figure 1.8 shows experimental results in H-SSZ-13 zeolite which indicate rates for DME-formation correlate well with the number of proximate Al-pairs.

1.1.4 Modelling the MTO process

This work is based in the field of theoretical heterogeneous catalysis (HC). Heterogeneous catalysis aims to predict how catalyst composition and structure influence rates of reactions and product distribution. It is an extremely collaborative research field with new insights and research themes stemming from many different sub-fields such as theory, catalyst synthesis, spectroscopy and microscopy, lab scale experiments and the industrial scale. Theoretical catalysis often thrives in answering questions on the basis of atomic scale simulations which would be very difficult to probe experimentally. On the other hand, identification of key reaction intermediates via detailed spectroscopy and microscopy can provide both useful input for and verification of reaction mechanisms obtained via theoretical modelling [47]. Furthermore, theoretical modelling may have difficulties reproducing complex kinetic phenomena observed in experiments [7]. Well-designed experiments can, in principle, yield detailed information about which species are present and how their concentrations change along the catalyst bed with time. One way of yielding this information is to run the experiment at the desired conditions before thermally quenching, dissolving the zeolite framework in hydrofluoric acid and then extracting the species present via a solvent [48]. The reactant species which were enclosed within the cavities are thus available for analysis using standard chromatographic techniques. Insights into the mechanism may be gleaned by coupling such an approach with isotopic labelling [30] or by observing the effects of cofeeding a given reactant [49]. A variety of spectroscopic methods can, reasonably straightforwardly, yield *ex situ* information about the catalyst structure and the locations of the active sites. Increasingly *operando* and *in situ* spectroscopic methods are being applied, often with much more difficulty, to make real time predictions of catalytic phenomena [50, 51].

Theoretical HC relies heavily on methods from computational chemistry [22, 52–54]. Predictions are made *in silico* based on a simplification of reality which most adequately reproduces what one wishes to model [53, 55]. The model used depends on the length scale being probed, the accuracy required in order to make a reasonable prediction and the resources available. Currently *ab initio* methods such as Coupled Cluster theory which rely solely of the nuclear coordinates as input are too computationally demanding to be used as the main method of calculation. Instead semi-empirical and density functional theory (DFT) based methods are the workhorses of computational chemistry. They necessarily contain parameterisations, approximations and numerical procedures which make them computationally less expensive at the expense of accuracy. Furthermore, if more accuracy is required to make a prediction then higher level methods can then be applied to the structures obtained via more computationally affordable methods.

Crucially, the predictions DFT makes are precise enough to use for trend studies and to plot scaling relations with. Figure 1.10 shows a typical example of the use of scaling relations in zeolite catalysis and Figure 1.9 shows results from a recent study which strongly support the idea that DFT predicts trends in zeolite catalysis well. HC has a rich history [56–58] of using computational screening to design new catalytic materials which is often done by plotting theoretical descriptors such as adsorption energies, bond lengths and transition state energies against each other. Such an approach is often justified by the Bell–Evans–Polanyi principle [59, 60] which observes that the difference in activation energy between two reactions of the same family is proportional to the difference of their enthalpy of reaction.

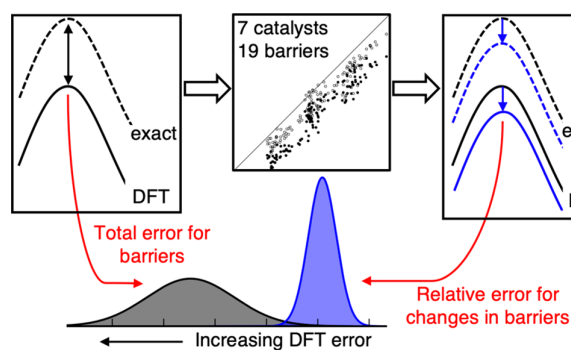


Figure 1.9: Graphical abstract reprinted from [61], Copyright (2020), with permission from the American Chemical Society.

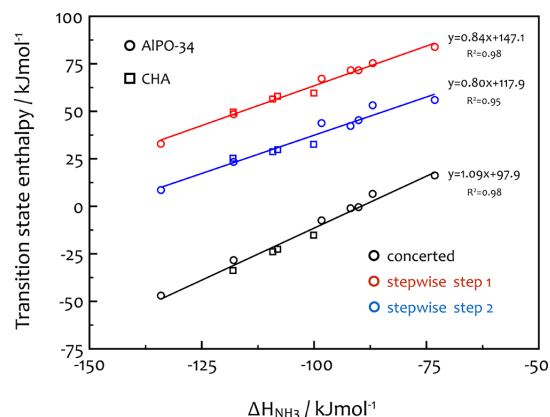


Figure 1.10: Reprinted from [58], Copyright (2014), with permission from the American Chemical Society: "Linear scaling relations between the transition-state enthalpies and $\Delta H_{ads}(\text{NH}_3)$ for the methanol-propene reaction through the concerted and stepwise pathways."

Zeolites are excellent for researchers to model because they have a well-defined, well understood active site, and a periodic structure. Within the cavities guest olefins can typically form 1) Van der Waals (vdW) complexes 2) π -complexes 3) cations 4) alkoxides. A depiction of these different states with the same numbering as shown in Figure 1.11. Equations 1.2-1.4 in the last section describe a typical methylation mechanism for an olefin being methylated in a zeolite. Figure 1.12 draws out the stepwise and concerted pathways for DME synthesis. Figure 1.13 draws this out for the case of propene methylation. The subscripts app and int indicate the apparent and intrinsic energy barriers. The lower part of Figure 1.13 shows a typical example of how strongly the enthalpy (ΔH) and Gibbs free energy (ΔG) profiles can differ for methylation steps in the MTO process.

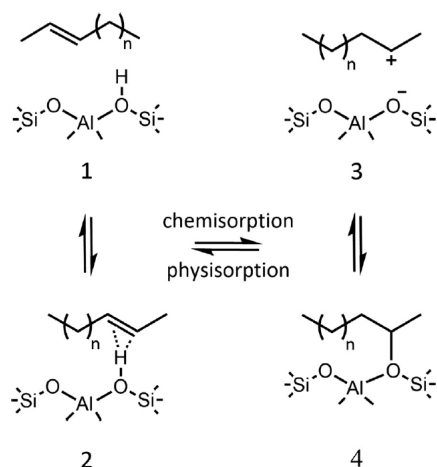


Figure 1.11: Reprinted from ref. [62], Copyright (2014), with permission from Elsevier: "Four adsorption states of a 2-alkene – 1: Van der Waals complex, 2: π -complex, 3: carbenium ion, 4: alkoxide."

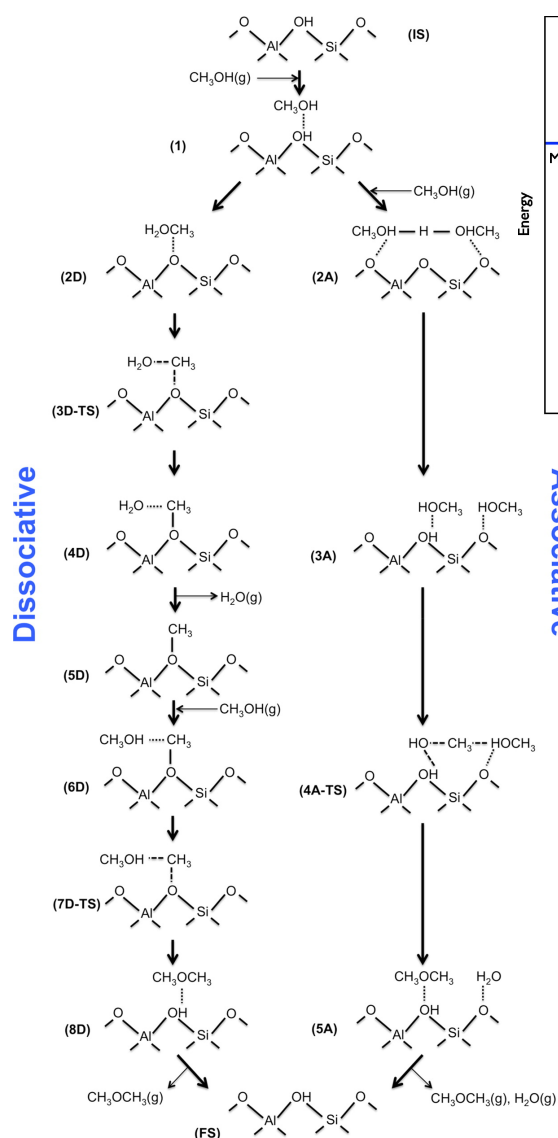


Figure 1.12: Reprinted from [63], Copyright (2016), with permission from the American Chemical Society: "Dissociative (Left) and Associative (Right) Reaction Pathways for the Conversion of Methanol to DME Catalyzed by an H-form Zeolite. States labeled "D" and "A" belong to the dissociative and associative routes, respectively. Labels that contain "TS" represent the transition states. Electrostatic interactions between adsorbates and active sites are denoted by dotted lines, while transition-state complex interactions are denoted by dashed lines."

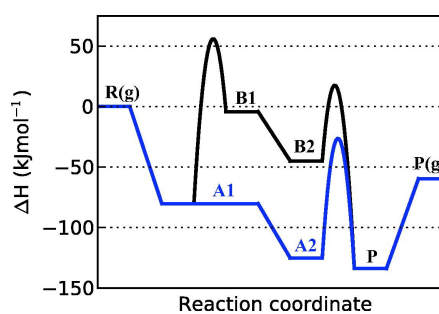
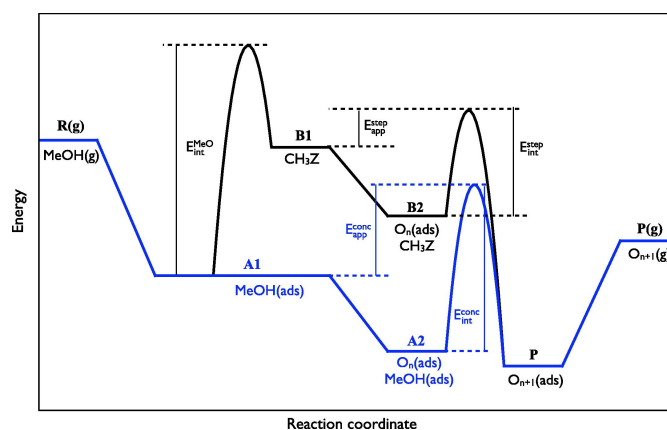


Figure 1.13: Reprinted from [64], Copyright (2014), with permission from Elsevier. Upper: "Generic energy profiles along the concerted (blue) and stepwise (black) pathways as modeled in the DFT calculations, including the definitions of apparent and intrinsic reaction barriers. Each state is described by the species methanol (MeOH), surface-methoxy groups (CH3Z), alkene (O_n) and methylated alkene (O_{n+1}) as well as the shorthand notation to be used in calculated energy profiles below. Species not included in the state descriptions are in gas phase." Lower: Calculated enthalpy (left) and free energy (right) profiles at 673K for the reactions between methanol and propene along the concerted (blue) and stepwise (black) pathways in H-ZSM-22."

2 Outline and scope

The MTO process is routinely modelled on the atomic scale using DFT calculations with a rich variety of reaction mechanisms having been proposed in the literature. Often research is done on the subject **1)** without detailed kinetics being done or with the kinetics being oversimplified, for example, by using steady state microkinetic models or by making assumptions about the rate based upon the highest energy barrier. In order to capture the autocatalytic nature of the MTO reaction a more detailed microkinetic model is essential. **2)** Using a high Si/Al ratio and a "set and forget" approach to choosing the BAS location. The choice of BAS location in a given study is often justified on the basis of accessibility or stability. It is often assumed that there is just one acid site per unit cell and sometimes it is further assumed that reactions only occur at one particular framework oxygen. In reality BAS location is highly dependent how the catalyst was synthesised and a large range of different acid site motifs are present in a real working catalyst.

This thesis aims to explore extensions to how the MTO process is currently modelled. The two main topics are:

Topic 1) Kinetic-modelling based upon energies obtained via chemically accurate electronic structure calculations.

Topic 2) Investigating how the location and proximity of BASs influence reactivity.

Topic 1):

Chapter 4: Implements a kinetic model of the initial stages of the MTO process which carefully takes its autocatalytic nature into account.

Chapter 5: Explores diffusion limitations in H-SSZ-13. Diffusion barriers are found for a range of symmetric molecules with the aim being to estimate a molecular diameter at which diffusion is infeasible.

Topic 2):

Chapter 6 Investigates how much reactions occurring at a fixed first BAS in H-SSZ-13 are by affected by the addition of secondary BASs.

Chapter 7 Compares reaction barriers for processes occurring at all 12 different T-site locations in H-ZSM-5.

3 Methods

3.1 Electronic structure methods

3.1.1 The multi-particle Schrödinger equation

The great majority of the work in this thesis will have its origins in the Schrödinger equation which in the position basis for a single particle system is

$$\hat{H}\Psi = E\Psi \quad (3.1)$$

$$\hat{H} = -\frac{\hbar^2}{2m}\nabla^2 + V(\mathbf{r}) \quad (3.2)$$

where Ψ is the wave function, \hat{H} is the Hamiltonian operator. The first term is the kinetic energy (KE) and the second is the potential energy, which for example, for the electron in the hydrogen atom $V(\mathbf{r})$ would be the electrostatic potential due the nucleus.

Analytical solutions of the Schrödinger equation are only possible for a few simple problems such as a particle in a box, a harmonic oscillator, and the hydrogen atom. For most systems of interest in chemistry, there is no analytical solution and direct numerical solutions are computationally expensive. When solving the Schrödinger equation for the multi-particle case the wave function depends on $3N$ electronic coordinates ($4N$ if spin is also included) where N is the number of electrons and also on the nuclear coordinates. In the multi particle case the Hamiltonian becomes;

$$\begin{aligned} \hat{H}(\mathbf{r}, \mathbf{R}) = & \underbrace{-\frac{\hbar^2}{2m} \sum_r \nabla_r^2}_{\hat{T}_r} \underbrace{-\frac{\hbar^2}{2M} \sum_n \nabla_n^2}_{\hat{T}_R} + \underbrace{\frac{1}{8\pi\epsilon_0} \sum_{i \neq j} \frac{e^2}{|\mathbf{r}_i - \mathbf{r}_j|}}_{\hat{V}_r} \\ & + \underbrace{\frac{1}{8\pi\epsilon_0} \sum_{n \neq m} \frac{Z_n Z_m e^2}{|\mathbf{R}_n - \mathbf{R}_m|}}_{\hat{V}_R} - \underbrace{\frac{1}{4\pi\epsilon_0} \sum_{i,n} \frac{Z_n e^2}{|\mathbf{r}_i - \mathbf{R}_n|}}_{\hat{V}_{r,R}} \end{aligned} \quad (3.3)$$

\hat{T} indicates a kinetic term and \hat{V} indicates a potential term. Little \mathbf{r} stands for the electronic coordinates and big \mathbf{R} stands for the nuclear coordinates. There are two electronic terms, two nuclear terms and a mixed term which depends both on the nuclear and the electronic coordinates.

For a broader discussion of the content discussed in section 3.1 see references [65–67].

3.1.2 The Born-Oppenheimer approximation

The Born-Oppenheimer (BO) approximation is heavily used in quantum chemistry and throughout this work. It states that the electronic wave function Ψ_e and the nuclear wave function Ψ_N can be treated separately. This is often motivated by the idea that the electrons, which are around 1800 times lighter than the individual nucleons, move so fast compared to the nuclei that they can always adiabatically update their state for a given position of the nuclei. The result of making the BO approximation is that the electronic wave function $\Psi_e(\mathbf{r}; \mathbf{R})$ depends explicitly on the electronic coordinates but only parametrically on the nuclear coordinates.

$$\hat{H}_e \Psi_e(\mathbf{r}; \mathbf{R}) = E_e(\mathbf{R}) \Psi_e(\mathbf{r}; \mathbf{R}) \quad (3.4)$$

$$[\hat{T}_N + E_e(\mathbf{R})] \Psi_N(\mathbf{R}) = E \Psi_N(\mathbf{R}) \quad (3.5)$$

The BO approximation can fail. Notably at conical intersections where there can be significant coupling between the electronic and the nuclear degrees of freedom.

3.1.3 The variational principle

The variational principle is central to the development of algorithms for finding approximate solutions to the multi-particle Schrödinger equation. It is fundamental to both deriving and to calculating expressions for the energy in both Hartree-Fock (HF) theory and DFT. It states for a given trial wave function Ψ the true ground state energy E_0 will always be a lower bound to this and that $E = E_0$ if and only if Ψ is the true wave function.

$$E[\Psi] = \frac{\langle \Psi | \hat{H} | \Psi \rangle}{\langle \Psi | \Psi \rangle} \geq E_0 \quad (3.6)$$

Here $|\Psi\rangle$ denotes a ket vector from standard bra-ket notation and the square brackets denote a functional. A formal way to minimise such an expression is via the calculus of variations. In many cases in quantum chemistry the relation between the energy and the wave functions or densities is of functional form and the task is to minimise it, often subject to certain constraints.

3.1.4 Molecular orbital theory

Molecular orbital theory (MOT) is one of the two basic theories used to explain chemical bonding. In MOT electrons move in the external potential of all the nuclei in the molecule and they occupy molecular orbitals ϕ_i . The molecular orbitals can be expressed as a linear combinations of atomic orbitals χ_i .

$$\phi_i = \sum_r c_{ri} \chi_r \quad (3.7)$$

where c_{ri} are to coefficients in the expansion. The atomic orbitals chosen are often those of "hydrogen-like" atoms i.e. atoms with only one electron but with the appropriate nuclear charge. The other basic theory is valence bond theory which instead assigns the electrons to chemical bonds rather than orbitals.

Perhaps the most physically intuitive choice for the atomic orbitals is Slater-type orbitals (STOs) [68] which possess less radial nodes than analytical solutions to the hydrogen atom (Schrödinger orbitals) but retain key features such as cusps at the nuclei (Kato's cusp condition [69]) and exponential decay. A general form for STOs is

$$\chi_{\zeta nlm}(r, \theta, \phi) = N Y_{lm}(\theta, \phi) r^{n-1} e^{-\zeta r} \quad (3.8)$$

where r is the radius, θ is the polar angle and ϕ is the azimuthal angle. The constant ζ is related to the charge of the nucleus, n , l and m are principle quantum numbers, $Y_{lm}(\theta, \phi)$ are spherical harmonics and N is a normalisation factor. Other choices include Gaussian type orbitals [70] which approximate STOs but are much easier to deal with due to the nature of the Gaussian product, or pseudo-atomic-orbitals which result from using an approximate form for the nuclear potentials.

3.1.5 Slater determinants

Slater determinants [71] express the wave function in terms of the atomic orbitals and combine them so that the anti-symmetry requirements of the Pauli exclusion principle are satisfied. There needs to be a change in sign every time two electrons are exchanged i.e. the total wave function should be anti-symmetric with respect to the permutation of any two electrons. The formula for a single Slater determinant is

$$\psi(\mathbf{x}_1, \dots, \mathbf{x}_N) = \frac{1}{\sqrt{N!}} \begin{vmatrix} \chi_1(\mathbf{x}_1) & \chi_2(\mathbf{x}_1) & \cdots & \chi_N(\mathbf{x}_1) \\ \chi_1(\mathbf{x}_2) & \chi_2(\mathbf{x}_2) & \cdots & \chi_N(\mathbf{x}_2) \\ \vdots & \vdots & \ddots & \vdots \\ \chi_1(\mathbf{x}_N) & \chi_2(\mathbf{x}_N) & \cdots & \chi_N(\mathbf{x}_N) \end{vmatrix} \quad (3.9)$$

The atomic orbitals χ_i are listed along one axis of the determinant and the position coordinate changes along the other axis.

3.1.6 The Hartree-Fock method

Making the BO approximation yields a simpler form for the Hamiltonian and using MOT expresses the molecular orbitals in terms of atomic orbitals. The next step is to find a way to solve for the electronic energy E_{el} . The archetypal approach in quantum chemistry is the HF approach. A useful starting point is to express the Hamiltonian in terms of one-electron operators $\hat{h}(i)$ and two-electron operators $\hat{v}(i, j)$.

$$\hat{h}(i) = -\frac{1}{2}\nabla_i^2 - \sum_A \frac{Z_A}{r_{iA}} \quad (3.10)$$

$$\hat{v}(i, j) = \frac{1}{r_{ij}} \quad (3.11)$$

$$\hat{H} = \sum_i \hat{h}(i) + \sum_{i < j} \hat{v}(i, j) + E_{NN} \quad (3.12)$$

$\hat{h}(i)$ accounts for the KE of electron i as well as its attraction to all of the nuclei which are summed over via the index A . $\hat{v}(i, j)$ accounts for the Coulomb interaction between a pair of electrons i and j . In the full Hamiltonian \hat{H} the sum over the two-electron operators is restricted to $i < j$ to avoid double counting. The term E_{NN} accounts for the coulomb repulsion between the nuclei (which formally belongs to the nuclear equations of motion). As it is a constant (when the BO approximation holds) it will not affect the form of the final solution.

The expression for E_{el} (equation 3.6) must be calculated from the Slater determinant (equation 3.9) and \hat{H} . Expanding all the terms yields a large number of potentially cumbersome $3N$ dimensional integrals. Forgiveably however, many of the terms evaluate to zero or one and only terms involving at most two electrons survive. The Slater-Condon rules [71, 72] can be followed to reach the final result.

$$E_{HF} = \sum_i^{\text{elec}} \underbrace{\langle i | \hat{h} | i \rangle}_{\text{One-electron terms}} + \sum_{i > j}^{\text{elec}} \underbrace{[ii | jj]}_{\text{Coulomb terms}} - \underbrace{[ij | ji]}_{\text{Exchange terms}} + E_{NN} \quad (3.13)$$

$$\langle i | \hat{h} | i \rangle = \int d\mathbf{x}_1 \chi_i^*(\mathbf{x}_1) \hat{h}(\mathbf{r}_1) \chi_i(\mathbf{x}_1) \quad (3.14)$$

$$[ii | jj] = \int d\mathbf{x}_1 d\mathbf{x}_2 \underbrace{\chi_i^*(\mathbf{x}_1) \chi_i(\mathbf{x}_1)}_{\text{Mean-field treatment}} \frac{1}{r_{12}} \chi_j^*(\mathbf{x}_2) \chi_j(\mathbf{x}_2) \quad (3.15)$$

$$[ij | ji] = \int d\mathbf{x}_1 d\mathbf{x}_2 \chi_i^*(\mathbf{x}_1) \underbrace{\chi_j(\mathbf{x}_1)}_{\text{Indices} \leftarrow} \frac{1}{r_{12}} \chi_j^*(\mathbf{x}_2) \underbrace{\chi_i(\mathbf{x}_2)}_{\rightarrow \text{exchanged}} \quad (3.16)$$

The subscripts 1 and 2 are dummy indices which stand in for whichever two electrons are considered. The first term in equation 3.13 gives the total KE of the single electrons and their attraction to all of the nuclei. The two-electron integrals on the right hand side are the Coulomb terms and the exchange terms. The Coulomb terms are simply the repulsion between an electron 1 in orbital i and an electron 2 in orbital j . The exchange terms have no direct physical meaning and represent the effects of swapping the orbitals of electrons 1 and 2. From the form of equations 3.15 and 3.16 it can be seen that the

electrons only interact with each other in an average way. Each electron can be thought of as interacting with the probability distribution of the other electrons. The last thing to note is that for case $i = j$ the Coulomb and exchange terms cancel each other out which ensures each electron doesn't interact with itself.

Next E_{HF} needs to be minimised with respect to the orbitals. It is also prudent to enforce the constraint that the orbitals remain orthonormal. The minimisation can be done using the calculus of variations which was touched upon in section 3.1.3. The result is

$$\hat{f}(\mathbf{x}_1) \chi_i(\mathbf{x}_1) = \epsilon_i \chi_i(\mathbf{x}_1) \quad (3.17)$$

$$\hat{f}(\mathbf{x}_1) = \hat{h}(\mathbf{x}_1) + \sum_j \hat{J}_j(\mathbf{x}_1) - \hat{K}_j(\mathbf{x}_1) \quad (3.18)$$

$$\hat{J}_j(\mathbf{x}_1) = \int d\mathbf{x}_2 \chi_j^*(\mathbf{x}_2) \frac{1}{r_{12}} \chi_j(\mathbf{x}_2) \quad (3.19)$$

$$\hat{K}_j(\mathbf{x}_1) \chi_i(\mathbf{x}_1) = \int d\mathbf{x}_2 \chi_j^*(\mathbf{x}_2) \frac{1}{r_{12}} \chi_i(\mathbf{x}_2) \chi_j(\mathbf{x}_1) \quad (3.20)$$

Expression 3.17 is the shorthand form of the HF equations and the equations which follow it expand out the terms in more detail. \hat{f} is the Fock operator, ϵ_i is a diagonal matrix, $\hat{J}_j(\mathbf{x}_1)$ is the coulomb operator and $\hat{K}_j(\mathbf{x}_1)$ is the exchange operator. The HF equations are a complex set of integro-differential equations. They can be simplified by introducing a basis set $\tilde{\chi}$, multiplying by $\tilde{\chi}_\mu^*(\mathbf{x}_1)$ and then integrating to give the Roothaan equations (Expression 3.22 gives the Roothaan equations and the surrounding equations give their expanded form).

$$\chi_i = \sum_{\mu}^K C_{\mu i} \tilde{\chi}_{\mu} \quad (3.21)$$

$$\mathbf{FC} = \mathbf{SC}\epsilon \quad (3.22)$$

$$\sum_{\nu} F_{\mu\nu} C_{\nu i} = \epsilon_i \sum_{\nu} S_{\mu\nu} C_{\nu i} \quad (3.23)$$

$$F_{\mu\nu} = \int d\mathbf{x}_1 \tilde{\chi}_{\mu}^*(\mathbf{x}_1) \hat{f}(\mathbf{x}_1) \tilde{\chi}_{\nu}(\mathbf{x}_1) \quad (3.24)$$

$$S_{\mu\nu} = \int d\mathbf{x}_1 \tilde{\chi}_{\mu}^*(\mathbf{x}_1) \tilde{\chi}_{\nu}(\mathbf{x}_1) \quad (3.25)$$

The problem is now a generalised eigenvalue problem. The matrices are emphasised in bold. \mathbf{F} is the Fock matrix, \mathbf{C} is a matrix of coefficients, \mathbf{S} is the overlap matrix and ϵ is once again a diagonal matrix. The next section illustrates how E_{HF} and in general E_{el} tend to be found in practice.

3.1.7 Self-consistent field solutions

Many problems in computational chemistry need to be solved self-consistently via self-consistent field (SCF) methods. For example, the Roothaan equations can be solved by the following procedure:

- 0) Initial setup: Specify molecule, basis functions, and electronic state of interest (e.g. singlet or triplet). Form \mathbf{S} from the basis functions.
- 1) Guess the matrix of coefficients \mathbf{C} . Form the Fock matrix \mathbf{F} from this guess.
- 2) Solve $\mathbf{FC} = \mathbf{SC}\epsilon$.
- 3) Use new \mathbf{C} in step 1). Repeat until \mathbf{C} no longer changes from one iteration to the next.

In general SCF type methods start from some initial guess which could be nuclear coordinates themselves, an initial guess for the molecular orbital coefficients or an initial guess for the density and so on... An iterative procedure is then followed until self-consistency. For example, when solving the HF equations (3.17) the Fock operator $\hat{f}(\mathbf{x}_1)$ will depend on the molecular orbitals $\chi_i(\mathbf{x}_1)$ which depends on the previous $\hat{f}(\mathbf{x}_1)$. Similarly, in DFT (see section 3.1.12) many of the terms will depend on the density which depends on the Kohn-Sham orbitals which themselves depend on the effective potential which depends on the density.

Extreme care needs to be taken when developing electronic structure optimisation algorithms. Many standard textbook approaches for solving systems of linear equations and diagonalising matrices may require that matrix elements are accessed in a random order which becomes prohibitively difficult as the size of the system increases. In fact, some matrices may be so large that even storing them on a disk may be problematic. In practice, most electronic structure codes need to implement convergence techniques [73, 74] such as direct inversion of the iterative subspace. The convergence techniques used in quantum chemistry are often iterative requiring the repeated evaluation of matrix vector products and they often break the full computational space up into a series of easier to solve subspaces.

3.1.8 The complete basis set limit

The energy obtained in quantum chemical calculations is strongly influenced by the basis set choice. If the basis set is well-chosen and is continually made larger and more complete then there is more flexibility in the expansion which should lead to a better value for the energy. So, in theory, to represent the wave function as precisely as possible an infinitely large and well-chosen basis set would be needed. Reaching this theoretical limit is referred to as the complete basis set (CBS) limit [75, 76]. In practice, at a certain basis set size the energy becomes nearly constant with increasing basis set size and extrapolation techniques are then used to converge the calculation to the CBS limit. An illustration of how the energy may get lower as one approaches this limit (for a HF calculation) is shown in Figure 3.1.

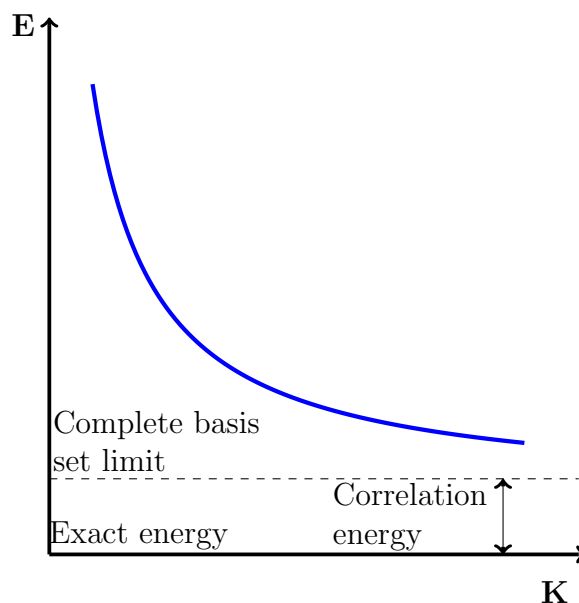


Figure 3.1: Illustration of the complete basis set limit in the Hartree-Fock approach. The basis set size is labelled by \mathbf{K} .

In general only approximate solutions to the Schrödinger equation can be found in quantum chemistry. This means the accuracy of the calculation is limited by whatever assumptions were made in order to reach the solution. In the HF approach it is assumed that the wave function can be represented by a single Slater determinant, as a consequence each electron only interacts with the mean field of the other electrons. There will be no dynamical correlation between them and they will be restricted to be unnecessarily close together. This means that even in the CBS limit the HF approach will always overpredict the true energy ϵ_0 by an amount E_{cor} known as the correlation energy [77].

$$E_{cor} = \epsilon_0 - E_{HF} \quad (3.26)$$

3.1.9 Post Hartree-Fock methods

Post-Hartree-Fock (PHF) methods are a large and important class of *ab initio* quantum chemistry methods used to find the true non-relativistic energy. In most applications PHF methods take an already converged structure as input which was found using another method such as HF or DFT. PHF methods improve on the HF method by explicitly including electron correlation. The basic idea behind many of these methods is to use a basis that is larger than the number of occupied molecular orbitals, with the HF solution being the zeroth order solution and with the task being to search for the higher order solutions. One of the simplest (but not as widely used as methods like Coupled Cluster and Møller–Plesset perturbation theory [66]) PHF methods is the configuration interaction (CI). The CI takes linear combinations of the configuration states Ψ_i each having different occupations of the molecular orbitals and the task is to find the coefficients α_i .

$$\Psi = \alpha_0 \Psi_{HF} + \sum_{singles} \alpha_i^s \Psi_i^s + \sum_{doubles} \alpha_i^d \Psi_i^d + \dots + \sum_{Nexcit} \alpha_i^N \Psi_i^N \quad (3.27)$$

A configuration state is one of the many possible states of the system and the solution can be systematically improved (see [78] for a discussion of size-consistency and size-extensibility) by first considering all the single excitations, then doubles and so on ... In theory, absolutely all possible excitations would have to be considered in order to reach the exact solution. In practice, calculating singles doubles and triples on a given system is likely to give a very accurate energy. If all possible excitations are considered and spin is accounted for then for K basis functions and N electrons the number of possible excitations N_{ext} is

$$N_{ext} = \binom{2K - N}{N} \quad (3.28)$$

where this notation stands for $2K - N$ choose N . The numbers of possible excitations blows up very quickly, take for example water and use $N = 10$ and $K = 24$, there are around $5 * 10^8$ possible combinations.

Using a succession of mean-field methods like HF theory or DFT and PHF methods can provide highly accurate energies for a wide range of chemical systems. However, this hierarchy will fail for systems which are genuinely multi-reference in character i.e. systems whose wave function needs to be expressed in terms of more than one Slater determinant. In this case similar but more flexible methods such as multi-configurational self-consistent field methods need to be applied. Furthermore, mean-field methods also break down when modelling strongly correlated systems. More advanced theories like dynamical mean-field theory allow for a more controlled and reliable description of some of the correlation effects which will inevitably be averaged over in a mean-field regime. The rest of this thesis will use the umbrella term "higher level methods" to refer to methods which capture the full non-relativistic electronic energy correctly.

3.1.10 Scaling of density functional theory with system size

The Hilbert space in quantum chemical systems tends to grow exponentially with system size making numerical solutions increasingly difficult to obtain. In DFT instead of expanding the electronic wave function into $3N$ coordinates like in HF theory the energy is expressed in terms of a functional of the density ρ with only 3 spatial coordinates. The problem of N interacting electrons moving around in an external potential will be mapped to the problem of N non-interacting electrons moving in an effective potential. The original problem will be mapped from something that scales like the number of grid points to the power N ; $(\#gridpoints)^N$, to something that scales like N times the number of grid points; $N * (\#gridpoints)$.

$$\psi(\mathbf{r}_1, \dots, \mathbf{r}_N) \rightarrow \{\psi_1(\mathbf{r}), \dots, \psi_N(\mathbf{r})\}$$

$$(\#gridpoints)^N \rightarrow N * (\#gridpoints)$$

This means the formal scaling of DFT with system size is much better compared to other quantum chemical methods.

Molecular dynamics (classical)	$O(N)/O(N \log N)$
Density functional theory	$O(N^3)$
Hartree-Fock	$O(N^4)$
Coupled Cluster (CCSD(T))	$O(N^7)$

The improved scaling with system size comes at the cost of having to guess the exchange-correlation functional and will place strong limits on the accuracy obtainable with DFT. The gold standard for a method in quantum chemistry is to be able to find chemically accurate energy barriers [79] which is often defined as being within 5 kJ/mol of the true value. DFT regularly fails to meet this standard often having systematic errors above 20 kJ/mol for the reactions studied in this work [80]. DFT's strength lies in the fact that although it has a large associated error this error tends to be systematic and to preserve trends well [61, 81, 82]. Because it preserves trends well while being computationally cheap it is one of the workhorses of computational chemistry. DFT can be used alone in trend studies, or if accurate chemical barriers are essential it can converge the calculation most of the way before being used as the input for higher level methods.

3.1.11 Hohenberg-Kohn theorems

DFTs foundations lie in the Hohenberg-Kohn (HK) theorems [83] which state:

- 1) For any electronic system in an external potential said potential is determined uniquely,
safe for a constant, by the ground state density $\rho_0(\mathbf{r})$.

Corollary 1) Since the Hamiltonian is thus fully determined it follows that the many-body wave functions (ground and excited) and thus all properties are also uniquely determined.

- 2) A universal functional of the energy $E[\rho]$ can be defined in terms of the density ρ , which is valid for any external potential $v_{\text{ext}}(\mathbf{r})$. For any particular $v_{\text{ext}}(\mathbf{r})$ the exact ground state of the system is determined by the global minimum value of this functional.

$$E[\rho] = \int d\mathbf{r} v_{\text{ext}}(\mathbf{r})\rho(\mathbf{r}) + F[\rho] + E_{NN} \quad (3.29)$$

The HK functional is *a priori* unknown, so in a nutshell the size of the problem is reduced at the expense of introducing a term $F[\rho]$ which must be guessed. $F[\rho]$ is universal because all systems have the term, the first term in equation 3.29 is system dependent due to $v_{\text{ext}}(\mathbf{r})$. As is HF theory the last term accounts for the interaction of the nuclei and is a constant. HK-DFT is in principle exact with no approximations being necessary but is impractical to solve. The overwhelming majority of DFT calculations are carried out using Kohn-Sham (KS) DFT [84] which is explored in the next section.

3.1.12 Kohn-Sham equations

In KS-DFT it assumed that the system behaves like a fictitious system of non-interacting electrons which move around in an external potential v_{eff} called the KS potential. The multi-electron density $\rho(\mathbf{r})$ and the KE term are written in terms of the KS orbitals $\phi_i(\mathbf{r})$.

$$\rho(\mathbf{r}) = \sum_i^N |\phi_i(\mathbf{r})|^2 \quad (3.30)$$

$$F[\rho] = \underbrace{\sum_{i=1}^N \int d\mathbf{r} \phi_i^*(\mathbf{r}) \left(-\frac{\hbar^2}{2m} \nabla^2 \right) \phi_i(\mathbf{r})}_{T_s[\rho]} + \underbrace{\frac{e^2}{2} \int d\mathbf{r} \int d\mathbf{r}' \frac{\rho(\mathbf{r})\rho(\mathbf{r}')}{|\mathbf{r} - \mathbf{r}'|}}_{E_H[\rho]} + E_{\text{xc}}[\rho] \quad (3.31)$$

$$E_{\text{xc}}[\rho] = \underbrace{(T[\rho] - T_s[\rho])}_{\text{real KE}} + \underbrace{(E_{ee}[\rho] - E_H[\rho])}_{\text{real exchange}} \quad (3.32)$$

Here $T_s[\rho]$ is the KE of the fictitious system of non-interacting particles, $E_H[\rho]$ is the Hartree energy which accounts for the Coulomb repulsion between the electrons, and

$E_{xc}[\rho]$ is the exchange-correlation energy. Using the above formalism $E[\rho]$ is in principle exact with all terms except $E_{xc}[\rho]$ already being known. However, $E_{xc}[\rho]$ is only known exactly for the free electron gas, otherwise it must be guessed. It can be interpreted as containing the contributions of detailed correlation and exchange. $E_{xc}[\rho]$ should account for missing parts of the KE which was approximated using the KS orbitals and the missing interaction between the electrons which has been approximated by $E_H[\rho]$. In HF theory exact exchange is explicitly included and all terms corresponding an electron interacting with itself cancel out. This property will not be present in DFT and there will an associated self-interaction error.

The energy is minimised via a variational procedure (see reference [85] for details of the derivation) which yields the KS equations (expression 3.33)

$$\left(-\frac{\hbar^2}{2m} \nabla^2 + v_{\text{eff}}(\mathbf{r}) \right) \phi_i(\mathbf{r}) = \varepsilon_i \phi_i(\mathbf{r}) \quad (3.33)$$

$$v_{\text{eff}}(\mathbf{r}) = v_{\text{ext}}(\mathbf{r}) + e^2 \int \frac{\rho(\mathbf{r}')}{|\mathbf{r} - \mathbf{r}'|} d\mathbf{r}' + \underbrace{\frac{\delta E_{xc}[\rho]}{\delta \rho(\mathbf{r})}}_{v_{xc}(\mathbf{r})} \quad (3.34)$$

A complex N-particle problem which may or may not be soluble is mapped to N one dimensional Schrödinger-like equations which are easily solved. All terms in $v_{\text{eff}}(\mathbf{r})$ are already known except for the exchange-correlation potential $v_{xc}(\mathbf{r})$ which includes all the many-body interactions. δ denotes a functional derivative. There is still debate about whether the KS energies ε_i are physically meaningful [86, 87] on their own. When they are summed they are related to the total energy E via

$$E = \sum_i^N \varepsilon_i - E_H[\rho] + E_{xc}[\rho] - \int \frac{\delta E_{xc}[\rho]}{\delta \rho(\mathbf{r})} \rho(\mathbf{r}) d\mathbf{r} \quad (3.35)$$

3.1.13 Choice of functional

There is no guarantee that $E_{xc}[\rho]$ will have a simple form. In fact, over 20 years passed between the KS equations being published and accurate enough functionals such as for example, the B3LYP [88, 89] functional being developed. Nowadays a zoo of different density functionals are in active use (for an in-depth overview of commonly used density functionals a see reference [82])). They can use many different levels of approximation

$$\begin{aligned} E_{xc} &= f[\rho(\mathbf{r})] && \text{(Local density approximation)} \\ E_{xc} &= f[\rho_\alpha(\mathbf{r}), \rho_\beta(\mathbf{r})] && \text{(Local spin density approximation)} \\ E_{xc} &= f[\rho_\alpha(\mathbf{r}), \rho_\beta(\mathbf{r}), \nabla \rho_\alpha(\mathbf{r}), \nabla \rho_\beta(\mathbf{r})] && \text{(Generalised gradient approximation)} \\ E_{xc} &= f[\rho_\alpha(\mathbf{r}), \rho_\beta(\mathbf{r}), \nabla \rho_\alpha(\mathbf{r}), \nabla \rho_\beta(\mathbf{r}), K(\mathbf{r})] && \text{(Hybrid)} \\ E_{xc} &= f[\rho_\alpha(\mathbf{r}), \rho_\beta(\mathbf{r}), \nabla \rho_\alpha(\mathbf{r}), \nabla \rho_\beta(\mathbf{r}), K(\mathbf{r}), \tau(\mathbf{r})] && \text{(Meta)} \end{aligned}$$

Here f stands for a functional which can depend on $\rho(\mathbf{r})$, $\nabla \rho(\mathbf{r})$, the spins α and β , exact exchange $K(\mathbf{r})$ from HF theory and the KE density $\tau(\mathbf{r})$.

The methodology for improving density functionals is more loose than *ab initio* many-body methods like Coupled Cluster theory or Møller–Plesset perturbation theory where the higher the order of the perturbations or excitation operators considered the more accurate the result should be expected to be. Which functional performs best can be very system specific and using a more advanced functional may not always improve the result obtained. To choose the functional for a given system one has to know where to apply a given functional along with knowledge of which systems it has been benchmarked against and shown to work for [90–92].

In this work the Perdew–Burke–Ernzerhof (PBE) functional [93, 94] is mainly utilised. It is a popular choice because, although it is not as accurate as many hybrid functionals or higher level methods, it tends to reproduce trends well and to underestimate energies in a systematic manner. It belongs to a class of non-empirical functionals which try to only use general rules of quantum mechanics and special limiting conditions to determine the parameters in as general a form possible. In contrast hybrid functionals are often fitted in some manner to external parameters. In doing so they can lose some of their generality and arguably their physical meaningfulness but gain more accuracy [95, 96].

3.1.14 Plane wave basis sets

In periodic systems like zeolites it is useful to use a basis set made up of plane waves. Many authors also study zeolites with atom centered basis sets where part of the crystal structure is cut out and the under-coordinated terminal atoms are bonded to additional hydrogens. In a periodic systems Bloch’s theorem can be used to write the wave function Ψ as a plane wave $e^{i\mathbf{k}\cdot\mathbf{r}}$ modulated by a periodic function $u(\mathbf{r})$ where \mathbf{r} is the position in real space and \mathbf{k} is the wave vector in reciprocal space

$$\Psi = e^{i\mathbf{k}\cdot\mathbf{r}}u(\mathbf{r}) \quad (3.36)$$

The wave functions are expanded in terms of plane waves via the relation

$$\Psi_{i,\mathbf{k}}(\mathbf{r}) = \frac{1}{\sqrt{V}} \sum_{\mathbf{G}} c_{\mathbf{G};i,\mathbf{k}}(\mathbf{G}) e^{i(\mathbf{G}+\mathbf{k})\cdot\mathbf{r}} \quad (3.37)$$

where V is the volume of the unit cell and \mathbf{G} stands for the reciprocal lattice vectors which define a grid centred around the point \mathbf{k} and $c_{\mathbf{G};i,\mathbf{k}}(\mathbf{G})$ are the coefficients. In many systems many \mathbf{k} -points are needed in order to get an accurate result and the symmetries of the system are often exploited to gain quicker convergence. In zeolites however, it is common to sample only the Γ point because the large unit cell in real space leads to a small unit cell in reciprocal space. At some point when adding plane waves with higher and higher KE the energy should converge. The expansion is usually cut off at some energy E_{cut} so that all plane waves with KE less than E_{cut} are included

$$\frac{1}{2}|\mathbf{G} + \mathbf{k}|^2 < E_{cut} \quad (3.38)$$

The number of planes waves $N_{\mathbf{G}}$ required can be estimated by comparing the volume of a sphere containing all plane waves to the fineness of the grid \mathbf{G} , the result is

$$N_{\mathbf{G}} \sim V E_{cut}^{\frac{3}{2}} \quad (3.39)$$

3.1.15 Pseudopotentials

In general wave functions oscillate most rapidly near the atomic nuclei and so a computationally costly number of plane waves are needed to capture these oscillations. In the majority of the chemical interactions the core electrons are tightly bound to the nucleus and play a minor role compared to the valence electrons. The valence electrons experience the nuclear core as being screened by the core electrons i.e. they experience a potential that is much smoother than that of the bare nucleus alone. In order to avoid going to the expense of computing this screening every time the "true" atomic potentials can be replaced with pseudopotentials [97] which manually mimic it. A pseudopotential represents how the wave functions interact with the combination of nucleus plus core electrons.

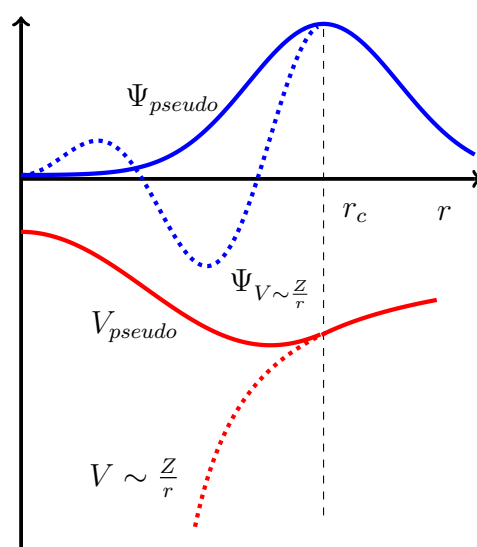


Figure 3.2: Simple scheme showing the "true" potentials and wave functions and the "pseudo" potentials and wave functions. Potentials are shown in red, wave functions in blue. The "true" solutions are shown dotted and the "pseudo" solutions with a full line. The cut-off radius above which the system should behave like the all electron system is r_c .

Space can be divided into core regions which are contained within spheres centered around each of the atoms and the interstitial region which consists of the rest of the unit cell. It is demanded that at a certain radius r_c that the wave functions for the two regions must match up [98] and that in general as many of the properties as possible of the all-electron calculation are maintained outside the core regions. Figure 3.2 presents a simple scheme for a single nuclear core showing both the pseudopotential and an augmented wave function. Usually the core regions are regarded as fixed and non-polarisable in what is termed the frozen core approximation. It is possible to relax this by self-consistently updating the pseudopotential within the chemical environment that it is embedded in but it is rarely done. The projector augmented wave (PAW) method [99, 100] generalises the use of pseudopotentials and linear augmented plane waves. It is a method for reconstructing the all-electron wave-functions from the pseudo wave functions and is used throughout this work.

3.1.16 Grimme's D3 correction

Standard KS-DFT is able to approximately account for much of the interaction between the electrons. However it is unable to account for London dispersion forces.

$$E_{\text{int}} = \underbrace{E_{\text{Pauli-rep}} + E_{ES} + E_{\text{pol}} + E_{\text{disp-short}}}_{\text{included in KS-DFT}} + \underbrace{E_{\text{disp-London}}}_{\text{missing}} \quad (3.40)$$

London dispersion forces are long ranged and result from small fluctuations in time of the electron density around a given atom or molecule. The fluctuations in the electronic density induce instantaneous dipoles and multipoles in nearby atoms and molecules which themselves can go on to cause more fluctuations. The fluctuations can be thought of as excitations to virtual orbitals which are by definition difficult to take account of with a ground-state theory such as standard KS-DFT. Taking the simplest example of two molecules in a box, at very far away distance they do not interact at all. At a closer distance they can induce instantaneous multipoles in each-other and hence attract each other, when they are very close the interactions become repulsive.

If ones chosen functional does not have dispersion corrections [101] somehow already built in (e.g. via fitting to benchmark data like in the BEEF-vdW functional [102]) then a popular choice is to use Grimme's dispersion correction [103]. The latest version as of writing is the D4 family of corrections. This work uses the D3 family which has been in use for far longer. Grimme's dispersion correction E_{disp} is semi-empirical and can simply be added to the energy obtained from KS-DFT.

$$E_{\text{DFT-disp}} = E_{\text{KS-DFT}} + E_{\text{disp}} \quad (3.41)$$

$$E_{\text{disp}} = -\frac{1}{2} \sum_{i=1}^{N_{\text{at}}} \sum_{j=1}^{N_{\text{at}}} \sum_{\mathbf{L}}' \left(f_{\text{damp},6}(r_{ij,L}) \frac{C_{6ij}}{r_{ij,L}^6} + f_{\text{damp},8}(r_{ij,L}) \frac{C_{8ij}}{r_{ij,L}^8} \right) \quad (3.42)$$

All atoms and all translations of the unit cell \mathbf{L} are summed over, the prime indicates that when $\mathbf{L} = 0$, $i \neq j$. The expansion is cut off at order 8 and only two body terms are considered. The coefficients C_{6ij} and C_{8ij} depend on the atoms types themselves and the coordination number around atoms i and j and the damping functions $f_{\text{damp},n}(r_{ij})$ scale the force field in a way that minimises the contributions from interactions that are within typical bonding distances.

The zero-damping [104] damping function is

$$f_{\text{damp},n}(r_{ij}) = \frac{s_n}{1 + 6(r_{ij}/(s_{R,n}R_{0ij}))^{-\alpha_n}} \quad (3.43)$$

$$R_{0ij} = \sqrt{\frac{C_{8ij}}{C_{6ij}}} \quad (3.44)$$

with the values α_6 , α_8 , s_6 and $s_{R,8}$ being fixed and the values s_8 and $s_{R,6}$ being adjustable and functional dependent. Another popular choice for the damping function is Beck-Johnson (BJ) [105] damping where the damping functions $f_{\text{damp},n}(r_{ij})$ change to

$$f_{\text{damp},n}(r_{ij}) = \frac{s_n r_{ij}^n}{r_{ij}^n + (a_1 R_{0ij} + a_2)^n} \quad (3.45)$$

with s_6 being fixed and a_1 and a_2 being adjustable parameters. Typically, the type of damping function used in the dispersion correction does not influence the result significantly. Figure 3.3 presents the dispersion correction for a system of two Argon atoms for the undamped, zero-damped and BJ damped cases.

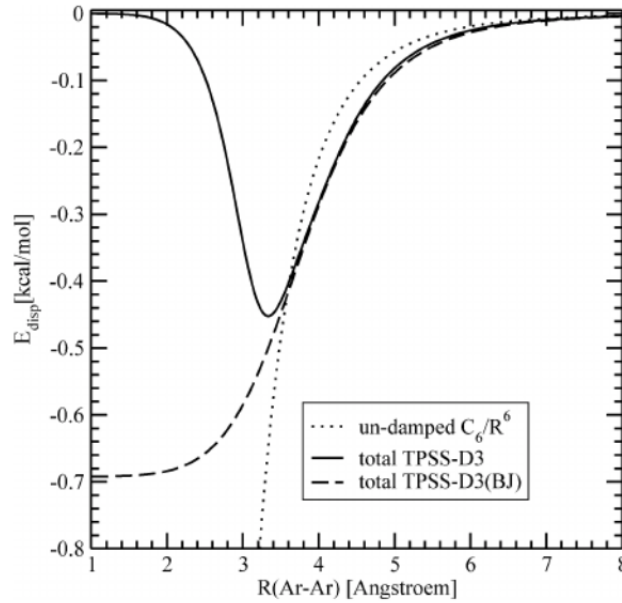


Figure 3.3: Reprinted from [106], Copyright (2011), with permission from John Wiley and Sons. "Dispersion correction for two argon atoms. with the zero- and BJ-damping methods in comparison with the un-damped $-C_6 \cdot R^{-6}$ term."

3.2 Characteristics of energy surfaces

3.2.1 Geometry optimisation

Section 3.1.7 demonstrated how the electronic structure can be found self-consistently and section 3.1.10 showed that DFT calculations scale very well with the system size compared to other methods. However, they are not by any means computationally cheap with efficient optimisation methods which minimise the number of calculation steps needed being extremely beneficial. There are a large variety of different optimisation schemes such as gradient descent (GD), Newton's method, the conjugate gradient method and trust-region methods. The most intuitive of these methods is GD where the direction of steepest is found at each point before travelling along this direction for a certain step size and repeating.

To confirm a local minimum has been reached the eigenvalues of the Hessian matrix must be analysed.

$$H_{i,j} = \frac{\partial^2 E}{\partial \mathbf{x}_i \partial \mathbf{x}_j} \quad (3.46)$$

where i and j run over the degrees of freedom with the full expression for a given point \mathbf{x}_k on the surface given by the second order Taylor expansion

$$E(\mathbf{x}_k + \Delta \mathbf{x}) \approx E(\mathbf{x}_k) + \nabla E(\mathbf{x}_k)^T \Delta \mathbf{x} + \frac{1}{2} \Delta \mathbf{x}^T H(\mathbf{x}_k) \Delta \mathbf{x} \quad (3.47)$$

(for simplicity a subscript is used for both indexes i and j which refer to the coordinates and to mark a given point \mathbf{x}_k). The task is to look for first order saddle points with one negative eigenvalue in the Hessian matrix. Taking the gradient of the Taylor series above yields

$$\nabla E(\mathbf{x}_k + \Delta \mathbf{x}) = \nabla E(\mathbf{x}_k) + H \Delta \mathbf{x} \quad (3.48)$$

This is known as the secant equation. Setting the first term to zero a \mathbf{H} needs to be found that satisfies

$$\Delta \mathbf{x} = -H^{-1} \nabla E(\mathbf{x}_k) \quad (3.49)$$

In practice the Broyden–Fletcher–Goldfarb–Shanno (BFGS) algorithm [107] is among the most commonly used optimisation algorithms for solving such problems. More often than not it converges in far fewer steps than GD, it is accurate, it has very stable performance and it is fast. The BFGS algorithm belongs to the class of quasi-Newton methods (QNM) which navigate around the computational expenses associated with Newton type methods. In Newton type methods either Jacobian or the Hessian matrix needs to be inverted which can very costly when done at every step. In QNM the matrix inversion is done iteratively, for example, in the BFGS algorithm the Hessian is found via:

$$H_{k+1} = \left(I - \frac{\Delta \mathbf{x}_k \mathbf{y}_k^T}{\mathbf{y}_k^T \Delta \mathbf{x}_k} \right) H_k \left(I - \frac{\mathbf{y}_k \Delta \mathbf{x}_k^T}{\mathbf{y}_k^T \Delta \mathbf{x}_k} \right) + \frac{\Delta \mathbf{x}_k \Delta \mathbf{x}_k^T}{\mathbf{y}_k^T \Delta \mathbf{x}_k} \quad (3.50)$$

$$\mathbf{y}_k = \nabla E(\mathbf{x}_{k+1}) - \nabla E(\mathbf{x}_k) \quad (3.51)$$

A common convergence criteria for the forces is

$$\max_a |\vec{F}_a| < f_{\max} \quad (3.52)$$

The index a labels the different atoms. The above expression requires that all components of the total force $|\vec{F}|$ are less than some tolerance f_{\max} . A good rule of thumb is that 0.05 eV per Å for f_{\max} is considered acceptable however 0.01 is more desirable.

Such an optimisation procedure defines how to find a local minimum. Although chemical intuition is useful for determining whether the final structure obtained is reasonable some doubt will always remain as to whether there is a more stable local minima which is yet to be found. Some methods exist which aim to explore the computational space more systematically e.g. minima hopping algorithms [108].

3.2.2 Transition state searching

The product $k_B T$ is often used as a scale factor in systems because for many phenomena the rate depends on the ratio $E/k_B T$. For a reaction temperature of 400 °C this gives a result of 0.06 eV for $k_B T$. Barriers for chemical and diffusive processes are typically of the order 1 eV, in this case that the exponential factor will be of the order 10^{-8} and (assuming a typical prefactor) the rate will be of the order 10^5 s^{-1} . In comparison the typical timestep used in Molecular dynamics (MD) simulations is on the fs scale (10^{-15} s). It's clear that on average the time it would take to observe just one transition state (TS) event is extremely large. TSs are extremely rare events on the atomic scale.

TSs can be found by searching along the minimum energy path (MEP) between two minima and looking for first order saddle points. It should be confirmed that normal mode corresponding to the negative eigenvalue of the Hessian matrix moves along the RP (reaction path). In general TSs are much more difficult to find than minima with the search process often requiring more input and very good starting guesses. When applying most TS searching methods the structure needs to be constrained in some manner in order to keep it from relaxing back towards a local minima. The constraint could be for example fixing bond lengths, fixing an atom in all 3 spatial coordinates or fixing an atom in a given plane and so on ... If appropriate constraints for the RP are chosen then it is possible to climb up the potential energy surface (PES) until the force is sufficiently converged. Some methods such as the nudged elastic band (NEB) [109, 110] and the dimer method [111] aim to avoid the need for the user to explicitly specify the constraints and in principle find every type of TS without any chemical intuition. In practice however, knowledge of how the system moves along the RP and how interpolations of the MEP should look can help guide the calculation. The methods mainly used in this work are the NEB method, the dimer method, PES scans and Automated Relaxed Potential Energy Surface Scans (ARPES)[112].

PES scans can be understood in terms of the projected gradient \mathbf{g}_i^\perp [113] which projects out any movements that are parallel to the RP and so keeps the structure fixed along the RP.

$$\mathbf{g}_i^\perp = (I - \tau_i \tau_i^T) \mathbf{g}_i \quad (3.53)$$

Here τ_i is the tangent at point \mathbf{r}_i along the RP. If the constraint is chosen well then a scan can be done for a given grid spacing before taking the topmost parts of the scan and performing tighter and tighter scans. This works very well for simple reactions where the change in the structure as one moves along the MEP is well approximated by the chosen constraint. For more complex reactions however, it may be difficult to choose an appropriate constraint.

In such a case a more suitable choice would perhaps be the NEB method. In the NEB method the MEP is found by automatically adding fictitious springs between the different structures/images along the path. These springs have no physical meaning and only serve as a means of keeping the spacing between the structures. A given number of images along the RP must be specified as an initial guess for the MEP with the initial state and final state being the end points. Often this is done via an interpolation but can also be done by hand. The total force is the sum of fictitious spring forces \mathbf{f}_i^\parallel which are parallel to the local tangent and the components of the true forces \mathbf{g}_i^\perp perpendicular to the tangent

$$\mathbf{f}_i = \mathbf{f}_i^\parallel - \mathbf{g}_i^\perp \quad (3.54)$$

$$\mathbf{f}_i^\parallel = k [((\mathbf{r}_{i+1} - \mathbf{r}_i) - (\mathbf{r}_i - \mathbf{r}_{i-1})) \cdot \tau_i] \tau_i \quad (3.55)$$

the images are "nudged" by the spring forces not to move along the parallel direction and are relaxed along the perpendicular direction until the true forces reach the desired convergence criteria. The NEB path, when plotted in terms of reaction coordinate and energy eventually wraps round the MEP like an elastic band. After the NEB is sufficiently close to the true MEP the uppermost image can be pushed upward via changing the force on it to

$$\mathbf{f}_{i_{max}} = -\nabla E(\mathbf{R}_{i_{max}}) + 2(\nabla E(\mathbf{R}_{i_{max}}) \cdot \tau_{i_{max}}) \tau_{i_{max}} \quad (3.56)$$

This small alteration to the NEB method is known as the climbing image nudged elastic band method [114]. Without the climbing image the accuracy is limited by how close the highest image is to the TS. The NEB method is remarkably robust but can suffer, for example, from a bad initial interpolation, not using enough images or a RP which is too long. The method relies on the user to input a start point and an endpoint, which may not be easy to find for some reactions, fixing the endpoints also imposes some bias on which TSs can be found. Furthermore, it is a can be computationally expensive, especially in systems with a complex PES. The dimer method complements the NEB by avoiding some of these problems.

In the dimer method a literal dimer made up of two images is walked along the lowest curvature normal mode of the system up towards the TS. The main two steps are to 1) Rotate the dimer along the lowest curvature mode which is equivalent to minimising its energy. 2) Translate upwards along this mode. In complex systems reactions can often

take place via unexpected or unknown mechanisms. The dimer is ideal here because it can find many saddle points that are *a priori* difficult to take into account. However, the method requires a very good starting guess to converge to the TS which one desires. It is also, in many cases, not as robust as the NEB and may, if it converges at all, end up converging to an undesired saddle point.

In the ARPES method the RP is automatically scanned through. This method is very fast because it uses an adaptive step to determine the next value of the constraint. In contrast the PES scans described earlier often use evenly spaced grids which in many cases are manually added with progressively tighter spacing. The constraint chosen is a linear combination of bond distances. It is a good method to apply whenever bonds are formed and broken and performs particularly well for simple S_N1 and S_N2 type reactions. No interpolations are needed like in the NEB and the initial guess does not have to be as accurate as in the dimer method.

3.2.3 Vibrational analysis

Hessian vibrational analysis (HVA) [115] is used to capture the periodic motions in chemical and physical systems. In most applications a converged electronic structure calculation is used as the input for the HVA which provides information about the normal modes of the system and their corresponding frequencies. The normal modes could characterise for example, how a reactant moves along a reaction coordinate or the vibration of a bond. HVA is essential to confirm that TSs are well converged and is the main input for thermodynamic analysis.

Some of the key steps in finding the normal modes include the construction of the Hessian matrix (equation 3.46) transforming to mass weighted coordinates and transforming to normal coordinates. The final output will be $3N-6$ non zero normal modes (or $3N-5$ for linear molecules, translational and rotational modes yield an eigenvalue of zero) of the system and their corresponding frequencies. In many cases the vibrational analysis is carried out numerically using a finite difference approximation but in some electronic structure codes it can be done fully analytically [116]. A large majority of theoretical studies use partial Hessian vibrational analysis (PHVA) instead of full HVA. This is because the calculation quickly becomes expensive as the size of the Hessian matrix increases. In PHVA vibrational modes are found only for the atoms which are most relevant which is reasonable as long as the modes of interest are only weakly coupled to the other modes. For example, when considering an adsorbate on a surface, the vibrational modes associated with the surface are somewhat irrelevant, the vibrational modes of the adsorbate itself are of much more importance.

3.3 Thermochemistry

The previous sections were mainly concerned with the properties which can be calculated directly from an electronic structure calculation, most importantly, the electronic energy E_{elec} . Although differences in E_{elec} alone are sufficient to make predictions in many chemical systems the Gibbs free energy is, of course, more universally applicable. It is given by

$$G(P, T) = H - TS \quad (3.57)$$

where H is the enthalpy and S is the entropy. Quantum statistical mechanics (QSM) is usually used to calculate thermodynamic quantities from electronic structure calculations [117, 118] because it elegantly expresses macroscopic thermodynamic variables in terms of microscopic degrees of freedom. It should be noted however that there are many ways to sample the possible microstates in more detail than is presented here, such as for example, methods based upon MD simulations.

The theory that follows is derived by applying QSM using the vibrational modes discussed in section 3.2.3 as the input. The electronic structure calculation provides the energy E_{elec} at $T = 0$ K and both the thermal and the zero-point energy (ZPE) corrections [119] will be added in. In this work there are two main ways in which thermodynamic corrections are made 1) in the harmonic limit where all $3N$ degrees of freedom are treated harmonically which is used for adsorbates and TSs and 2) in the ideal gas limit for gases. The corrections in the latter are in many cases significantly larger than in the former.

3.3.1 The Harmonic limit

The harmonic approach is the simplest way to calculate the Gibbs free energy G . It is used when there are no significant rotational and translational degrees of freedom as is often the case for adsorbates and TSs. Because the term PV is essentially constant for the systems studied in this work and we are mainly interested in energy differences, G can be approximated by the Helmholtz free energy F (in other applications PV could change significantly between reactant and product e.g. if the lattice parameter changes significantly).

$$F(T) = U(T) - TS(T) \quad (3.58)$$

$$G = F + PV \quad (3.59)$$

$U(T)$ and S are related to the vibrational modes ω_i via the following

$$U(T) = E_{\text{elec}} + E_{\text{ZPE}} + \sum_i^{\text{harm DOF}} \frac{\epsilon_i}{e^{\epsilon_i/k_B T} - 1} \quad (3.60)$$

$$S = k_B \sum_i^{\text{harm DOF}} \left[\frac{\epsilon_i}{k_B T (e^{\epsilon_i/k_B T} - 1)} - \ln(1 - e^{-\epsilon_i/k_B T}) \right] \quad (3.61)$$

$$\epsilon_i = h\omega_i \quad (3.62)$$

The only unfamiliar term in the previous expressions is the ZPE E_{ZPE} , it is a purely quantum in nature and is strongly related to the uncertainty principle. By definition it is difficult to measure experimentally but can easily be expressed in terms of the vibrational modes via the following

$$E_{\text{ZPE}} = \sum_i^{\text{vib DOF}} \frac{h\omega_i}{2} \quad (3.63)$$

Computing the ZPE is important whenever the sum above is significantly different between reactants and products, for example when a high frequency mode in the reactants is broken but not replaced in the products.

Another important observation is that the entropic contribution is dominated by the low frequency modes and thus extremely sensitive to numerical inaccuracies. If the Harmonic approximation is applied to particularly loosely bound or large species it is well documented that spurious imaginary frequencies can arise because the modes are too "floppy" [120]. To remedy this it is common practice to replace all real frequencies under 12 cm^{-1} and all imaginary frequencies by 12 cm^{-1} . This value is chosen because it is approximately the translational frequency of a particle in a box [41].

3.3.2 The ideal gas limit

Calculating $G(T, P)$ is more complicated for gases due to the contributions from the rotational and vibrational degrees of freedom. Now the entropy $S(T, P)$ explicitly depends on P .

$$G(T, P) = H(T) - T S(T, P) \quad (3.64)$$

First let's consider the enthalpy H as a function of temperature which at constant pressure is given by

$$H(T) = E_{\text{elec}} + E_{\text{ZPE}} + \int_0^T C_P dT \quad (3.65)$$

The contribution from the heat capacity C_P is in most cases far smaller than from the ZPE and can be expressed in terms of the translational, rotational, vibrational and electronic degrees of freedom

$$C_P = k_B + C_{V,\text{trans}} + C_{V,\text{rot}} + C_{V,\text{vib}} + C_{V,\text{elec}} \quad (3.66)$$

(the extra factor of k_B comes from using Mayer's relation). The vibrational modes (which are most easily expressed in an already integrated form) can be found via

$$\int_0^T C_{V,\text{vib}} dT = \sum_i^{\text{vib DOF}} \frac{\epsilon_i}{e^{\epsilon_i/k_B T} - 1} \quad (3.67)$$

The entropy S is also found using a simple sum

$$\begin{aligned} S(T, P) &= S(T, P^\circ) - k_B \ln \frac{P}{P^\circ} \\ &= S_{\text{trans}} + S_{\text{rot}} + S_{\text{elec}} + S_{\text{vib}} - k_B \ln \frac{P}{P^\circ} \end{aligned} \quad (3.68)$$

where P° is the reference pressure. The electronic, and vibrational component are given by

$$S_{\text{vib}} = k_{\text{B}} \sum_i^{\text{vib DOF}} \left[\frac{\epsilon_i}{k_{\text{B}}T (e^{\epsilon_i/k_{\text{B}}T} - 1)} - \ln(1 - e^{-\epsilon_i/k_{\text{B}}T}) \right] \quad (3.69)$$

$$S_{\text{elec}} = k_{\text{B}} \ln [2 \times (\text{total spin}) + 1] \quad (3.70)$$

The translational and rotational components are given by

$$S_{\text{trans}} = k_{\text{B}} \left\{ \ln \left[\left(\frac{2\pi M k_{\text{B}}T}{h^2} \right)^{3/2} \frac{k_{\text{B}}T}{P^\circ} \right] + \frac{5}{2} \right\} \quad (3.71)$$

$$S_{\text{rot}} = \begin{cases} 0 & , \text{ if monatomic} \\ k_{\text{B}} \left[\ln \left(\frac{8\pi^2 I k_{\text{B}}T}{\sigma h^2} \right) + 1 \right] & , \text{ if linear} \\ k_{\text{B}} \left\{ \ln \left[\frac{\sqrt{\pi I_A I_B I_C}}{\sigma} \left(\frac{8\pi^2 k_{\text{B}}T}{h^2} \right)^{3/2} \right] + \frac{3}{2} \right\} & , \text{ if nonlinear} \end{cases} \quad (3.72)$$

Here the molecules have been treated as rigid rotors where I_A , I_B and I_C are the three principle moments of inertia for a non-linear molecule, I is the degenerate moment of inertia for a linear molecule and σ is the symmetry number of the molecule in question.

3.4 Kinetic modelling

3.4.1 Transition state theory

Chemical and diffusive processes occur when traversing between local minima on the PES and are often accompanied by an energy barrier. The aim of transition state theory (TST) is to calculate the rate at which reactants go from the reactant region R to the product region P via crossing a dividing surface TS .



Some of the key assumptions made are (see reference [121] for a derivation):

0) The dynamics happen on a PES (this comes from the BO approximation).

1) TS is in a quasi-equilibrium with R (This comes from assuming that the system can be treated by statistical mechanics. Thus the Boltzmann distribution can be used to calculate the probability of finding the system with a given total energy.)

2) There are no recrossings back over TS (This comes from assuming there is a finite velocity into P).

The final result is that

$$k_{TST} = \frac{k_B T}{h} \frac{q^{TS}}{q^R} = \frac{k_B T}{h} e^{-\frac{\Delta G}{k_B T}} \quad (3.74)$$

where q stands for partition function and k_{TST} is the rate. In harmonic TST it is further assumed that the PES can be represented harmonically which is reasonable as long as the extrema are well represented by a second order Taylor expansion. In harmonic TST the main information required to calculate k_{TST} comes from two points TS and R where TS is a saddle point and R is a local minima. In many applications harmonic TST yields a rate k_{TST} which is a robust estimation of the true rate k_{exact} . However, in general

$$k_{TST} > k_{exact} \quad (3.75)$$

In variational TST [122] the position of TS is varied in order to get as close as possible to k_{exact} . The rate of recrossings can be dynamically corrected by finding the transmission coefficient $\kappa(T)$.

$$k_{exact} = \kappa(T) k_{TST} \quad (3.76)$$

$$\kappa(T) < 1 \quad (3.77)$$

A value for $\kappa(T)$ can be obtained by following the trajectory of the system for a very short time period compared to the time it takes to pass over the TS but long enough to observe the recrossings [121].

3.4.2 Microkinetic modelling

A reversible elementary reaction can be described by the equation



where ν_i and ν_j are stoichiometric coefficients and R_i and P_j are the reactants and products. The rate of a forward reactions r can be expressed as

$$r = k * \prod_{\alpha,\beta} \theta_\alpha^{\nu_\alpha} * p_\beta^{\nu_\beta} \quad (3.79)$$

where θ_α are the coverages of the surface reactants and p_β are the pressures of the gas phase reactants and k is the rate constant which can be found via equation 3.74. By setting the forward rate equal to the backwards rate the equilibrium constant K can be found where

$$K = \frac{k_{\rightarrow}}{k_{\leftarrow}} = \prod_{\alpha,\beta,\gamma,\delta} \frac{\theta_\gamma^{\nu_\gamma} p_\delta^{\nu_\delta}}{\theta_\alpha^{\nu_\alpha} p_\beta^{\nu_\beta}} \quad (3.80)$$

Here γ and δ label the coverages and pressures of the products. More generally the reaction quotient is defined as

$$Q_r = \frac{\prod_j a_j^{\nu_j}}{\prod_i a_i^{\nu_i}} \quad (3.81)$$

where a_i are the activities which can often be related to the concentrations/pressures via some activity coefficient. The standard free energy of a reaction ΔG_r^\ominus can be calculated via

$$\Delta G_r^\ominus = \sum_j \nu_j \Delta G_{j,f}^\ominus - \sum_i \nu_i \Delta G_{i,f}^\ominus \quad (3.82)$$

where j runs over the products, i over the reactants and the subscript f indicates these are the standard free energies of formation which can be found from thermodynamic tables. ΔG_r can be found at any conditions via the relation

$$\Delta G_r = \Delta G_r^\ominus + RT \ln Q_r \quad (3.83)$$

where R is the universal gas constant. At equilibrium $\Delta G_r = 0$ and $Q_r = K$ yielding the reaction isotherm equation

$$\frac{\Delta G_r^\ominus}{T} = -R \ln K \quad (3.84)$$

Subbing back into equation 3.83 yields

$$\Delta_r G = RT \ln\left(\frac{Q_r}{K}\right) \quad (3.85)$$

For a deeper background on kinetics see references [123–125].

So if $Q > K$ the reaction proceeds forwards and if $Q < K$ it proceeds backwards. Common reactor types include batch reactors, continuous-flow stirred tank reactors and plug flow reactors. Batch reactor are governed by the simple differential equation

$$\frac{dN_i}{dt} = V_R * r_i = S_R * \Omega_i \quad (3.86)$$

where N_i is number of species i . V_R is the volume of the reactor in which the reactants are held for time t and r_i is the rate of formation of species i . S_R is the number of catalytic sites in the reactor and Ω_i is the turnover frequency for species i .

3.4.3 Kinetic Monte Carlo

Standard KS-DFT finds the ground state of the system with no time evolution involved. Other computational methods such as MD are able to evolve the system with time but the phenomena which they can be applied to is limited by the fact that the time step used in the simulation has to be linked to the lowest frequency mode of the system. This means that in the absence of steering they are in most cases unable to simulate TS events with high barriers. Kinetic Monte carlo (kMC) is a simple way of simulating systems on larger time scales which takes predetermined rate constants as the input. The rate constants may come theoretical simulations at lower length scales or from experiment. The dynamics of the system are reproduced by using coarse grained hops as illustrated in Figure 3.4.

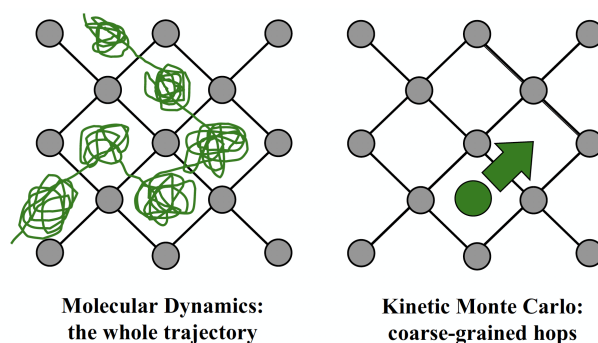


Figure 3.4: Reprinted from [127], Copyright (2009), with permission from John Wiley and Sons. "Schematic top view explaining the differences between a MD (left panel) and a kMC (right panel) trajectory. Sketched is the path covered by an adsorbate that diffuses over the surface by rare hops to nearest-neighbor sites. Whereas the MD trajectory resolves the short-time vibrational dynamics around the stable adsorption sites explicitly, this is coarse-grained into the rate constants in the kMC simulations so that the corresponding trajectory consists of a sequence of discrete hops from site to site."

For an introduction to kinetic Monte Carlo simulations see reference [126]

The Markov approximation is used where the evolution only depends on the state of the system at time t and not on the history of the system. The time evolution can be described using an equation of the form

$$\frac{dP_i(t)}{dt} = - \sum_{j \neq i} k_{ij} P_i(t) + \sum_{j \neq i} k_{ji} P_j(t) \quad (3.87)$$

The trajectories of the system consist of a sequence of jumps between the possible system configurations i.e. k_{ij} is the rate of going from state i to state j . Equation 3.87 determines the random selection of the next state to hop into and the variable timestep after which this occurs. This time is called the escape time Δt_j^{escape} where

$$\Delta t_j^{escape} = - \frac{\ln \rho}{k_{ij}} \quad (3.88)$$

$\rho \in (0, 1]$ is a random number. By looking at the trajectory over a long enough timescale and taking the average over all trajectories the set of all probabilities to be in a given state $P_i(t)$ can be found.

An intuitive way to solve this problem is calculate every possible Δt_j^{escape} when in a given state i , choose the one with the smallest timestep to hop into and then keep repeating this process. This is called the First reaction method.

The Bortz–Kalos–Lebowitz (BKL) algorithm is in many cases a more efficient way to solve such problems. In the BKL algorithm the total rate constant k_{tot} is found for all processes N

$$k_{tot} = \sum_{i=1}^N k_i \quad (3.89)$$

Then the executed process q is chosen with a random number ρ_1 such that

$$\sum_{i=1}^q k_i \geq \rho_1 k_{tot} \geq \sum_{i=1}^{q-1} k_i \quad (3.90)$$

The system time is then advanced by

$$\Delta t_{escape} = - \frac{\ln \rho_2}{k_{tot}} \quad (3.91)$$

now only 2 random numbers ρ_1 and ρ_2 need to be generated at each time step instead of N .

3.4.4 Multiscale modelling

Due to the vastly different length and time scales involved in studying a catalytic system theoretical simulations are often combined, sometimes hierarchically, in a multiscale modelling approach [128]. Figure 3.5 tries to give a rough representation of the different scales of investigation and to shed light on where different classes of methods belong. Beginning at the bottom end of the scale, quantum chemical calculations based on, for example, density functional theory (DFT) may be used at the active centre of the catalyst to predict the electronic structure. Advancing up the scale, it is suitable to model longer range effects such as diffusion with less computational demanding simulations such as, for example, MD simulations where the force field used is often empirical and based on classical mechanics. Towards the top of the scale computational fluid dynamics could be used to make full scale predictions about rates in a particular reactor. In a multiscale modelling approach the results from modelling on one length scale are used as input for simulations higher up the scale. For example, there is much interest in using electronic structure methods on atomic scale as inputs for a micro-kinetic model on the reactor scale [11, 129, 130].

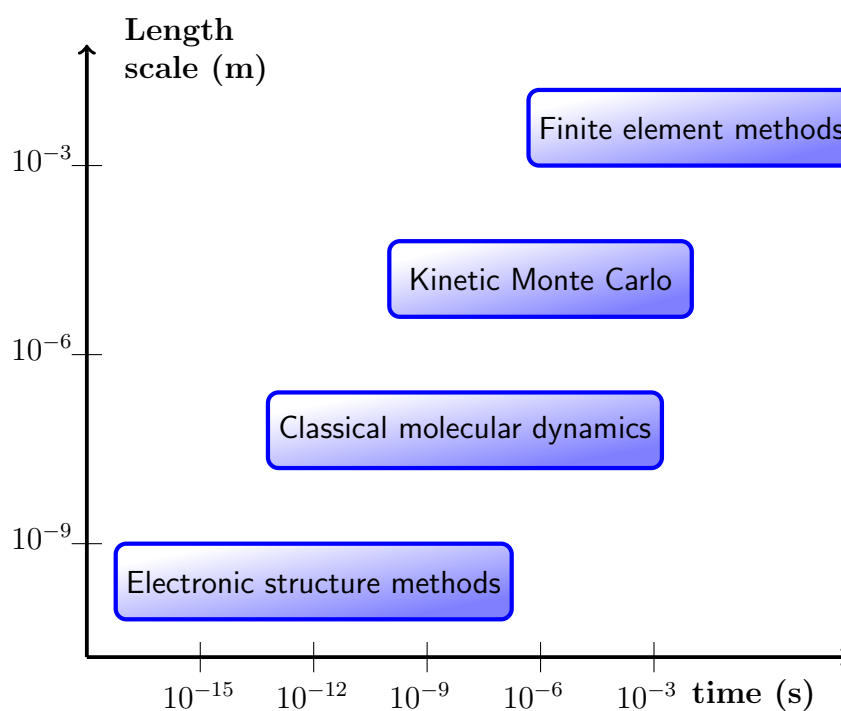


Figure 3.5: Schematic multiscale modelling diagram.

4 Modelling the formation of the first olefins in the MTO process

4.1 Introduction

The formation of the observed products in the MTO process can be explained through the HP mechanism, in which aromatics and olefins act cocatalysts to produce more hydrocarbons. In the olefin cycle, olefins are repeatedly methylated and then cracked into two olefins, making the HP autocatalytic in olefins. While this concept is widely accepted and explains experimental observations in the presence of hydrocarbons as cocatalysts, it remains unclear as to where these hydrocarbons initially come from. On the one hand, impurities in the feed and in the zeolite may initialise the HP [8, 38, 131]. There is also the possibility that hydrocarbons are formed directly from methanol. In this case, the formation of the first C-C bond has been identified as the crucial step, after which numerous facile paths to active HP species are conceivable.

A tremendous amount of experimental and theoretical research has been dedicated to study if and how direct C-C bond formation from methanol is viable [1, 4, 132–141]. On the experimental side, the use of *operando* spectroscopy has become increasingly important as it allows the identification of species under the actual operating conditions and during the initiation period [142, 143]. A challenge for the interpretation of the results is assigning species to either the initiation period or autocatalysis. On the theoretical side, quantum chemical calculations have been used to gain insight into the initiation mechanism at the atomic level. One of the challenges of quantum chemistry lies in the computation of accurate reaction free energies. Current modelling of zeolites is largely limited to DFT typically at the generalised gradient approximation level of theory. This leads to the usual underestimation of barrier heights that can be as high as 60 kJ/mol [130].

An equally important challenge lies in the interpretation of theoretically computed free energies and rate constants. The barriers for the initiation reactions seem prohibitively high [2] for a catalytic cycle. In terms of its kinetics, however, the MTO initiation does not resemble a catalytic steady-state problem and is coupled to the autocatalytic part of the olefin cycle [144, 145]. This means that the viability of an initiation mechanism can be indirectly measured through the extent to which it enables autocatalysis to start. Because of this interplay between initiation and autocatalysis, it is therefore difficult to assess the feasibility of a given initiation mechanism without explicitly modelling the reaction kinetics including autocatalysis.

This chapter is based on the following publication: P.N. Plessow, A.Smith, S.Tischer, and F.Studt, "Identification of the reaction sequence of the mto initiation mechanism using ab initio-based kinetics", J. Am. Chem. Soc, vol. 141, no.14, pp. 5908-5915, 2019.

4.2 Results and Discussion

The initiation kinetics of the MTO process were investigated using a batch reactor model which uses rate constants obtained from 42 reactions from the initiation stage and 63 from the olefins cycle (Figure A.1 shows the full reaction scheme and a list of all species and reactions is given in Tables A.1 and A.2. Also see 1.5 and reference [5]). All reaction were modelled in H-SSZ-13 zeolite and all elementary reactions of the reaction network were computed using a hierarchical cluster approach [130] which enables the calculation of accurate reaction barriers via higher level methods. The higher level method of choice here was second order Møller- Plesset perturbation theory (MP2) which has been shown to agree quantitatively with CCSD(T) for the chemistry considered here [130, 146]. Figure 4.1 gives a simplified overview of the investigated mechanism and includes the initiation and the autocatalytic olefin cycle as central parts.

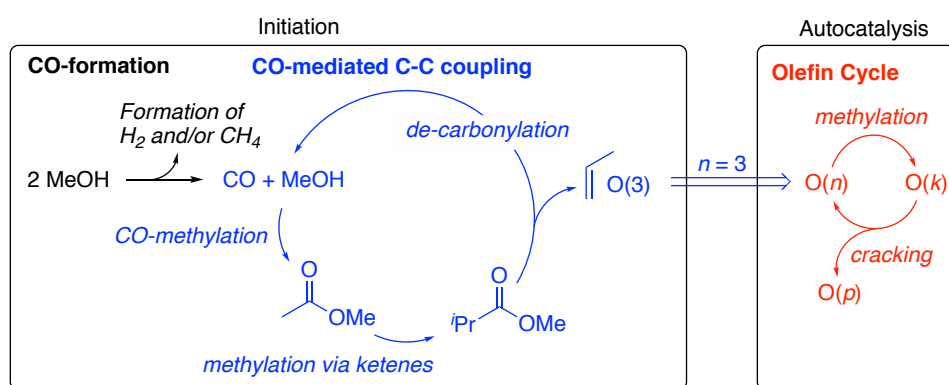


Figure 4.1: Overview of the initiation and autocatalytic part (olefin cycle only) of the MTO Process. The initiation part is further broken down into a part responsible for CO formation and CO-mediated C-C coupling. $O(n)$ is an abbreviation for any isomer of an olefin C_nH_{2n} .

The initiation has been divided into two regimes: 1) the dehydrogenation of MeOH to produce CO and 2) subsequent methylation of CO to form the first C-C bond yielding methyl acetate (MA) [147, 148]. It is worth noting that the carbonylation of methanol and DME has also been studied extensively [148–150] with these reactions possibly being connected to the direct conversion of syngas to hydrocarbons [151]. The decomposition of MA gives ketene and methanol and, through repeated methylation of ketene and methyl ketene, esters with multiple C-C bonds, such as methyl isobutyrate. This ester can be decarbonylated to yield free CO and propene. CO can then again be methylated and is therefore a catalytic species, but not an autocatalytic species. Propene can initiate the olefin cycle, in which the olefin is repeatedly methylated to higher olefins that are cracked into two olefins as described by the HP mechanism [5, 152–154]. In a recent study [5] the most favourable cracking mechanisms in H-SSZ-13 were found to occur for olefins larger than C7. Isobutene is the major cracking product mainly due to the fact that the corresponding cation (t-butyl cation) is particularly stable. Here, only on the olefin cycle part of the HP is focused on because, in the absence of impurities, no aromatic molecules are present initially. Therefore, the olefin cycle is expected to be the most relevant mechanism during and right after the initiation phase.

Simulations of the initiation reaction using a batch reactor model are shown in Figure 4.2. The kinetics are simulated at a constant temperature of 400 °C and an active site concentration of $17.9 \text{ mol}/m^3$. Diffusion limitations are not taken into account. The feed consists of an equilibrium mixture of DME, methanol, and water that results from an initial pressure of methanol of 1 bar. (The fast equilibration of 1 bar of methanol is shown in the Appendix Figure A.2). The partial pressures are shown in Figure 4.2 a) as a function of time.

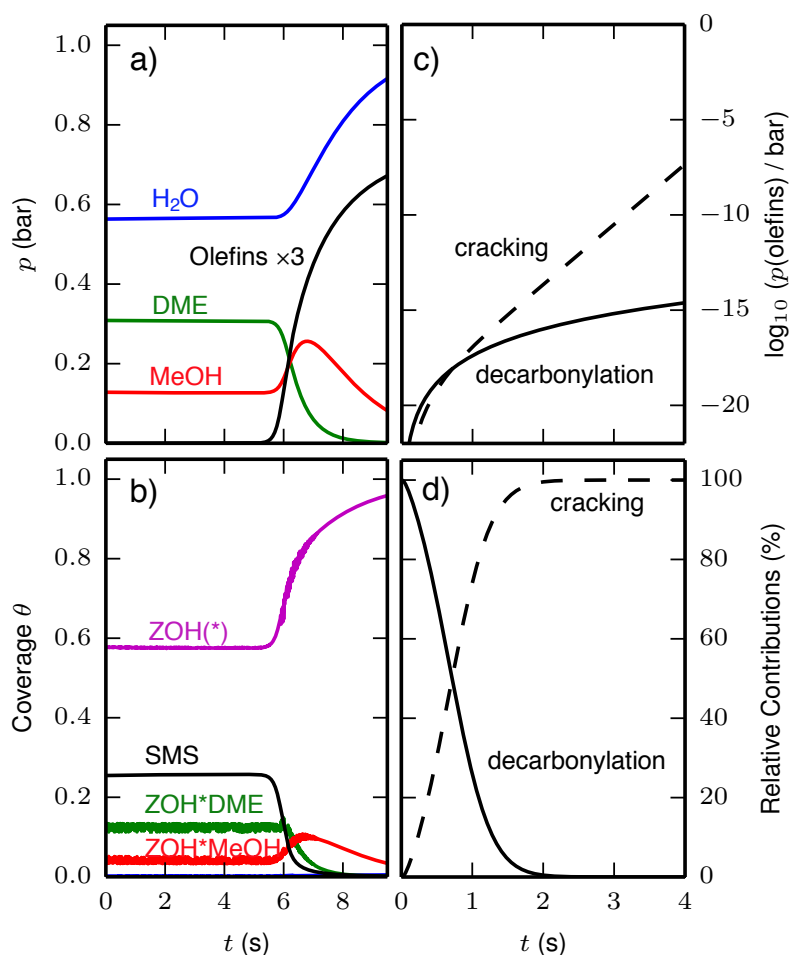


Figure 4.2: Results of the batch reactor model starting from an equilibrated MeOH/DME feed corresponding to an initial total pressure of MeOH of 1 bar as a function of time. a) Partial pressures of H_2O , DME, methanol, and olefins (MeOH and DME are also present in significant amounts as adsorbed species ZOH*MeOH and ZOH*DME). The sum of all olefin pressures is shown and is multiplied by a factor of 3 for better comparison. b) Coverages of SMS and adsorbed MeOH and DME. The formation of SMS from methanol is the reason that more H_2O than DME is formed initially. c) Partial pressure of olefins formed through decarbonylation and cracking. d) Relative contribution to olefin formation shown in panel c).

Note that the initial formation of SMS results in a water pressure that is higher than that of DME. The kinetic model reveals that there is an initiation phase without significant changes in partial pressures until a sudden light-off occurs, leading to the rapid formation of olefins and additional water. Figure 4.2 a) shows that the DME concentration decreases more rapidly at the light-off than that of methanol. This is due to the fact that olefin methylation using DME is faster compared to methanol, as has also been observed in experimental and theoretical studies [64]. Because methylation via DME produces methanol, there is a small initial increase in the methanol partial pressure before it eventually decreases. This feature has also been observed experimentally [7]. H_2 , CH_4 , formaldehyde, CO, MA, and all other intermediates considered here are present only in minor amounts throughout (less than 0.1 mbar) and are given in Figure A.3. Another class of intermediates that is being vividly discussed is ketenes [155] which are thought to play a role in the MTO and related processes but are inherently unstable. Figure A.3 also shows the partial pressures of ketene, methyl ketene, and dimethyl ketene as a function of time, indicating that they are formed but are present only in small amounts, thus highlighting the difficulty of detecting them experimentally.

Figure 4.2 b) shows the coverages of the catalyst as a function of reaction time. Most of the active sites are free (ZOH^*), followed by SMS and adsorbed DME and methanol. The coverages decrease with the corresponding gas phase concentrations. Figure 4.2 c) splits up the contributions of the decarbonylation (initiation) and cracking reactions (autocatalysis) to the formation of olefins before light-off, where no significant olefin concentration is observed (i.e., the sum of all olefin pressures is below 10^{-5} bar). Intrinsically, olefin formation through the autocatalytic cycle is orders of magnitude faster than the initiation reaction, which is also expressed through the differences in free energy barrier heights, where the highest barriers that have to be surpassed are about 50 kJ/mol lower for autocatalysis [2, 5]. It is important to understand that this means that olefin formation through the methylation of olefins followed by cracking becomes the dominating mechanism after a very short initiation phase and long before a light-off is observed (Figure 4.2 a)). This is also evident when the relative contributions of cracking and decarbonylation are analysed (Figure 4.2 d)). Importantly, the analysis clearly reveals that because of the large differences in rates between olefin formation from methanol and through autocatalysis, the total amount of olefins formed through the initiation reaction is negligible.

Now let's turn to the mechanistic details of the reaction sequence from methanol via MA to the first olefins. Figure 4.3 depicts the contribution of the various pathways calculated using the batch reactor model and the conditions described previously. Under these reaction conditions, the majority of the first oxidation steps occur via DME and mainly produces H_2 but also significant amounts of CH_4 . The second oxidation step mainly proceeds via methoxymethanol and to a lesser extent via dimethoxy methane, both producing methyl formate. Methyl formate is thus an important intermediate that is decomposed to CO, which is subsequently methylated to form MA via the intermediate formation of a surface ethanoate. The reaction of methanol with CO is thus responsible for the formation of the first C-C bond during the initiation phase of the MTO process catalysed by H-SSZ-13. MA is a precursor for olefins that can be formed via decomposition of the surface ethanoate to ketene, which is then further methylated to form a surface propionate. The surface propionate can be decarbonylated to form CO and ethene. CO is thus recovered and can again be methylated. Instead of ethene formation, the surface propionate can, analogously to the surface ethanoate, decompose to methyl ketene, the methylation of which gives a surface isobutyrate. The surface isobutyrate can be decarbonylated to CO and propene. Alternatively, the surface isobutyrate can decompose to dimethyl ketene which can be methylated to form a surface pivalate that can be decarbonylated to form isobutene and CO. Overall the kinetic analysis reveals that propene and, to a lesser extent, isobutene are the main products in this initiation phase. Other pathways that have been included explicitly are variants of the often-discussed methane-formaldehyde mechanism. As expected on the basis of their higher barriers, their contribution to any olefin formation during and after the initiation phase is negligible (see the Figure A.1).

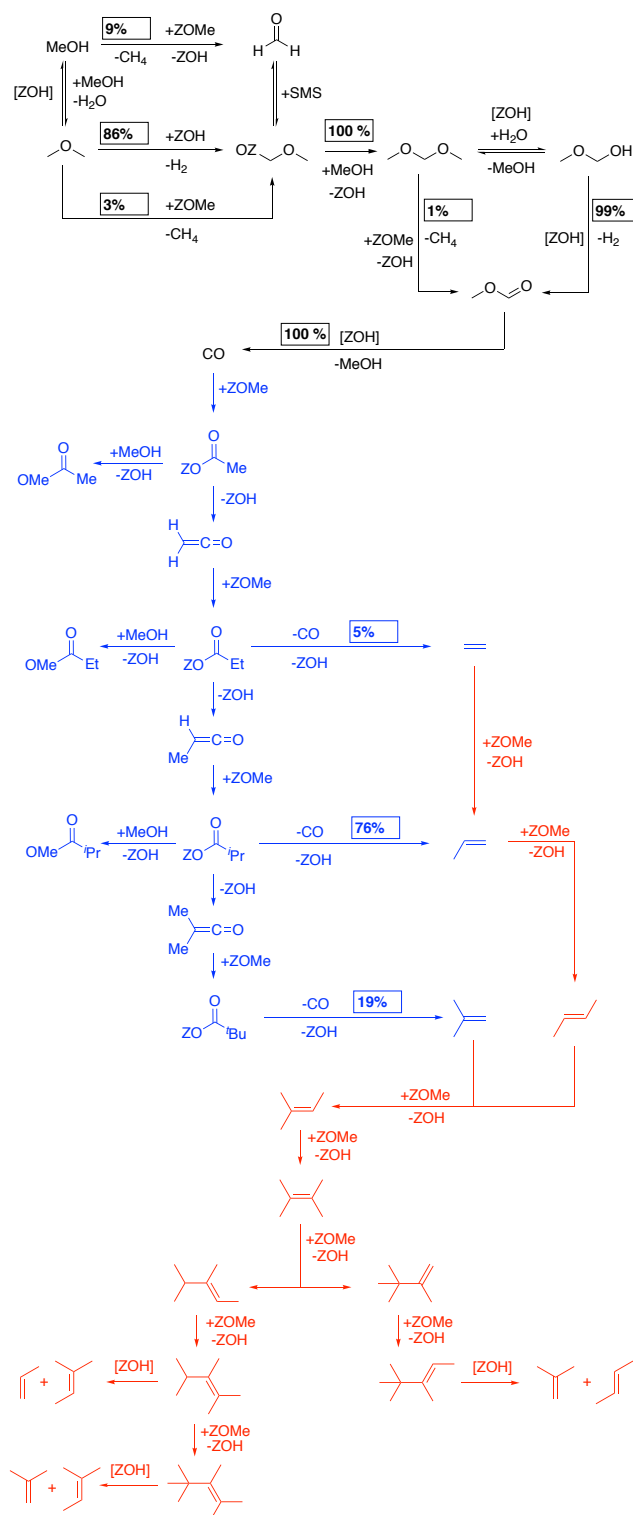


Figure 4.3: Contributions of the various reaction paths of the initiation phase. The percentage of the total flux was analysed at $t = 0.3$ s. Only pathways contributing more than 1% to the total rate are shown. The most important pathways for the olefin cycle are depicted. For a given olefin carbon framework, only the most stable isomer is shown (for example, 1-butene vs 2-butene). The corresponding isomerisations are omitted. All pathways studied are given in Figure A.1.

Next let's turn to analysing how sensitive the formation of the first olefins is to each reaction step. To do this a sensitivity analysis was performed in which the barriers were varied by small amounts to see how much they affect the total olefin pressure. More specifically, the derivatives of the sum of all olefin partial pressures $p_{\text{olefins}}(t)$ with respect to a given TS free energy were calculated.


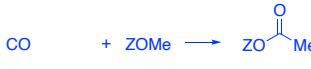
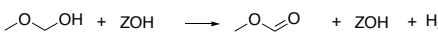
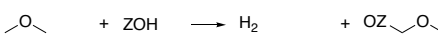

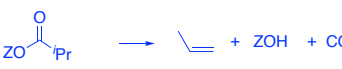




$$s_i^n(t) = \frac{|s_i(t)|}{\sum |s_j(t)|} \text{ with } s_i(t) = \left(\frac{\partial p_{\text{olefins}}(t)}{\partial G_i^\ddagger} \right)_{G_{j \neq i}^\ddagger} \quad (4.1)$$

Table 4.1 shows the results of the sensitivity analysis for a point well within the initiation phase (0.3 s) as well as after that phase but before light-off (3 s) (See also Figure A.4 for the key sensitivities plotted against time). Only the normalised sensitivities $s_i^n(t)$ which give the percentage of the sum of the absolute values of all sensitivities (see Table A.3 for a list of all sensitivities) that a certain barrier has are discussed. For the reactions shown $s_i(t)$ is always negative, which means that a higher barrier decreases the amount of formed olefins, while $s_i^n(t)$ is defined to be positive. Along with the most important reactions from the initiation phase the most important part of the modelled reactions of the olefin cycle are also depicted. The olefins formed from the initiation period (ethene, propene, and isobutene) can be further methylated to form branched heavier olefins (C8,C9) that can then be cracked to smaller olefins (C3-C5). The cracking products of the depicted reactions (propene, butene, isobutene, and methyl butene) can all re-enter the olefin cycle and can then be cracked again. Each olefin, upon cracking, generates two olefins and is therefore an autocatalytic species.

After the initiation phase, the limiting reactions are methylations in the olefin cycle. This may seem trivial, but it is important to stress that it means that observable olefin formation mainly depends on the barriers of autocatalytic reactions rather than those of initial C-C bond formation reactions. It also means that the question of whether a given initiation mechanism is sensible in terms of the total observed rate cannot be answered without also knowing and modelling the autocatalytic olefin cycle. In terms of the reactions that control initiation, the sensitivity analysis at 0.3 s shows that both reactions for methanol dehydrogenation and for CO-mediated C-C coupling are important (see Table 4.1). At first glimpse, this may be surprising because the barriers for dehydrogenation are significantly higher than for all reactions after CO formation. This can be rationalised by the fact that CO is catalytic in forming olefins, while methanol dehydrogenation generates catalytic CO. Therefore, both faster CO formation and faster CO utilisation independently lead to faster initiation, and both are rate-limiting during the initiation phase.

Overall the analysis shows that the TSs that are found to be most important for the olefin formation rate are generally those with the highest barriers within a given class of reactions. For CO-mediated C-C coupling, these are the methylation of ketene, methyl ketene, CO, and dimethyl ketene as well as the decarbonylation of the surface isobutyrate. For CO formation, they are the dehydrogenation of DME and methoxymethanol dehydrogenation. For the autocatalytic olefin cycle, the methylation of light olefins is rate-limiting.

Table 4.1: Normalised sensitivities s of the total olefin pressure in percentage at a given time for the most important reactions. The colour code is chosen according to Figure 4.3 where blue shows CO-mediated C-C coupling, black shows methanol dehydrogenation reactions, and red shows parts of the olefin cycle. The first time (0.3s) lies within the initiation zone, while the second time (3.0 s) is after autocatalysis dominates but still before the visible light-off of the reaction (see also Figure 4.2). Additionally, activation free energies ΔG^\ddagger are given for each reaction in kJ/mol.

Elementary reaction	$t =$	
	ΔG^\ddagger	$s_i^n(t)$
	159	15.7 3.4
	190	15.7 3.4
	181	15.5 3.4
	220	15.1 3.3
	139	15.0 3.4
	130	9.7 0.9
	136	4.3 2.0
	147	2.0 36.4
	154	0.7 32.8
	132	0.4 4.5

4.3 Methods

All rate constants were extracted from previously computed data [2, 5] which employed periodic PBE-D3 calculations carried out with the VASP using standard PAWs which were then corrected by MP2/def2-TZVPP calculations carried out with Turbomole [156] using T46-cluster models [130]. The rate constants were calculated using harmonic TST at 400 °C. The free energies are given for a total reference concentration of the active sites of $17.9 \frac{\text{mol}}{\text{m}^3}$ and a reference pressure of 1bar. Diffusion limitations are neglected, for example, perfect mixing is assumed.

The solution of the kinetics is non-trivial because numerical inaccuracies can initiate autocatalysis much like impurities in experiment. Therefore, care must be taken whenever iterative solutions are involved. Again, as in the experiment, it is *a priori* not clear when impurities are negligible, and it is therefore difficult to determine sufficiently accurate thresholds for iterative solutions. To cope with these problems a simple Euler integration was employed which avoids the use of iterative methods. The first 1000 to 10 000 steps were performed with a minimum time step of 10^{-10} s and afterward with a minimum time step of $5 \cdot 10^{-10}$ s. Additionally, time steps are limited so that any individual partial pressures decrease at most by 5%. For computational efficiency some rate constants for reactions with particularly low barriers were artificially increased to 80 kJ/mol. Figure A.5 shows that this leads to a negligible difference in the obtained pressures of propene. The simulations, which typically cover a simulation time of a few seconds, require on the order of 10^8 to 10^8 steps and run for up to a few hours. While this is certainly a “brute-force” approach to solving these kinetics, it allows rigorous error-control through lowering the time steps and avoids spurious contamination with autocatalytic, numerical inaccuracies that can occur, when iterative methods are used. The sensitivity analysis employs the numerical first derivative from central finite differences, where TS free energies are perturbed by ± 1 kJ/mol.

4.4 Conclusion

A simulation of the batch reactor kinetics of the initial phase of the MTO process was presented. Highly accurate MP2-corrected rate constants for a total of 105 elementary reaction steps comprising both the initial path to C-C formation and a representative part of the olefin cycle were used. Although these rate constants were found in H-SSZ-13 zeolite, similar conclusions for other zeotypes can be expected as a result of similarities in the relative ordering of the barriers [157]. The results show that the MTO process can be initiated in the absence of impurities via methanol dehydrogenation to CO and subsequent CO- methylation, ketene methylation, and decarbonylation of the formed esters. Importantly, the results also demonstrate the need to move beyond microkinetic modelling or the intuitive interpretation of barrier heights for an in depth understanding of the initiation mechanism. The crossover of rates for olefin formation from initiation and autocatalysis occurs long before large amounts of olefins are formed at quantities that can be difficult to detect experimentally. This has important consequences for the interpretation of experiments related to the initiation reaction because it shows how difficult it is to determine where the initiation zone ends and which species constitute a central part of it. While the results presented are able to disentangle the reaction mechanism in the initiation phase, later stages also include aromatic formation and olefin production via the aromatic cycle [158]. These need to be included in future studies that go beyond the question of MTO initiation in order to obtain a full picture of the entire MTO process and explain the observed product distribution. Importantly, this also calls for the inclusion of diffusion effects and might ultimately allow direct simulation of phenomena such as catalyst deactivation through coking.

5 Diffusion limitations in H-SSZ-13 zeolite

5.1 Introduction

During the MTO process, large, sometimes branched hydrocarbons and olefins but also aromatics are formed or converted within the zeolite cavities which are interconnected through pores that are typically in the one nanometer range. As a consequence, a zeolites specific activity, selectivity and stability is greatly influenced by the diffusivity of molecules through these pores [7, 26, 27, 159]. Addressing the diffusion limitations of molecules within zeolites has thus already been subject to extensive experimental [160–164] and theoretical study [165–172]. Much of the current theoretical literature on diffusion limitations tends to focus on smaller molecules such as for example propene and often uses higher molecular loadings. More often than not MD simulations are employed and it is typically found that passing through the pores of the zeolite is an activated process resulting in a linear relationship between mean squared distance and time [165, 171].

The aim of this chapter is to investigate larger molecules for example benzene and to establish the molecular size at which diffusion becomes prohibitive. DFT calculations are employed to compute the TSs for molecules to pass through the pores of H-SSZ-13 zeolite. The chosen molecule set consists of key olefins and aromatics from the MTO process. A simple lattice hop model will be employed to find the rough order of magnitude of the diffusion constants. Diffusion constants obtained in this manner could eventually be incorporated into a more complex kinetic model, for example, they could reasonably straightforwardly be used to try and simulate the flow in a plug flow reactor. Eventually knowledge of the diffusion constants could perhaps be used to make predictions about which intermediates are likely to be involved in coke formation and perhaps even to try to reproduce the observed product distributions from experiments and the industrial scale.

This chapter is based on the following publication: A.T.Smith, P.N.Plessow, and F.Studt, "Density functional theory calculations of diffusion barriers of organic molecules through the 8-ring of h-ssz-13", Chem. Phys, vol. 541, p. 111033, 2021.

5.2 Results and Discussion

H-SSZ-13 is modelled using a unit cell with one Al site, with the proton located so that it is most accessible to the channel, as has been described in earlier studies [2, 157]. The cavities of this framework are connected by 8-membered rings with a geometrical diameter of 7.4 Å with respect to the position of the Si nuclei and 6.5 Å with respect to the position of the O nuclei. The 8-membered ring and the acid site are depicted in Figure 5.1. The effective diameter experienced by diffusing molecules is smaller than the geometric diameter due to repulsion between the electron shells of the ring and the molecule. Thus, the effective vdW diameter of the ring is roughly 3.7 Å.

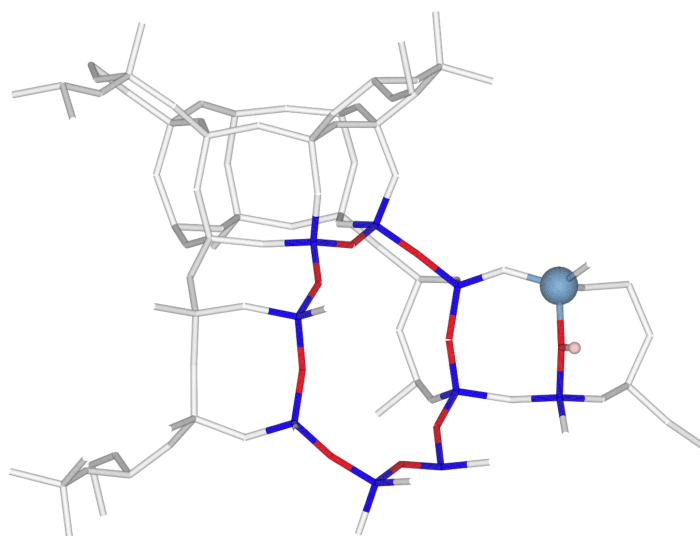


Figure 5.1: The structure of H-SSZ-13. The 8-membered ring and the acid site are highlighted. Silicon atoms are highlighted in blue, oxygen in red, hydrogen in pink and aluminium in light blue.

The goal here is to model diffusion of organic molecules in the limit of a low concentration of adsorbates. The diffusion behaviour at higher concentration may differ [172]. Co-adsorption of additional molecules is excluded and the limit of a low acid site density is assumed. For diffusion through the eight-membered ring, only pure siliceous rings, consisting only of SiO_2 units are considered. This is a structural motif that can be expected to occur frequently. A single acid site is placed within the unit cell at a position where it does not directly interfere with diffusion. The goal of including this acid site is to take into account the stabilisation of adsorbates in the initial and final states before and after diffusion. This is generally expected to increase the diffusion barriers with respect to these initial and final states. It should be noted that acid sites located within the 8-membered ring may also interact with the guest molecule during diffusion. In agreement with a recent study [172] including an acid site in the 8-membered ring led to a stabilisation of the TS (see Appendix Section B.1). Since purely siliceous rings are therefore expected to lead to a higher barrier, this situation is used for this trend study.

For adsorption at the acid site vdW complexes, π -complexes and alkoxides are considered as the adsorption states (See Figure 1.11). To differentiate between vdW complexes and π -complexes, a simple geometric criterion was used where complexes with a C-H distance smaller than 2.4 Å are considered π -complexes. Plain adsorption and desorption of molecules occurs typically without energetic barrier and is simply uphill or downhill in energy. This is illustrated in Figure 5.2 for the case of isobutene, where dissociation from the acid site is uphill in energy but does not require a significant barrier (also see Appendix Section B.2). In contrast Figure 5.2 also shows that there is a high barrier for diffusion through the 8-membered ring.

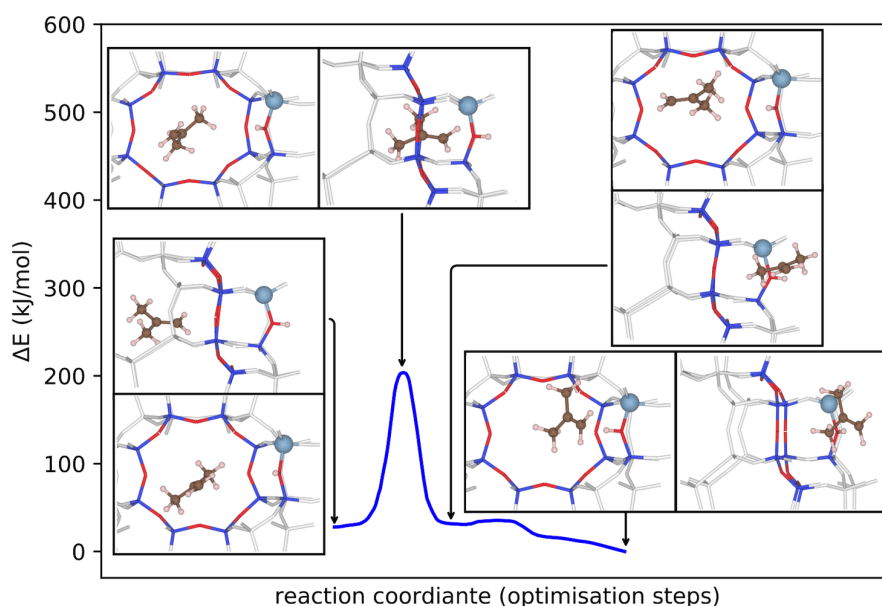


Figure 5.2: Energy profile for the diffusion of isobutene through the 8-membered ring. Insets illustrate the atomic structure at the indicated points of the reaction path with views both along and parallel to the ring. The energy profile was obtained by distortion of the TS along the transition mode followed by structural optimisation towards the initial and final states. Additional rearrangements of the final state that occur with low barriers were obtained with NEB calculations.

The molecules investigated were chosen to have incrementally increasing vdW diameters (d_{vdW}) with the d_{vdW} defined as the smallest cross-section that a molecule can fit inside plus an additional 2.4 Å corresponding to twice the vdW radius of hydrogen [173] which accounts for steric repulsion (see Figure 5.3 and Figure 5.4). The minima are referenced to the most stable adsorption geometry which depending on the molecule can be a π -complex, an alkoxide or a vdW complex (see Table 5.1 and also Table B.3) with the obtained adsorption energies being in good agreement with values from the literature [5, 62]. When the TS is given relative to the most stable state of the corresponding molecule it thus represents the diffusion barrier during a reaction.

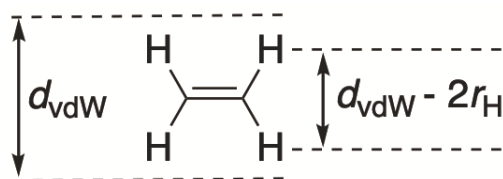


Figure 5.3: Definition of d_{vdW} .

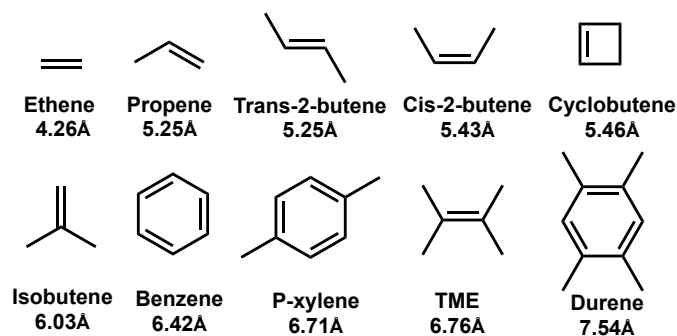


Figure 5.4: The d_{vdW} of ten selected molecules.

Table 5.1: Calculated adsorption energies and diffusion barriers for the 12 molecules investigated. The adsorption energies included are for the most stable adsorption configuration on the acid site of H-SSZ-13. The diffusion barriers are relative to this most stable adsorption configuration. All energies are given in kJ/mol.

Molecule	Most stable adsorbate	Adsorption energy	Diffusion barrier
Ethene	Alkoxide	-95.1	76.4
Propene	Alkoxide	-90.5	79.2
Trans-2-butene	Alkoxide	-93.0	68.9
Cyclobutene	Alkoxide	-92.2	133.1
Cis-2-butene	π -complex	-82.3	80.4
Isobutene	π -complex	-93.3	208.4
Isobutane	vdW complex	-78.8	201.0
Methanol	Hydrogen bonded	-115.3	81.5
Benzene	π -complex	-86.2	248.1
Para-Xylene	vdW complex	-96.0	226.8
Tetramethylethylene	π -complex	-88.1	244.0
Durene	vdW complex	-127.1	348.5

The formation of alkoxides was considered, since these are also known to be stable states of olefins in zeolites. On the other hand, MD studies indicate that π -complexes are favoured over alkoxides due to entropic effects even at room temperature [62]. In contrast to plain adsorption and desorption, the formation of alkoxides requires a distinct chemical reaction, where an O-H bond of the zeolite framework is broken and a C-H bond and a C-O bond with the olefin is formed instead. This barrier for alkoxide formation and vice versa is on the order of 120 kJ/mol for ethene and propene (see Appendix Section B.3) and therefore much higher than the diffusion barrier.

Overall, these barriers are unlikely to be a limiting factor for diffusion for two reasons. First of all, a free olefin could overcome the lower diffusion barrier many times before being trapped again as an alkoxide, which is associated with a much higher barrier. Most importantly, however, in terms of free energies, alkoxides are unlikely to be the most stable species at elevated temperatures relevant for catalysis. Therefore, alkoxide formation barriers are not considered here. Nevertheless, for consistency, the diffusion barriers are referenced to alkoxides, where those are the most stable states. The energetic difference in stability with respect to π -complexes is at most 20 kJ/mol and alkoxides are only most stable for ethene, propene and cyclobutene, which have relatively low diffusion barriers so that referencing these diffusion barriers either to alkoxides or π -complexes does not make a large difference.

The diffusion barriers investigated exhibit three different diffusion patterns (see Figure 5.5), with the shape of the energy profile and the occurrence of intermediates heavily depending upon the molecular geometry of the diffusing molecule. Isobutene exhibits one clearly distinct TS. The diffusion of tetramethylethylene (TME) on the other hand is characterized by two symmetric TSs separated by a minimum. This can be attributed to the effective symmetry of TME. For durene, three barriers which are separated by two minima were found, again due to the symmetry of the diffusing molecule. Importantly, the TS with the maximum barrier was identified in all cases. This barrier is taken as the overall diffusion barrier. Interestingly, the diffusion patterns of larger molecules are accompanied by distortions of the pore structures, albeit mostly small. For durene, for example, the ring distorts slightly with the diameter increasing by 0.73 Å.

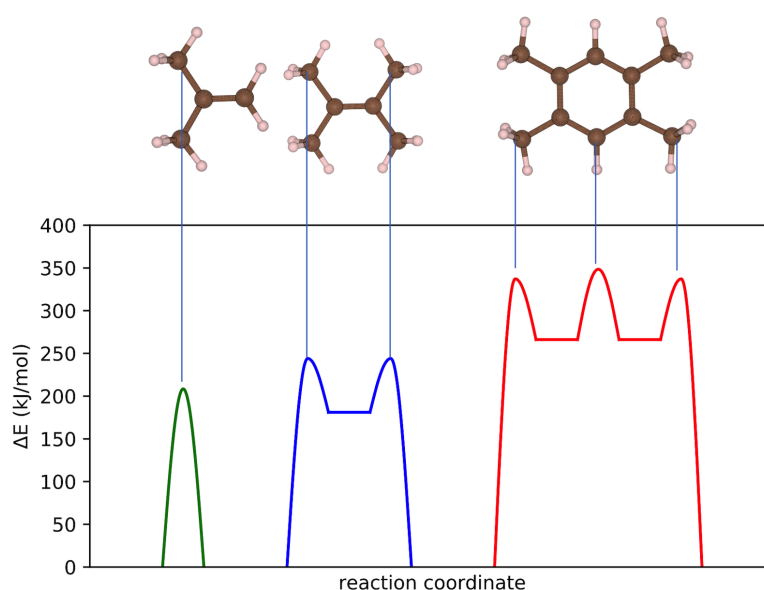


Figure 5.5: Schematic potential energy profile based on TSs and intermediates, for isobutene (left), tetramethylethylene (middle) and durene (right) to traverse through the 8-ring in H-SSZ-13. The adsorbed molecule at the acid site is chosen as the reference state (see also Table 5.1).

All calculated diffusion barriers are shown as a function of the d_{vdW} in Figure 5.6, both with respect to the molecules in the gas-phase (left) and the most stable adsorption configuration (right). Adsorption energies for olefins and aromatics at the acid site of H-SSZ-13 are in the range 80 – 140 kJ/mol, with the increase in vdW interactions of larger molecules being compensated by an increase in repulsion (see Section B.5 in the Appendix). The interaction of smaller olefins (ethene, propene, cis-2-butene and trans-2-butene, all with a d_{vdW} of less than 5.3 Å) with the pore is negligible, thus resulting in a constant value of around -20 kJ/mol relative to the gas-phase (Figure 5.6a) (or 60-80 kJ/mol when referenced to the most stable adsorption state, Figure 5.6b). These molecules will hence have relatively large diffusion constants.

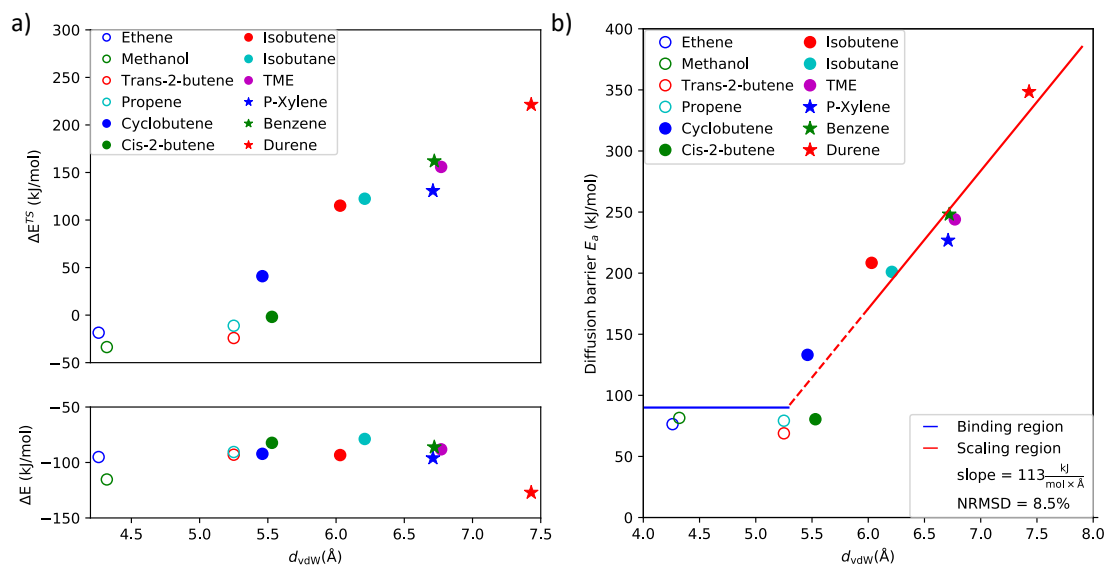


Figure 5.6: (a) Adsorption energies and diffusion barriers relative to the molecules in the gas-phase are shown as a function of vdW-diameter. The lower graph shows adsorption energies, the upper graph shows TS energies. (b) Diffusion barriers as a function of vdW-diameter. The straight blue line indicates a binding region with no significant diffusion barriers. Open markers indicate molecules with a d_{vdW} below 5.3 Å. The red line indicates the scaling region with linearly increasing diffusion barriers. Filled markers indicate molecules with d_{vdW} above 5.3 Å. Circles indicate olefins and stars indicate aromatics. The red line is a linear fit with a normalised root mean squared deviation (NRMSD) of 8.5%.

Olefins with d_{vdW} above 5.3 Å, on the other hand, experience strong repulsive interactions with the pore through which diffusion takes place, resulting in large diffusion barriers that increase linearly with the d_{vdW} . Isobutene ($d_{vdW} = 6.03$ Å) for example, has a diffusion barrier of 208 kJ/mol when referenced to the most stable adsorption state. The diffusion of isobutene through the pores of H-SSZ-13 will hence be extremely slow. Diffusion of TME and benzene have even higher barriers of 244 and 248 kJ/mol, respectively. The molecule with the largest d_{vdW} (7.54 Å), durene has a diffusion barrier of 348 kJ/mol relative to the adsorbed state. For molecules with sizes from 5.46 Å (cyclobutene) up to a d_{vdW} of 7.54 Å (durene) there is a roughly linear correlation between the magnitude of the diffusion barrier and d_{vdW} . The barriers above 5.3 Å were fitted to the function $a \cdot d_{vdW} + b$ yielding a slope of 113 kJ/(mol·Å) with a normalised root mean squared deviation (NRMSD) of 8.5%. Importantly, this correlation depends only on d_{vdW} . While the obtained NRMSD is encouraging, unfortunately, there is no clear correlation with d_{vdW} for d_{vdW} less than 6 Å for example when comparing the diffusion barriers of cyclobutene and cis-2-butene. It is also important to note that for these small molecules, barriers are largely due to strong adsorption at the acid site rather than due to the barrier measured relative to the gas phase.

Next diffusion constants are estimated from a lattice hop model using equation 5.1.

$$D = \frac{l^2 k_B T}{h} e^{\frac{-E_a}{k_B T}} \quad (5.1)$$

Where l is the lattice parameter, k_B is the Boltzmann constant, h is the Planck constant, T is the temperature and E_a is the diffusion barrier. A temperature of 673.15 K is assumed as this is a typical temperature for the MTO process. The entropic contributions from the initial and TSs are also assumed to be similar as the diffusing molecules have nearly identical vibrational frequencies. A value of 13.6 Å was used for the lattice parameter. Using these approximations and $E_a = 76.4$ kJ/mol for ethene a value for the diffusion constant of $3.6 \cdot 10^{-11} \frac{m^2}{s}$ was obtained. The value is in good agreement with other theoretical studies reported in the literature (e.g. $3.8 \cdot 10^{-10} \frac{m^2}{s}$ for ethene in SSZ-13) [165]. Benzene, the simplest aromatic molecule has a diffusion barrier of 248.1 kJ/mol and a diffusion constant of $1.4 \cdot 10^{-24} \frac{m^2}{s}$ is obtained indicating benzene is clearly diffusion limited.

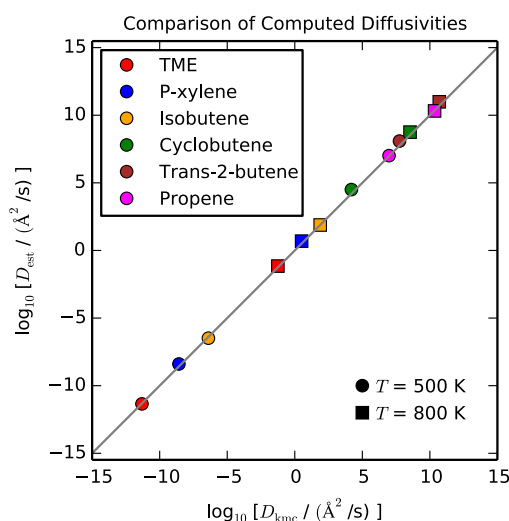


Figure 5.7: Comparison of diffusion constants obtained using the rate-determining step approximation as expressed in equation 5.1 with results from kMC simulations. For propene and isobutene, equation 5.1 is exact since only one minimum and TS is included in the kMC simulation.

For the estimation of diffusion constants only the highest barrier relative to the most stable minimum is considered. This approximation is analogous to the rate-determining step approximation that is often applied in catalysis. As can be seen from Figure 5.7, for the range of molecules considered this approximation works remarkably well, when the diffusion constants obtained with equation 5.1 are compared with diffusion constants extracted from kMC simulations. The accuracy of the diffusion constants obtained is generally sufficient to estimate the order of magnitude of the diffusivity.

The accuracy of the diffusion constants computed in this work is mainly limited by the energies obtained with DFT and the treatment of entropic contributions. The main goal of this work was to determine up to which point molecules are mobile in H-SSZ-13 with the approach used here likely being sufficient for that purpose. Most computational investigations as well as experimental studies focus on the diffusion of molecules with relatively high diffusion constants. It should be stressed that it is not the intention here to compute diffusion constants with high accuracy but instead determine the limit where diffusion is extremely slow with the guest molecule likely being immobile within the zeolite at typical reactions conditions. This study is thus complementary to existing investigations, that focus on diffusion constants of more mobile molecules and compute them with high accuracy using MD-simulations often accounting for additional effects such as coadsorbates, varying acid site locations and lattice dynamics [171, 174–176].

5.3 Methods

Periodic DFT calculations were carried out with the PAW method using the VASP program package in version 5.3.3.4 using the standard VASP-PAWs and the Atomistic simulation environment [177]. The PBE functional with Grimme’s dispersion corrections (PBE-D3) was used in all calculations. The energy cut off was 400 eV and the Brillouin-zone was sampled at the Γ -point with Gaussian-smearing with a width of 0.1 eV. The lengths of the vectors of the unit cell were 13.625, 13.625, and 15.067 Å as optimised in earlier studies [2] employing H-SSZ-13.

The dimer method, CI-NEB and constrained optimisations were employed to obtain TSs. In the NEBs, Image Dependent Pair Potential interpolations [178] or linear interpolations were employed. The PBE-D3 functional was tested against the BEEF-vdW functional that has been shown to capture the interaction of hydrocarbons with zeolites quite accurately [179] using single point calculations of the optimised structures and the same parameters as described above. Figure B.6 shows that BEEF-vdW and PBE-D3 give similar results which lends confidence to the results obtained here. Zero damping was used for the dispersion correction. The use of different damping functions was also explored (see Section B.7) with no systematic trend found when comparing damping functions. In order to test whether lateral interactions play a significant role, the minima and the intermediate preceding the TS for a 2 by 2 super cell for the case of benzene were calculated. Section B.8 shows that the interactions are very minor such that the values for the TS are unlikely to be affected by lateral interactions and the size of the super cell.

Harmonic force constants were computed from a central finite difference method where only atoms in the adsorbed molecule were included. All TSs were verified to contain only a single imaginary harmonic frequency corresponding to the transition vector of the reaction. In addition, through small distortions away from the TS followed by an optimisation, a given TSs connectivity with the minima and other TSs was verified. Tests were done to see whether including the atoms of the zeolite ring in the vibrational analysis influences the results and this was found not to be the case. Finally, the TSs for the molecule to traverse the ring in both directions were found. The good agreement is provides extra confidence in the obtained barriers.

Diffusion constants were computed using equation 5.1 and the rate obtained was compared to kMC simulations. In the kMC simulations, all elementary steps were considered and the diffusion constant was computed by analysing the mean squared displacement obtained for 100 separate simulations with 10^5 steps each.

5.4 Conclusion

The diffusion of organic molecules through the 8-membered rings of H-SSZ-13 was investigated using DFT calculations. Both diffusion barriers relative to the gas phase as well as relative to the diffusing molecule being adsorbed on an acid site were considered. When taken relative to the adsorbed state, the diffusion barriers found are in the range of 60-80 kJ/mol for smaller molecules. For larger olefins and aromatics the diffusion barriers reaches 200 kJ/mol for isobutene and 350 kJ/mol for durene. Furthermore, for the larger molecules, a simple scaling relation between the diffusion barrier and the size of the largest cross section of the molecules was found. This simple model enables the estimation of diffusion barriers in the limit of large molecules. For small molecules ($< 5.5 \text{ \AA}$), which have relatively low diffusion barriers the strength of adsorption is the most important factor in determining the height of the barrier. The established correlation is intended to give an estimate of diffusion barriers in the range where diffusion is slow to impossible, in order to predict whether or not a molecule can reasonably diffuse through zeolite. While the model has been shown to work for the chabazite framework, future work will focus on extending this to other zeolite topologies.

6 Trends in reactivity due to proximate acid sites in H-SSZ-13

6.1 Introduction

In this chapter DFT calculations are used to investigate how reactions in H-SSZ-13 zeolite are affected by the influence of a second aluminium substitution per unit cell. The second BAS is placed at varying neighbour distances and the observed changes in reactivity are correlated with measures of acidity at the first BAS. H-SSZ-13 is an excellent choice of catalyst for this study because it has only one crystallographically distinct position for the first aluminium substitution. Although all T-sites in H-SSZ-13 are symmetry equivalent there are still many different ways for two or more Al atoms to sit inside the unit cell. This means H-SSZ-13 is a rather well-defined catalyst for high Si/Al ratios where there is a small likelihood of more than one aluminium per unit cell and a poorly defined catalyst for lower Si/Al ratios. DME synthesis from methanol is studied as this reaction has been investigated in great detail both experimentally [180, 181] and theoretically [63, 180–184].

On the atomic scale the strength of the BAS as well as the interaction of the reactant with the surrounding framework are both critical in determining the activity at a given BAS. However, zeolite crystals in a working catalyst typically have a wide variety of compositions and sizes and may be around a μm in diameter. Thus, the gross cumulative activity of zeolites is complicated by the fact that there are many different T-sites where the Al atoms can be substituted all with different BAS strengths. Experimentally rates for DME-formation have shown to correlate with the number of proximate Al pairs in H-SSZ-13 [46]. This could potentially mean that zeolite synthesis techniques can be developed which steer the synthesis towards more active motifs. While recent advances in synthesis and characterisation of zeolites are able to control the proximity of aluminium atoms to a larger extent [46, 185], it is still difficult to address how this affects the intrinsic activity experimentally [185]. On the theoretical side specific reactions can be explicitly modelled using a wide variety of combinations of aluminium sitting. Activation barriers in H-ZSM-5 for direct DME-formation have already been shown to vary by up to 40 kJ/mol, depending on the location of the acid site [18]. Furthermore, in an investigation of ethanol and methanol dehydration in H-SSZ-13 with varying densities of Al atoms, variations of activation barriers on the order of 20 kJ/mol were observed for proximate Al pairs [45].

This chapter is based on the following publication: A.T.Smith, P.N.Plessow, and F.Studt, Trends in the Reactivity of proximate Aluminum Sites in H-SSZ-13. *J. Phys. Chem. C*, *Accepted* 2021.

6.2 Results and discussion

The separation of a pair of two Al atoms is illustrated in Figure 6.1 a). The nomenclature P_n is used to refer to a structure, in which the two closest Al atoms are n th nearest neighbours. Alternatively, one can say that the two Al atoms are separated by $n-1$ (Si-O)-units. With one aluminium substitution per unit cell (Si/Al ratio of 35), two Al atoms (in two adjacent unit cells) are separated by five (Si-O) units. This P6 structure with one Al per unit cell is used as the “large separation limit” and the stability and reactivity of closer Al pairs is referenced relative to this limit.

There are 35 different ways to add a second Al atom in the 36T unit cell given the first one has been fixed with all these substitutions being symmetry inequivalent. 10 such examples with two acid sites per unit cell (nominal Si/Al ratio of 17) are illustrated in Figure 6.1 b). The structures are labelled according to the closest Al pair where the closest Al atom is not necessarily in the same unit cell, but can also be in a periodic image of the unit cell. Taking this into account, the most distant Al pair achievable with two Al atoms per unit cell is P5, a fifth-nearest neighbour substitution. Overall, there are 4 P1 isomers, 9 P2 isomers, 12 P3 isomers, 8 P4 isomers and 2 P5 isomers. 6.1 c) shows the oxygen labelling used in this work (for a comparison to the oxygen labels used in [45] see Table C.1 in the Appendix).

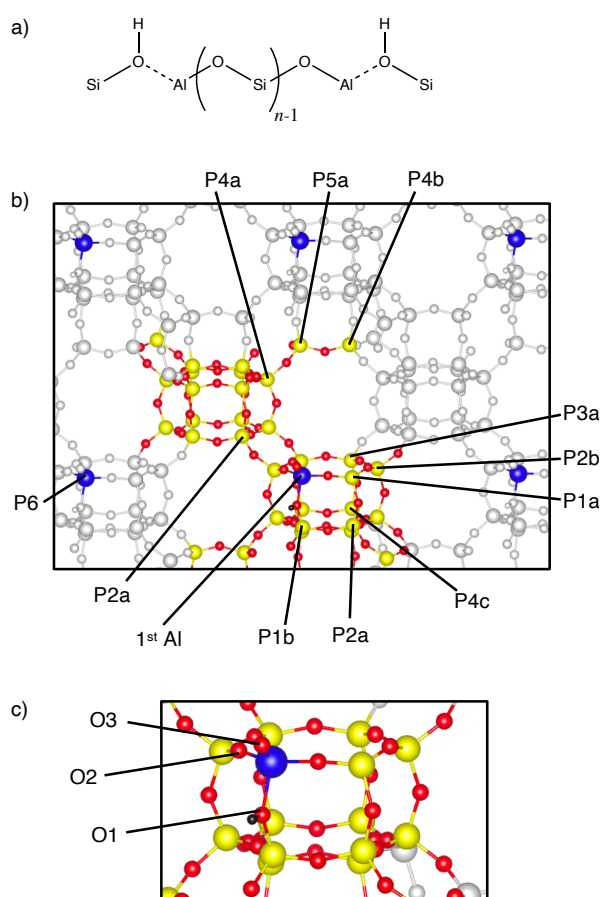


Figure 6.1: a) Relative position of two n -nearest neighbour aluminium atoms, starting from direct neighbours ($n = 1$), where no intermediate (-O-Si-) group is present to $n = 6$, which is the situation of an isolated Al atom per unit cell. b) Periodic structure of H-SSZ-13 with one Al per unit cell (shown in blue). The set of all silicon neighbours P_n is shown in yellow with the oxygens to which they are connected shown in red. c) Numbering scheme for the three oxygen atoms bound to the central Al atom.

Substitution of Si by Al is balanced by the introduction of a proton. Since every Al atom is bound to four oxygen atoms, there are always four different binding positions for the proton. In presence of methanol and water rapid equilibration should be expected such that a stable proton location is achieved. All possible variations (see also Figure C.1) of the protons were calculated i.e. all 16 choices of proton location for a given aluminium sitting. The stability of dual site structures is referenced relative to the catalyst P6 according to:

$$\Delta E(form) = E(P_n) + E(0Al) - 2 * E(P6) \quad (6.1)$$

where $E(P_n)$ is the total energy of the structure with two Al atoms per unit cell under consideration, $E(0Al)$ is the total energy of an unsubstituted, purely siliceous zeolite and $E(P6)$ is the total energy of a zeolite substituted with one Al atom. Figure 6.2 shows the stability of all possible combinations.

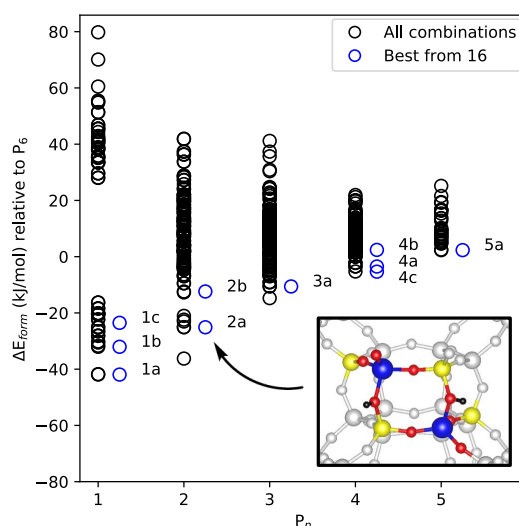


Figure 6.2: Stability of Al pairs as a function of distance. The energy is given relative to P6 the structure where the two Al atoms are separated by 5 (Si-O)-units. Motifs chosen for further study are shown slightly offset.

There is a considerable spread in formation energies with structures being up to more than 40 kJ/mol more stable and up to 80 kJ/mol less stable when compared to P6 (equation 6.1). Interestingly, there are structures which are more stable than P6 while violating Löwensteins rule ($n = 1$) with similar observations having been made in earlier studies [45, 186, 187]. Figure C.2 explores whether the stabilities of two acid sites can be simply understood in terms of additively combining two isolated BASs. It was found that this is not the case with the formation of internal hydrogen bonds meaning that some hard to predict structures are found to be the most stable, for example, for 4c a structure with both protons choosing to point into the 6dr ring was the most stable from 16 by around 5 kJ/mol. The most stable clean sites structures are highlighted in Figure 6.2 for the 10 Al combinations which will be used from here on in. The set was chosen to give balanced representation of zeolites with $n = 1 - 5$ (see Section C.2 for a more in-depth description of how these structures were chosen).

DME synthesis can proceed via either the stepwise or concerted mechanism (see Figure 6.3). In the former, two methanol molecules react in a concerted manner to produce DME and water. The latter occurs via two steps, (1) methanol adsorption followed by formation of a SMS and water and (2) reaction of the SMS with a second methanol to DME and the BAS. While the concerted mechanism has an overall lower enthalpic barrier, the TS has a larger entropic penalty thus the preferred reaction mechanism depends strongly on the temperature. TSs calculated with DFT, and PBE-D3 in particular, often have large errors when compared to higher level methods [2]. For example, the barrier for direct DME formation calculated with PBE-D3 is underestimated by 37 kJ/mol when compared to CCSD(T) [80] calculations. The emphasis here, however, is observing the trends imposed by aluminium proximity rather than absolute accurate numbers. Trends have been shown to be rather well-preserved at the GGA-DFT level of theory with errors of less than 5 kJ/mol [61].

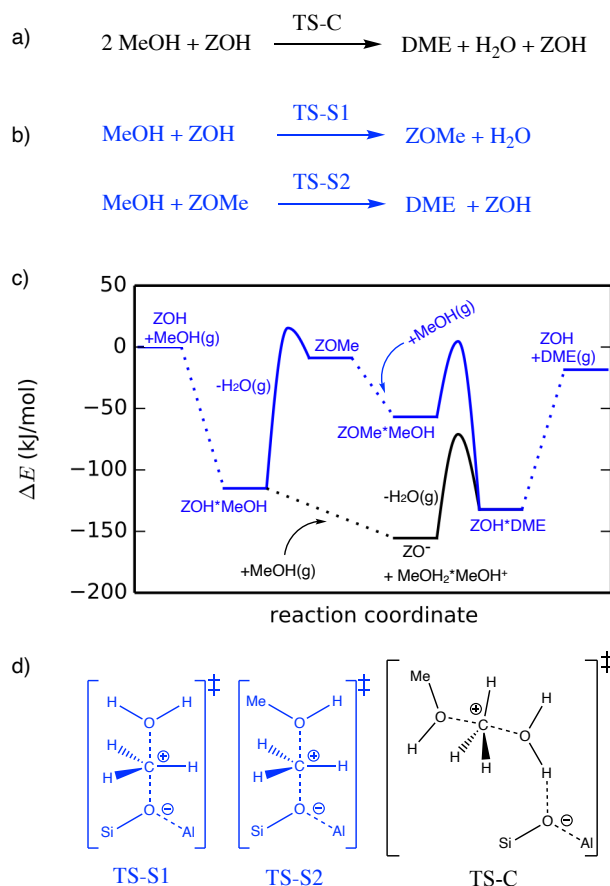


Figure 6.3: a) concerted and b) stepwise mechanism for DME-formation. c) Potential energy diagram of DME synthesis from methanol as calculated for H-SSZ-13 with a Si/Al ratio of 35 i.e. for the reference catalyst (P6). The black and blue pathways correspond to the concerted and stepwise mechanism respectively. All energies are referenced to the empty zeolite and two methanol molecules in the gas-phase at 0 K. An asterisk denotes an adsorbed species at either the acid site (ZOH) or the surface methoxy species (SMS). d) Illustration of the TSs in a-c).

Next the reaction mechanism presented in Figure 6.3 will be explored for the 10 chosen zeolites with 2 Al atoms per unit cell. In the two site regime the second site may directly interact with the first site and the reactants. Figure 6.4 a) shows a second clean BAS present while a reaction occurs at the first site. Looking back at the coverages and partial pressures Figure 4.2 this configuration has a high probability of being present. Figure 6.4 b) presents the initial state before concerted DME formation. The presence of the second site means the second methanol can now be bound more strongly than in the single site regime.

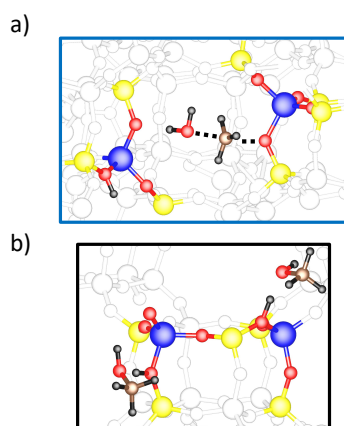


Figure 6.4: a) Stepwise SMS formation for motif 4c. b) Initial state before concerted DME formation for motif 2b.

Figure 6.5 shows the TS energies for all 10 motifs for SMS-formation both relative to gas-phase methanol (apparent barriers) as well as pre-adsorbed methanol (intrinsic barriers). The proton location at the second acid site determined using a variational approach, such that it is always in the most stable position (see Figure C.4). Furthermore, for each type of TS investigated TS isomers were systematically reoriented via scanning procedures in order to find reasonably stable configurations (see Section C.4). Some nearest neighbour structures have relatively low apparent barriers, for example, for 1b and 1c. However, very high barriers are observed for reactions occurring at the bridging oxygen (Al-O-Al), i.e. O3 for P1c and O1 for P1b. For the structures that obey Löwenstein's rule variations in intrinsic barriers are generally below 20 kJ/mol. The small variation in intrinsic barriers compared to apparent barriers also suggests a correlation between TS energies and the energy for methanol adsorption.

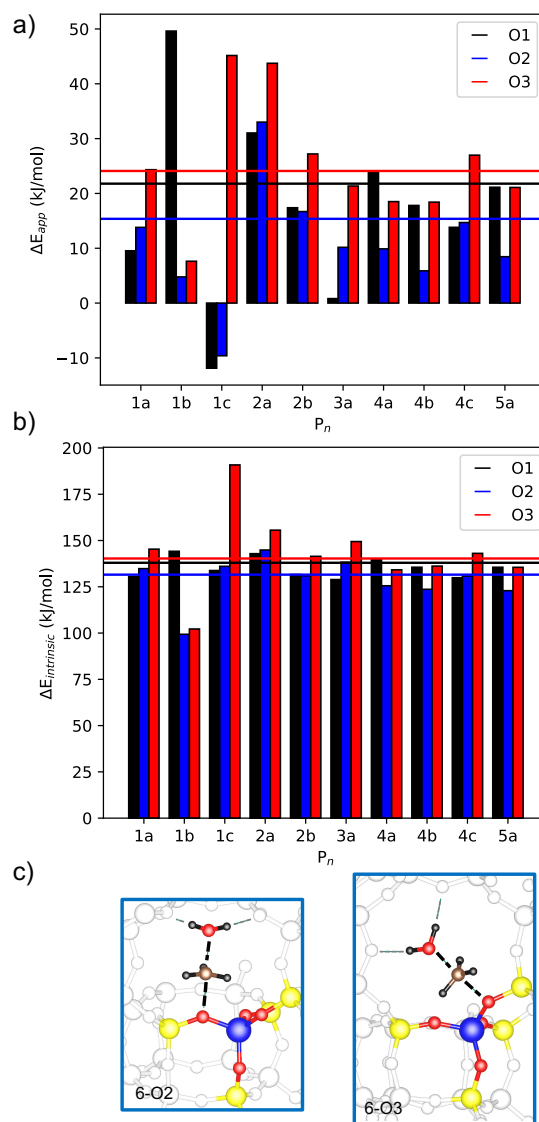


Figure 6.5: a) Apparent and b) intrinsic activation energies for SMS formation for selected Al pairs. SMS formation at three different oxygens is shown in black, red and blue and the barriers of the distant pair (P6) are shown as horizontal lines. The nomenclature for the oxygen location is illustrated in Figure 6.1 c). c) TSs for stepwise SMS formation occurring at O2 and O3.

Variations in energy barriers are often understood in terms of the acidity of the zeolite. There are various measures for the acidity of zeolites, such as the deprotonation energy [183], the O-H frequency shift upon CO adsorption [188] and the ammonia heat of adsorption, $E_{ads}(\text{NH}_3)$ [189]. Here the latter is chosen as a theoretical probe for the zeolites activity. Figure 6.6 shows the adsorption energy of methanol and the barrier for direct DME-formation as a function of $E_{ads}(\text{NH}_3)$. In agreement with reference [45] substitution of the second Al across the four-membered ring into a 2nd-nearest neighbour position (P2a, see inset in Figure 6.2) leads to a destabilisation of the concerted TS, while substitution across the six-membered ring into a 3rd-nearest neighbour position (P3a, see inset in Figure 6.6) leads to stabilisation and in fact to the lowest TS, not considering nearest neighbour positions.

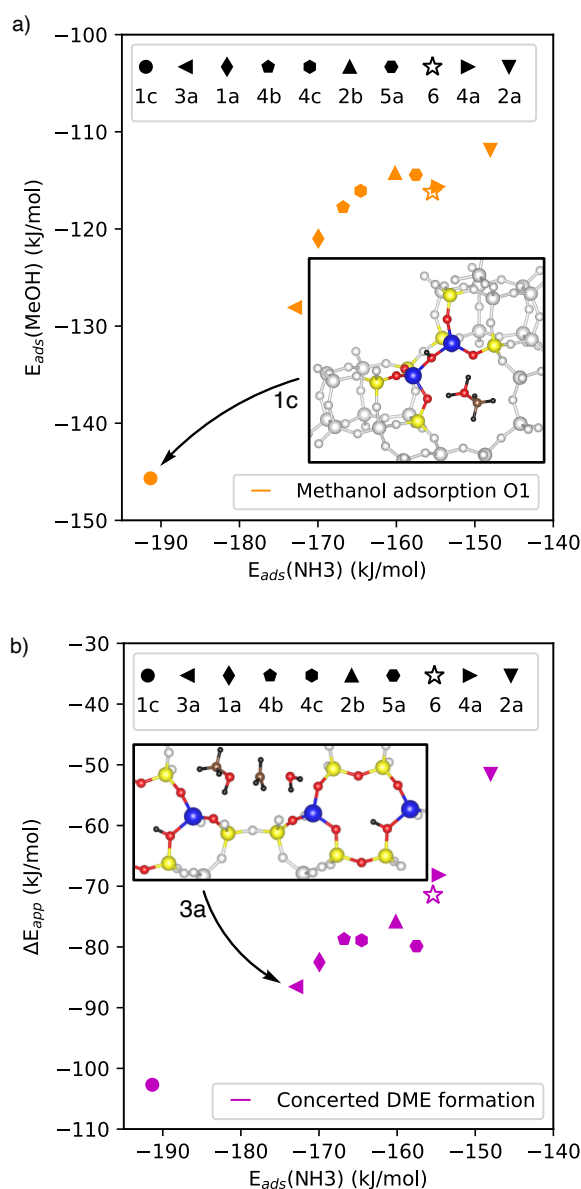


Figure 6.6: a) Adsorption energies of methanol. b) Apparent activation energies for direct DME-formation for selected Al pairs as a function of the adsorption energy of ammonia.

Figure 6.7 a) shows the TS energies for the first and second step of stepwise DME formation as a function of $E_{ads}(\text{NH}_3)$. For SMS-formation, the barrier is additionally investigated for formation of the SMS at three different oxygens. As for concerted DME-formation, the TS energies largely correlate well with acidity (see additionally Figure C.6). Similarly, structures P3a/P2a are particularly stable/unstable. Additionally, for isolated acid sites, SMS-formation is preferred at oxygen O2, where the TS is located within an eight-membered ring and two hydrogen bonds are formed between water and framework oxygen (see Figure 6.5 c)). As observed in [45] for the 3rd-nearest neighbour position across the six-membered ring (P3a), the most favourable oxygen for SMS-formation is O1. Due to the more stable methanol adsorption for this Al pair, the decrease in the apparent activation barrier (-21 kJ/mol relative to P6) does not carry over to the intrinsic barrier (-9 kJ/mol). Similarly, for structure P2a, the apparent barrier deviates more from P6 (+9 kJ/mol) than the intrinsic barrier (+5 kJ/mol). Figure 6.7 b) shows the changes in bond lengths for atoms involved in bond making and breaking. Overall the changes the bond lengths are relatively small being around 0.1 Å.

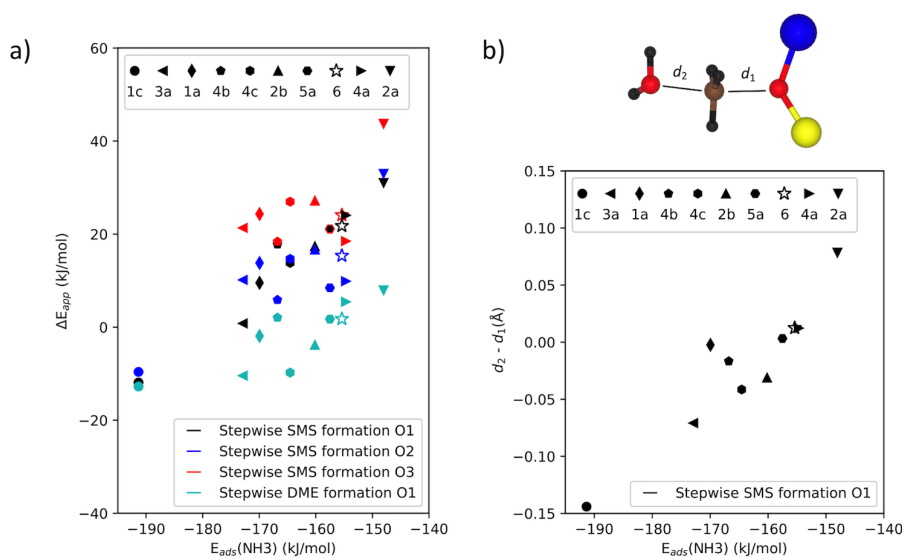


Figure 6.7: a) Apparent activation energies for stepwise DME-formation for selected Al pairs as a function of the adsorption energy of ammonia. (Stepwise SMS formation for O3 for P1c is not shown) b) Corresponding changes in the bond lengths of the TS structures.

So far this investigation has focused on clean additional BASs. However, an occupied secondary BAS can also affect the acidity at the first, for example, methanol can bridge across the 6-ring between the two acid sites and hydrogen bond with the first site. To shed light on this issue the calculations of 10 TSs for SMS formation at O1 were repeated with methanol adsorbed on the second acid site. The obtained apparent activation energies are shown in Figure 6.8 and compared with those obtained for the free acid site. The effect of the coadsorbed second methanol on the barrier is generally unsystematic and far smaller than the difference induced by the Al pair distribution. Thus the trends between the different Al pairs therefore remain largely unchanged. For the cases where the presence of the second methanol is expected to be at its most significant, for example, for motif 3a the overall decrease in the apparent barrier is around 10 kJ/mol.

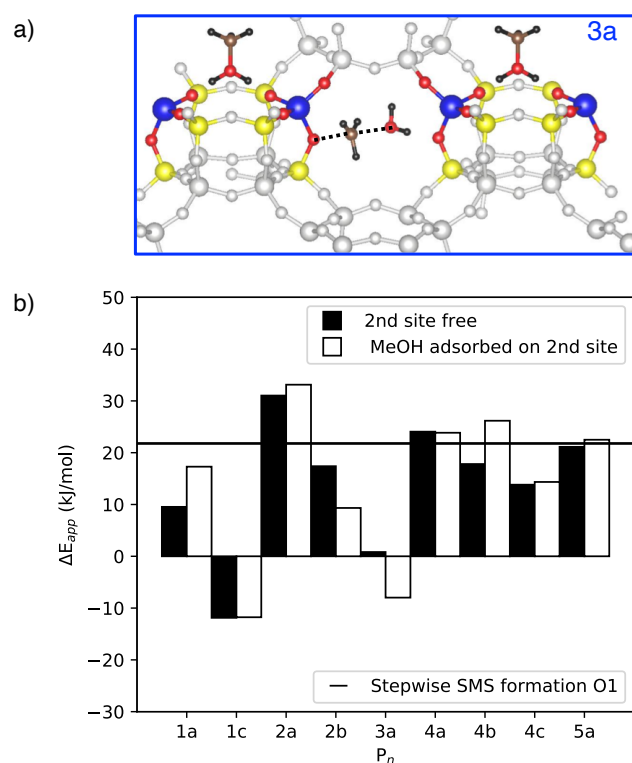


Figure 6.8: a) Illustration of the TS for P3a for SMS-formation with a coadsorbed MeOH at the second acid site. b) TS energies for SMS formation with a second methanol molecules coadsorbed at the second acid site.

All adsorption energies and activation barriers computed in this work are summarised in Figure 6.9 which shows a histogram of the deviation of these energies with respect to the most distant pair (P6) (Additionally, Figure C.7 shows all reactions profiles for the 10 motifs studied compared to the P6 regime). The largest differences are observed for nearest neighbour Al pairs with a mean absolute deviation (MAD) of 17.4 kJ/mol. Importantly, these pairs are not expected to form under usual synthesis conditions according to Löwenstein's rule. For typical more distant Al pairs expected for low Si/Al ratios, the influence of a neighbouring Al site is much less pronounced with most deviations within 20 kJ/mol and a MAD of 5.9 kJ/mol. Despite the correlation between adsorption energies and TSs (see Figures 6.6 and 6.7), deviations are similar for intrinsic and apparent barriers with a MAD of 5.8 and 7.0 kJ/mol, respectively (excluding nearest neighbour Al pairs).

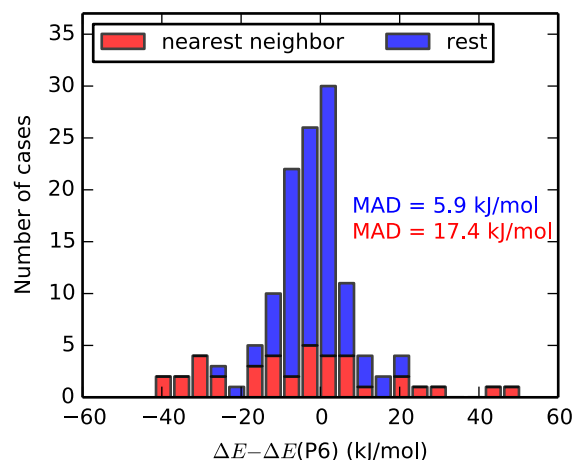


Figure 6.9: Statistics of the effect of proximate Al pairs, as measured relative to the adsorption energy, or activation barrier of structure P6. Nearest neighbour Al-O-Al pairs (violating Löwenstein’s rule) are shown in red, the remaining structures are shown in blue. The total height of the two sets of stacked bars corresponds to all structures.

6.3 Methods

DFT calculations were performed with the VASP program package in version 5.3.3.4 with the standard VASP-PAW potentials. The PBE density functional with the D3 dispersion correction (zero damping) from Grimme (PBE-D3) was employed. The Brillouin zone was sampled at the Γ point. A Gaussian smearing with a width of 0.1 eV was used. The cut-off energy for the plane waves was 400 eV, 800 eV was used for the optimisation of the unit cell. The optimised lengths of the lattice vectors of the unit cell of H-SSZ-13 are 13.625, 13.625 and 15.067 Å. All structures were fully relaxed and the convergence criteria for SCF cycles and geometry optimisations were 10^{-8} eV and $0.01 \frac{\text{eV}}{\text{Å}}$, respectively. The TSs were optimised using automated relaxed potential energy surface scans (ARPES). Harmonic force constants were computed from a central finite difference method where the oxygen at which the reaction occurs as well as the adjacent T-atoms were included. All TSs were verified to contain only one imaginary frequency corresponding to the transition vector of the reaction. In addition, the connectivity of TSs was confirmed through small displacement along the transition vector followed by optimisation to the corresponding minima.

6.4 Conclusion

The effects of the proximity and spatial orientation of Al pairs on the reactivity of the zeolite H-SSZ-13 were investigated. This was done for methanol dehydration to DME as a probe reaction, where both the concerted (associative) and stepwise (dissociative) mechanism were studied. The effect of Al pairs on adsorption and TS energies was investigated relative to the situation of a single acid site per unit cell (Si/Al ratio of 35), where the Al atom is separated by five (Si-O)-units from its periodic image. While most changes are in the 5 kJ/mol range, there are some notable outliers. The largest variations of up to 50 kJ/mol were found for direct Al-O-Al pairs which violate Löwenstein's rule. Both adsorption energies and activation barriers of the various Al pair distributions correlate well with the adsorption energy of ammonia, which was used as a descriptor for acidity. This leads to slight decrease in the variation of intrinsic barriers as compared to apparent barriers. In particular for the particularly reactive (3rd-nearest neighbour across the six-membered ring, P3a) and unreactive substitutions (2nd-nearest neighbour across the four-membered ring, P2a), these trends are diminished in the intrinsic activation barriers. Overall the apparent barriers show a mean absolute deviation (MAD) of 7 kJ/mol which lends credence to the idea that the commonly applied computational model exhibiting well separated acid sites (e.g. Si/Al=35 in H-SSZ-13) is also a good model for smaller Si/Al ratios. Larger deviations (MAD = 17 kJ/mol) were found for nearest neighbour aluminium substitutions, e.g. Al-O-Al pairs. These are, however, generally believed not to be formed under standard synthesis conditions according to Löwenstein's rule.

7 Trends in reactivity due to changing the choice of T-site in H-ZSM-5

7.1 Introduction

There are a large variety of different zeolites, which differ in both in their acidity and their microporous structure. H-SSZ-13 zeolite which was studied in the last chapter was a simple structure to study in the sense that with a high Si/Al ratio there is only one choice of Al sitting to explore. In general however, there are several T-sites where Al can be substituted. This chapter explores H-ZSM-5 in its orthorhombic high temperature form which occurs at typical MTO reaction conditions. H-ZSM-5 is the most commonly employed zeolite with MFI topology and has 12 different T-sites. The T-sites themselves have differing acidity and differing local confinement effects with some not being accessible by (larger) reactants rendering them inactive. It is conceivable that the overall activity of H-ZSM-5 is given by the sum of reactions occurring on all these different BASs. While this has implications for the preparation [28] and characterisation [190, 191] of H-ZSM-5, it also potentially complicates computational modelling and the investigation of reaction mechanisms.

Computational modelling, mostly based on DFT, has become an integral part of mechanistic studies shedding light on how BASs and the confinement effects of the surrounding framework influence specific reactions at the atomic level [192, 193]. Using DFT reaction barriers can be computed, allowing the search for rate-determining steps and the construction of kinetic models. The outcome of these computational studies depends on the limitations of DFT and the accuracy with which free energies are obtained [80, 194] but also on the structural model of the active site employed in the calculations [18, 44, 45, 63, 195]. Nowadays, it has become the standard to use periodic DFT and functionals that account for dispersion forces, which model the entire zeolite pore such that the confinement effects imposed by the framework are explicitly taken into account. Many employed models assume 1) high Si/Al ratios (typically one isolated acid site per unit cell) and 2) that the Al has been substituted at a specific location, for example, in H-ZSM-5 it has become the standard approach to calculate reaction mechanisms using the T12 site [130, 157, 183, 196] with only a few exceptions [18, 44, 63, 195, 197, 198]. One example of work exploring different possible Al substitutions is the work of Grabow and co-workers who calculated the reaction mechanism of DME synthesis for structural models of 4 of the 12 T-sites in H-ZSM-5 [18, 63]. In this chapter DFT is used at the PBE-D3 level to calculate the reaction barriers of five reactions related to the methanol-to-olefins (MTO) process over all 12 T-sites of H-ZSM-5. The study considers an isolated Al substitution and thus a Si/Al ratio of 95:1. How these sites differ in terms of reaction barrier heights and TS geometries will be investigated and how this is influenced by acidity and confinement will be discussed.

This chapter is based on the following publication: A.T.Smith, P.N.Plessow, and F.Studt, Acidity and Confinement of Aluminum T-site Substitution in H-ZSM-5. *In preparation.*

7.2 Results and discussion

Figure 7.1 shows the repeated unit cell of MFI in its Silicate form. Overall there are 96 tetrahedra in the unit cell with each T-site having a multiplicity of 8. All 12 possible choices of Al sitting are highlighted in the same positions used in all calculations and views along both the straight and sinusoidal channels are shown. The five reactions investigated are shown in Figure 7.2 with reactions investigated being strongly related to the MTO process. Reaction (1) is the formation of SMS by reaction of methanol with the BAS. This reaction also constitutes the first step of the dissociative mechanism of DME synthesis. The four other reactions are methylation of ethene (2), propene (3), n-butene (4) and benzene (5) all via a SMS.

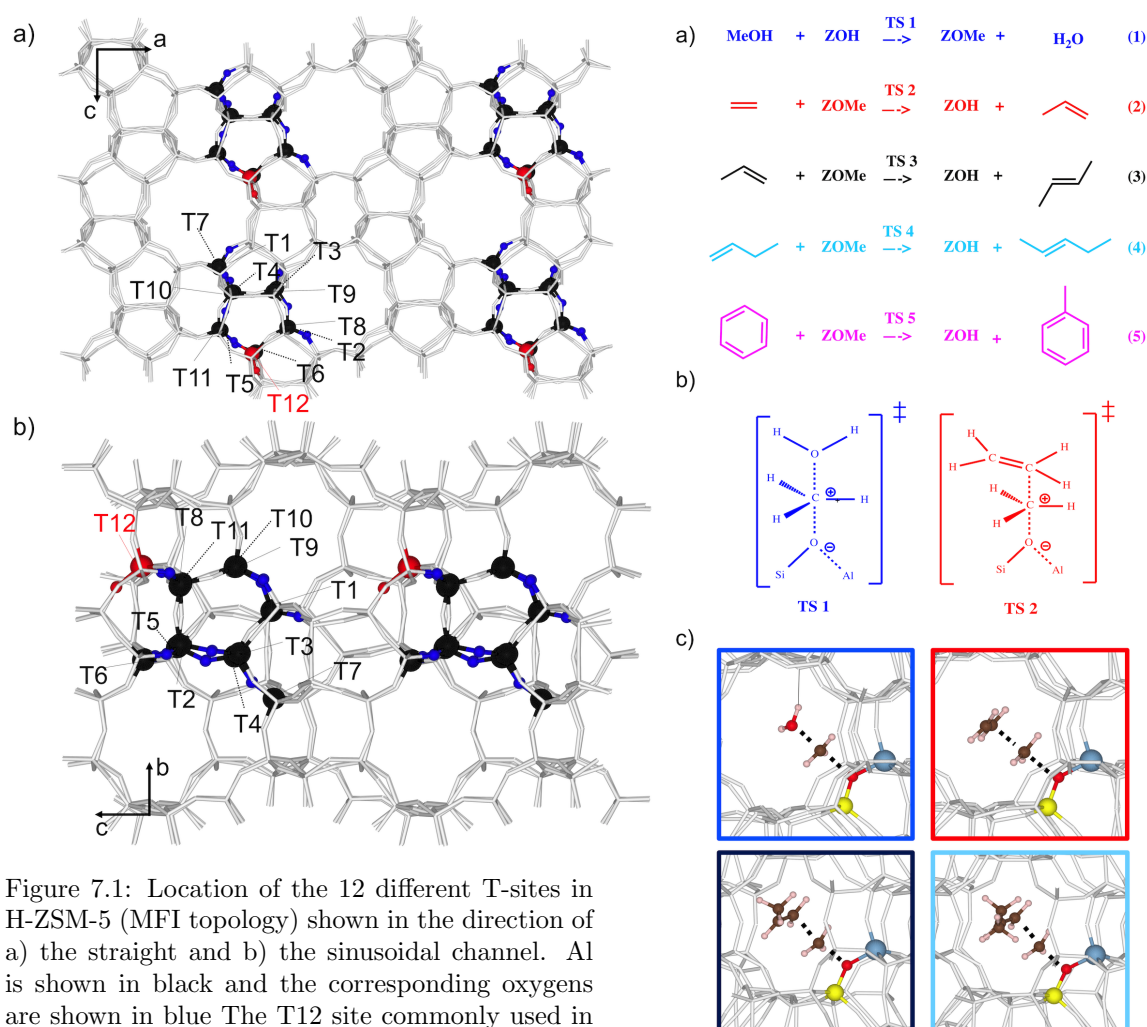


Figure 7.1: Location of the 12 different T-sites in H-ZSM-5 (MFI topology) shown in the direction of a) the straight and b) the sinusoidal channel. Al is shown in black and the corresponding oxygens are shown in blue. The T12 site commonly used in computational models is highlighted in red.

Figure 7.2: a) The five reactions investigated. Note that the same colour code is used throughout. b) Schematic representation of the TSs for SMS formation and ethene methylation by SMS. c) Calculated TS geometries of reactions (1), (2), (3) and (4) at the T12 site of H-ZSM-5 (H, white; Si, yellow; Al, light blue; O, red; C, brown).

Let's start by evaluating the stability of the different Al substitutions relative to the T12 site. Clean sites energies and ammonia adsorption energies were found for all possible alumina and proton sittings (see section D.1 in the Appendix) with the most stable proton position for each T-site used in further calculations. The most stable clean sites structures for each T-site are shown in table 7.1. The atom labels are the same as in reference [17]. Each BAS location can be compactly and unambiguously described, for example, Al-1-O-1-Si-2 indicates that Al sits at the first T-site and the hydrogen sits on the oxygen between T1 and T2. In agreement with earlier theoretical studies [18, 63] aluminium substitution at the T12 site is energetically favourable, only the T8 substitution is calculated to be slightly more stable (-0.6 kJ/mol). Most other substitutions are 5-10 kJ/mol less stable. The favourable stability along with the accessibility of the T12 location at the intersection of the two channels means that the majority of computational studies of H-ZSM-5 are based on the T12 site.

Table 7.1: Most stable clean sites structures and their corresponding oxygen locations.

T site	Clean site energy vs T12 (kJ/mol)	Chosen oxygen
T1	3.59	Al-1-O-1-Si-2
T2	3.27	Al-2-O-1-Si-1
T3	7.57	Al-3-O-2-Si-2
T4	7.15	Al-4-O-4-Si-5
T5	11.11	Al-5-O-5-Si-6
T6	13.63	Al-6-O-5-Si-5
T7	8.37	Al-7-O-17-Si 4
T8	-0.56	Al-8-O-7-Si-7
T9	11.54	Al-9-O-18-Si 6
T10	7.7	Al-10-O-15-Si 1
T11	9.95	Al-11-O-11-Si-12
T12	0	Al-12-O-20-Si-3

As in the last chapter NH₃ adsorption will be used as theoretical descriptor to measure the Brønsted acidity. Experimentally, it was found that the ammonia heat of adsorption does not vary significantly in H-ZSM-5 being on average 145 kJ/mol [199]. This compares rather well with the calculated adsorption energies in Table 7.2 which are in the narrow window of 138 to 160 kJ/mol with an average of value of -148 kJ/mol (-149 kJ/mol for the T12 site) similar results were also found by using DFT calculations by Grabow and co-workers [18].

Table 7.2 also shows the calculated values of the TS energies at all 12 different T-sites. All TSs are referenced to an SMS and the olefin in the gas-phase. At each T-site and for each reaction, the TS structures were systematically reoriented in order to ensure that only reasonably stable structures were considered (see Section D.2). The calculated values agree rather well with those reported in the literature. For example, SMS formation at the T12 site was calculated to be 22 kJ/mol relative to methanol in the gas-phase and the empty zeolite. Another study [200] using the same functional found the same barrier at the T12 site to be 19 kJ/mol. Similarly, for the methylation of ethene another PBE-D study [201] found a methylation barrier for ethene of 32 kJ/mol. In general when comparing the data for the methylation of ethene, propene and n-butene, it can be observed that there is a decrease of methylation barriers by around 30 kJ/mol for propene and 40 kJ/mol for butene methylation, when compared to that of ethene. Similar trends have been observed for other zeolites, e.g. H-SSZ-13 [37, 157] and have been attributed to the increased stabilisation of the cations as well as increases in vdW interactions with the zeolite framework. The reaction barriers employing the T12-site are at the lower end of the spectrum of calculated values with only T5 and T9 having consistently lower barriers. Comparing the four methylation reactions over the twelve T-sites of H-ZSM-5 reveals that the TS energies vary by about 20 kJ/mol. For example, ethene methylation has the lowest TS energy for the T9-site (26 kJ/mol) and the highest for the T1-site (50 kJ/mol), while this value is 34 kJ/mol for the commonly used T12-site.

Table 7.2: Overview of the calculated ammonia heat of adsorption and reaction barriers. All barriers are given relative to the empty zeolite or SMS, respectively, and the reactants in the gas-phase. All values in kJ/mol.

T-site	$\Delta E_{ads}(\text{NH}_3)$	Reaction barrier ΔE^\ddagger				
		(1)	(2)	(3)	(4)	(5)
1	-138	27	50	17	4	11
2	-138	26	49	19	2	16
3	-142	12	37	9	-3	14
4	-160	13	33	0	-6	32
5	-144	21	31	2	-14	0
6	-150	23	37	4	-9	5
7	-159	22	36	9	-2	37
8	-145	32	50	18	8	16
9	-149	22	26	-2	-11	17
10	-144	26	44	11	-3	4
11	-147	27	37	8	-7	0
12	-148	22	34	9	-8	10

Figure 7.3 compares the TS energies of propene and butene methylation with those of ethene. These relatively small reactants are in all likelihood marginally affected by vdW interactions caused by changing the local framework topology when going between different T-sites. The scaling of SMS formation and benzene with ethene formation as well as scaling of the barriers against ammonia adsorption were found to correlate less strongly (see section D.3). This can be attributed to stronger or weaker hydrogen bonding with the framework which depends strongly of the local confinement effects and to the relative bulkiness of benzene. The fact that the reaction barriers do not scale well when the T-site

is varied is again likely due to ammonia adsorption being too simple of a descriptor to capture the changing local environment.

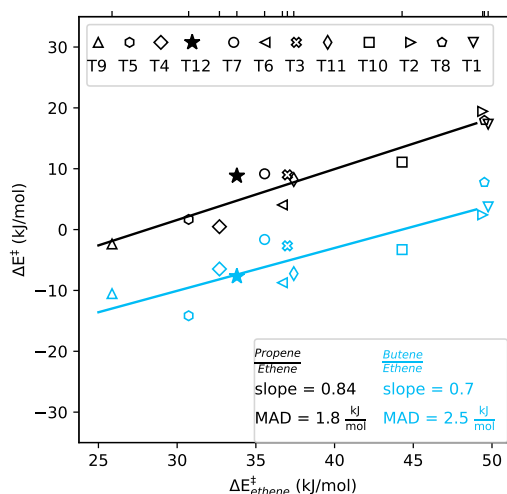


Figure 7.3: TS energies of propene (black) and n-butene (light blue) methylation via a SMS compared to that of ethene. All TSs are referenced to a SMS and the olefin in the gas-phase. The filled data points indicate calculations for the T12 site of H-ZSM-5.

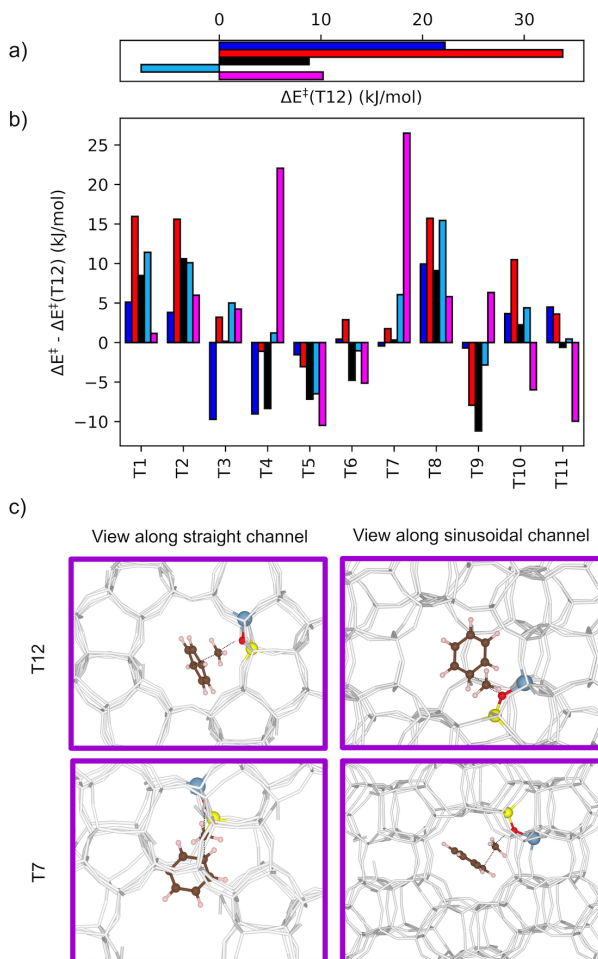


Figure 7.4: a) TS energies of reactions (1) to (5) calculated for the T12 site. b) Differences in TS energies of reactions (1) to (5) relative to the T12 site. c) Optimised geometries of the TSs of benzene methylation occurring at the T12 and T7 sites viewed both along the straight and sinusoidal channels.

Figure 7.4 further analyses how all five reaction barriers considered differ from that calculated for the T12 site. Generally, differences are less pronounced for smaller TS geometries, for example, SMS formation, and are largest for that of benzene methylation. The TS energy of benzene methylation is particularly high for the T4 and T7 sites. This can be ascribed to an increased steric repulsion due to these acid sites being difficult to access with parts of the benzene molecule being as close as 3.2 Å to the framework atoms.

Figure 7.5 divides the energy contribution of the TS energies into the PBE part that is derived from the solution of the KS equations and the dispersion part (D3) that is only a simple function of the position of the nuclei. These contributions are shown relative to those calculated for the T12 site. The TS for SMS formation (reaction (1)) at the T12 site has a PBE energy of 58 kJ/mol and contributions from vdW forces of -36 kJ/mol resulting in an overall barrier height of 22 kJ/mol relative to methanol in the gas phase. Interestingly, the PBE part of the methylation barriers (ethene to benzene, reactions (2) to (5)) at the T12-site are all fairly similar, with values between 73 kJ/mol (propene) and 88 kJ/mol (benzene). The major differences observed for the T12 site are thus due to the increase in vdW interactions, linearly increasing from ethene (-44 kJ/mol), over propene (-73 kJ/mol), to 1-butene (-84 kJ/mol), with benzene being similar to 1-butene (-77 kJ/mol). This agrees with earlier observations that the vdW interactions are a linear function of the numbers of atoms constituting the TS [157, 202]. Parts b) and c) of Figure 7.5 show how the PBE and D3 parts differ for the various T-sites compared to that of T12. Interestingly, the differences in PBE energies ($\Delta\Delta E(\text{PBE})$) and dispersion interactions ($\Delta\Delta E(\text{D3})$) are comparable with MADs of 7.2 and 5.3 kJ/mol respectively. For most TSs they differ by less than 10 kJ/mol, with the exception of benzene methylation at T4 and T7 that are due to strong steric hinderance caused by the acid site being difficult to access. This is in line with the ammonia heat of adsorption (as a measure of acidity) that changes by a similar magnitude across the twelve T-sites (see Table 7.2). Overall the acidity and confinement effects caused by different alumina sittings are reasonably small differing on average by around plus or minus 10kJ/mol at most. For bulky TS geometries and less accessible acid sites, however, there can be repulsive interactions of the order 20 kJ/mol as evidenced by benzene methylation.

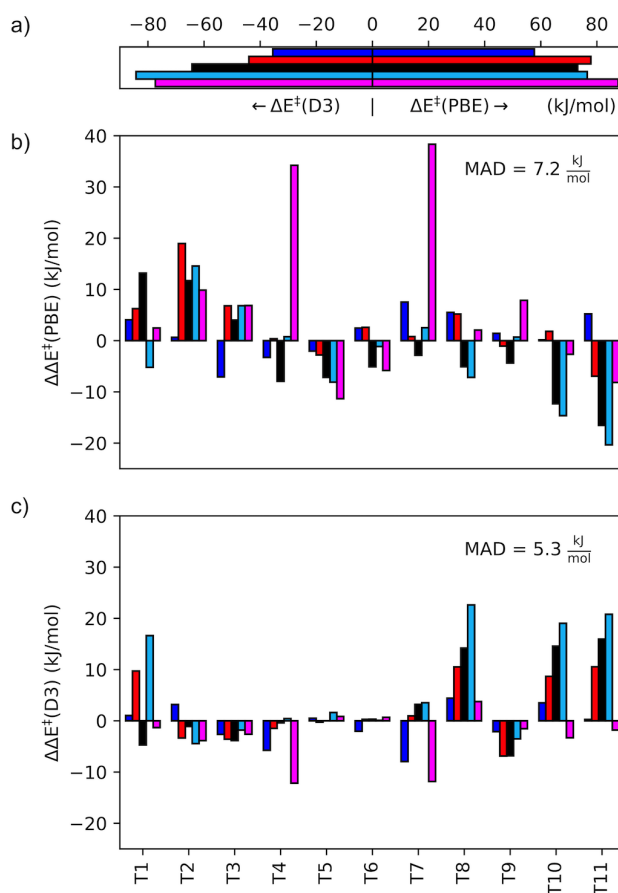


Figure 7.5: a) ΔPBE and ΔD3 TS energies of reactions (1) to (5) calculated for the T12 site. b) $\Delta\Delta\text{PBE}$ energies of all other T-sites relative to those obtained for T12. c) $\Delta\Delta\text{D3}$ energies of all other T-sites relative to those obtained for T12.

So far the analysis only considered the TS energies relative to the reactants in the gas-phase. Next intrinsic barriers for SMS formation which depend on the difference between the energy of the TS and that of pre-adsorbed methanol will be explored. A comparison of intrinsic barriers and values for methanol adsorption are given in Table 7.3. Interestingly, the spread in adsorption energies of methanol is rather small with the T3 site having the

weakest (-113 kJ/mol) and the T7 and T12 site having the strongest adsorption energies (-124 kJ/mol). The data is generally in good agreement with other values reported in the literature [200, 201]. TS energies for SMS formation range from 12 to 27 kJ/mol and 126 to 149 kJ/mol for the apparent and intrinsic barriers, respectively, thus having similar spreads. This means that the choice of reference state (gas-phase vs adsorbed methanol) has only a small influence on the overall observed trends for SMS formation.

Table 7.3: Calculated adsorption energies for methanol and reaction barriers for SMS formation relative to gas-phase (ΔE_{app}^\ddagger) and adsorbed methanol (ΔE_{int}^\ddagger). All values in kJ/mol.

T-site	$\Delta E_{ads}(\text{MeOH})$	SMS formation barrier ΔE^\ddagger	
		ΔE_{app}^\ddagger	ΔE_{int}^\ddagger
1	-116	27	143
2	-116	26	142
3	-113	12	126
4	-123	13	136
5	-120	21	141
6	-121	23	143
7	-124	22	146
8	-117	32	149
9	-120	22	141
10	-123	26	149
11	-114	27	140
12	-124	22	146

Figure 7.6 compares all energy barriers and adsorptions presented in this study to those obtained for the commonly used T12 site. Overall, roughly one third (36%) is lower in energy than T12, with two thirds (64%) showing higher energies. While there can be significant deviations of the order 20 kJ/mol in some cases, overall the low MAD of 6 kJ/mol indicates that, at least statically speaking, choosing to model H-ZSM-5 with the T12 site is a reasonable choice.

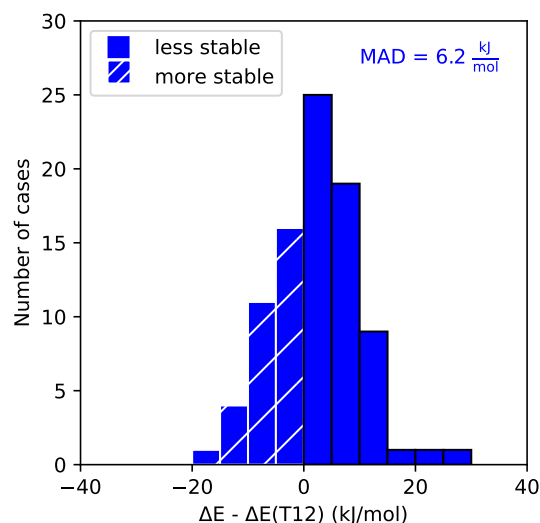


Figure 7.6: Statistics of the effect of alumina sitting in H-ZSM-5, as measured relative to the adsorption energies and activation barriers calculated for the T12 site for all data presented. The width of the stacked bars is 5 kJ/mol.

7.3 Methods

DFT calculations were performed using the VASP program package in version 5.3.3.4 with the standard VASP-PAW potentials. The PBE density functional with Grimme’s D3 dispersion correction (zero damping) from (PBE-D3) was employed. The Brillouin-zone was sampled at the Γ point. Gaussian smearing with a width of 0.1 eV was used. The cut-off energy for the plane waves was 400 eV, while 800 eV was used for the optimisation of the lattice parameters. The optimised lengths of the lattice vectors of the unit cell of H-ZSM-5 are 20.340, 19.988 and 13.492 Å, as also used in earlier theoretical studies [157]. All structures have been fully relaxed and the convergence criteria for SCF cycles and geometry optimisation were 10^{-8} eV and $0.01 \frac{\text{eV}}{\text{Å}}$, respectively. The transition states were optimised using ARPES. Harmonic force constants were computed from a central finite difference method where the oxygen at which the reaction occurs as well as the adjacent T-atoms were included. All transition states were verified to contain only a single imaginary frequency corresponding to the transition vector of the reaction. In addition, the connectivity of transition states was confirmed through small displacement along the transition vector followed by optimisation to the corresponding minima.

7.4 Conclusion

The influence of the acid site location in H-ZSM-5 on TS energies of reactions related to the MTO process was investigated. Overall, TS energies vary by about 20 kJ/mol with the commonly employed T12 site having some of the lowest barriers. The energetic differences when going between different T-sites can be ascribed to both, differences in acidity and to confinement effects. While the analysis is based on the PBE-D3 functional which often underestimates reaction barriers related to the MTO process [80], energy differences are still well described at this level of theory [61]. The current study does not include changes in entropy contributions which are in many cases calculated using the harmonic approximation. These contributions have been shown to vary only to a minor extent between different acid sites [58], thus the overall trends are likely to be captured by the methods employed here. The analysis thus reveals that taking the T12 site as a computational model catalyst will give reaction barriers that are among the lowest of all T-sites available. The T12 model catalyst will capture the lowest TSs rather well if one assumes that all T-sites are present. This gives confidence to the commonly employed T12 model catalyst. However, one should also be aware that barriers can vary by 20 kJ/mol between the various T-sites, which translates to differences in rate constants of more than two orders of magnitude at relevant operating conditions.

8 Final outlook and conclusions

The aim of this thesis was to investigate extensions to how the MTO process is currently modelled. The two main topics were microkinetic modelling based upon highly accurate chemical barriers from the DFT:MP2 level of theory and to study the influence of catalyst structure upon reactivity.

In Chapter 4 a simple batch reactor model for 105 reactions from the MTO process was implemented. A long-standing question is where the first HP species come from? Is it due to impurities in the feed or is it due to a direct initiation mechanism? This model qualitatively showed a direct initiation mechanism involving the formation of a C-C double bond is viable in the absence of impurities. The key pathways were methanol dehydrogenation to CO and subsequent CO methylation which leads to the first C-C double bond.

The simple batch reactor model from chapter 4 explicitly assumed perfect mixing when of course in reality it can be difficult or in many cases impossible for large species to move between zeolite cavities. In chapter 5 diffusion limitations were studied from the perspective of the atomic scale in H-SSZ-13 zeolite. The effective diameter was used as an intuitive predictor of the diffusion barriers. Small species e.g. ethene can easily pass through the zeolite pores and bulkier molecules such as benzene have large diffusion barriers and small diffusion constants.

Chapter 6 investigated the effects of adding a secondary BAS on reactions occurring at a first BAS for the methanol dehydration pathway. The study was done in H-SSZ-13 due to its high symmetry with all choices of Al location being symmetry equivalent. Some motifs such as 3a with the second site placed at the 3rd-nearest neighbour across the six-membered ring were found to be particularly reactive. However, the intrinsic activity for all structures considered was found to lie within a very small range for non-nearest neighbour structures which are most likely to be formed under normal synthesis conditions.

Chapter 7 built on the work from Chapter 6 this time modelling 5 key reactions in H-ZSM-5 which has 12 symmetry inequivalent sites. The results demonstrate that individual elementary reactions can be highly dependent upon the confinement effects related to which Al sitting is present which in turn depends on how the catalyst was synthesised. The commonly modelled T12 site was found to yield some of the lowest barriers on average which lends credit to the idea that the T12 should be chosen on the basis of accessibility.

Controlling the location and proximity of BASs is currently a difficult but nonetheless feasible task at the experimental scale. It is also possible to synthesise stable zeolite catalysts with far lower Si/Al ratios than have been explored in this work. Future zeolite synthesis should aim to produce some of the more catalytically active motifs found in Chapters 6 and 7. Future modelling of catalyst structure could focus on combinations of more than two acid sites in H-SSZ-13 and more than one in H-ZSM-5. Although the number of possible combinations grows very quickly with the number of BASs explored each individual structure can be generated straightforwardly and automatically meaning it's a feasible task to screen a wide variety of Si/Al ratios for highly stable and highly active structures. Overall however, it was found that the commonly employed acid site

models of one acid site per unit cell in H-SSZ-13 and locating the Al at the T12 site in H-ZSM-5 are on average extremely reasonable. Thus more focus should be directed towards exploring more pathways in the reaction mechanism using these simple acid site models.

In future work a similar kinetic treatment should include spatial variations in the concentrations with mass and heat transfer limitations taken into account. At a minimum this would involve using the simple to compute effective diameter explored in Chapter 5 but a more careful treatment would likely involve computing diffusion barriers for all intermediates studied. Eventually kinetic modelling should be done for the later stages of the MTO process in order to make predictions about the observed product distribution and to predict which species are involved in deactivation. This is a large task requiring a comprehensive reaction mechanism and an appreciation of its dual-cycle nature. The most important steps in both the olefin cycle and the aromatic cycle should be taken into account including olefin formation via the aromatic cycle and also aromatic formation via cyclisation of olefins.

References

- [1] K. Hemelsoet, J. Van der Mynsbrugge, K. De Wispelaere, M. Waroquier, and V. Van Speybroeck, "Unraveling the reaction mechanisms governing methanol-to-olefins catalysis by theory and experiment", *ChemPhysChem*, vol. 14, no. 8, pp. 1526–1545, 2013.
- [2] P. N. Plessow and F. Studt, "Unraveling the mechanism of the initiation reaction of the methanol to olefins process using ab initio and dft calculations", *ACS Catal*, vol. 7, no. 11, pp. 7987–7994, 2017.
- [3] V. Van Speybroeck, K. Hemelsoet, L. Joos, M. Waroquier, R. G. Bell, and C. R. A. Catlow, "Advances in theory and their application within the field of zeolite chemistry", *Chem. Soc. Rev*, vol. 44, pp. 7044–7111, 2015.
- [4] U. Olsbye, S. Svelle, K. P. Lillerud, Z. H. Wei, Y. Y. Chen, J. F. Li, J. G. Wang, and W. B. Fan, "The formation and degradation of active species during methanol conversion over protonated zeotype catalysts", *Chem. Soc. Rev*, vol. 44, pp. 7155–7176, 2015.
- [5] P. N. Plessow and F. Studt, "Olefin methylation and cracking reactions in h-ssz-13 investigated with ab initio and dft calculations", *Catal. Sci. Technol*, vol. 8, pp. 4420–4429, 2018.
- [6] M. Stöcker, "Methanol-to-hydrocarbons: Catalytic materials and their behavior", *Microporous Mesoporous Mater*, vol. 29, no. 1, pp. 3–48, 1999.
- [7] U. Olsbye *et al.*, "Conversion of methanol to hydrocarbons: How zeolite cavity and pore size controls product selectivity", *Angew. Chem. Int. Ed*, vol. 51, no. 24, pp. 5810–5831, 2012.
- [8] W. Song, D. M. Marcus, H. Fu, J. O. Ehresmann, and J. F. Haw, "An oft-studied reaction that may never have been: Direct catalytic conversion of methanol or dimethyl ether to hydrocarbons on the solid acids hzsm-5 or hsapo-34", *J. Am. Chem. Soc*, vol. 124, no. 15, pp. 3844–3845, 2002.
- [9] P. Tian, Y. Wei, M. Ye, and Z. Liu, "Methanol to olefins (mto): From fundamentals to commercialization", *ACS Catal*, vol. 5, no. 3, pp. 1922–1938, 2015.
- [10] I. Yarulina, A. D. Chowdhury, F. Meirer, B. M. Weckhuysen, and J. Gascon, "Recent trends and fundamental insights in the methanol-to-hydrocarbons process", *Nat. Catal*, vol. 1, no. 6, pp. 398–411, 2018.
- [11] V. Van Speybroeck, J. Van der Mynsbrugge, M. Vandichel, K. Hemelsoet, D. Lesthaeghe, A. Ghysels, G. B. Marin, and M. Waroquier, "First principle kinetic studies of zeolite-catalyzed methylation reactions", *J. Am. Chem. Soc*, vol. 133, no. 4, pp. 888–899, 2011.
- [12] Y. Li, L. Li, and J. Yu, "Applications of zeolites in sustainable chemistry", *Chem*, vol. 3, no. 6, pp. 928–949, 2017.
- [13] G. A. Olah, "Beyond oil and gas: The methanol economy", *Angew. Chem. Int. Ed*, vol. 44, no. 18, pp. 2636–2639, 2005.
- [14] C. Baerlocher and L. McCusker, Eds., *Database of Zeolite Structures*. <http://www.iza-structure.org/databases/>.
- [15] T. Pang, X. Yang, C. Yuan, A. A. Elzatahry, A. Alghamdi, X. He, X. Cheng, and Y. Deng, "Recent advance in synthesis and application of heteroatom zeolites", *Chin. Chem. Lett*, vol. 32, no. 1, pp. 328–338, 2021.
- [16] L. S. Dent and J. V. Smith, "Crystal structure of chabazite, a molecular sieve", *Nature*, vol. 181, no. 4626, pp. 1794–1796, 1958.
- [17] D. H. Olson, G. T. Kokotailo, S. L. Lawton, and W. M. Meier, "Crystal structure and structure-related properties of zsm-5", *J. Phys. Chem*, vol. 85, no. 15, pp. 2238–2243, 1981.
- [18] A. Ghorbanpour, J. D. Rimer, and L. C. Grabow, "Periodic, vdW-corrected density functional theory investigation of the effect of al siting in h-zsm-5 on chemisorption properties and site-specific acidity", *Catal. Commun*, vol. 52, pp. 98–102, 2014.
- [19] C. Baerlocher, L. B. McCusker, and D. H. Olson, Eds., *Atlas of Zeolite Framework Types (Sixth Edition)*. Amsterdam: Elsevier Science B.V., 2007.
- [20] D. J. Earl and M. W. Deem, "Toward a database of hypothetical zeolite structures", *Ind. Eng. Chem. Res*, vol. 45, no. 16, pp. 5449–5454, 2006.
- [21] M. W. Deem, R. Pophale, P. A. Cheeseman, and D. J. Earl, "Computational discovery of new zeolite-like materials", *J. Phys. Chem C*, vol. 113, no. 51, pp. 21353–21360, 2009.
- [22] J. K. Nørskov, T. Bligaard, J. Rossmeisl, and C. H. Christensen, "Towards the computational design of solid catalysts", *Nat. Chem*, vol. 1, no. 1, pp. 37–46, 2009.
- [23] W. Vermeiren and J.-P. Gilson, "Impact of zeolites on the petroleum and petrochemical industry", *Top. Catal*, vol. 52, no. 9, pp. 1131–1161, 2009.
- [24] R. Prins, *Introduction to heterogeneous catalysis*, A. Wang and X. Li, Eds., ser. Advanced textbooks in chemistry ; Vol. 1. London: World Scientific, 2016, ch. 4.
- [25] A. Primo and H. Garcia, "Zeolites as catalysts in oil refining", *Chem. Soc. Rev*, vol. 43, pp. 7548–7561, 2014.
- [26] B. Smit and T. L. M. Maesen, "Towards a molecular understanding of shape selectivity", *Nature*, vol. 451, no. 7179, pp. 671–678, 2008.
- [27] B. P. Hereijgers, F. Bleken, M. H. Nilsen, S. Svelle, K.-P. Lillerud, M. Bjørgen, B. M. Weckhuysen, and U. Olsbye, "Product shape selectivity dominates the methanol-to-olefins (mto) reaction over h-sapo-34 catalysts", *J. Catal*, vol. 264, no. 1, pp. 77–87, 2009.
- [28] J. Děddeck, Z. Sobalík, and B. Wichterlová, "Siting and distribution of framework aluminium atoms in silicon-rich zeolites and impact on catalysis", *Catal. Rev*, vol. 54, no. 2, pp. 135–223, 2012.
- [29] J. A. Ryder, A. K. Chakraborty, and A. T. Bell, "Density functional theory study of proton mobility in zeolites: Proton migration and hydrogen exchange in zsm-5", *J. Phys. Chem. B*, vol. 104, no. 30, pp. 6998–7011, 2000.
- [30] I. M. Dahl and S. Kolboe, "On the reaction mechanism for hydrocarbon formation from methanol over sapo-34: I. isotopic labeling studies of the co-reaction of ethene and methanol", *J. Catal*, vol. 149, no. 2, pp. 458–464, 1994.
- [31] W. Song, H. Fu, and J. F. Haw, "Selective synthesis of methylnaphthalenes in hsapo-34 cages and their function as reaction centers in methanol-to-olefin catalysis", *J. Phys. Chem. B*, vol. 105, no. 51, pp. 12839–12843, 2001.
- [32] J. F. Haw, "Zeolite acid strength and reaction mechanisms in catalysis", *Phys. Chem. Chem. Phys*, vol. 4, pp. 5431–5441, 2002.
- [33] W. Song, J. F. Haw, J. B. Nicholas, and C. S. Heneghan, "Methylbenzenes are the organic reaction centers for methanol-to-olefin catalysis on hsapo-34", *J. Am. Chem. Soc*, vol. 122, no. 43, pp. 10726–10727, 2000.
- [34] W. Wang, A. Buchholz, M. Seiler, and M. Hunger, "Evidence for an initiation of the methanol-to-olefin process by reactive surface methoxy groups on acidic zeolite catalysts", *J. Am. Chem. Soc*, vol. 125, no. 49, pp. 15260–15267, 2003.
- [35] C.-M. Wang, Y.-D. Wang, Y.-J. Du, G. Yang, and Z.-K. Xie, "Similarities and differences between aromatic-based and olefin-based cycles in h-sapo-34 and h-ssz-13 for methanol-to-olefins conversion: Insights from energetic span model", *Catal. Sci. Technol*, vol. 5, pp. 4354–4364, 2015.
- [36] A. D. Chowdhury, K. Houben, G. T. Whiting, M. Mokhtar, A. M. Asiri, S. A. Al-Thabaiti, S. N. Basahel, M. Baldus, and B. M. Weckhuysen, "Initial carbon-carbon bond formation during the early stages of the methanol-to-olefin process proven by zeolite-trapped acetate and methyl acetate", *Angew. Chem. Int. Ed*, vol. 55, no. 51, pp. 15840–15845, 2016.
- [37] C.-M. Wang, Y.-D. Wang, and Z.-K. Xie, "Insights into the reaction mechanism of methanol-to-olefins conversion in hsapo-34 from first principles: Are olefins themselves the dominating hydrocarbon pool species?", *J. Catal*, vol. 301, pp. 8–19, 2013.

- [38] J. Haw, W. Song, D. Marcus, and J. Nicholas, "The mechanism of methanol to hydrocarbon catalysis", *Acc. Chem. Res.*, vol. 36, no. 5, pp. 317–326, 2003.
- [39] A. Bhan and E. Iglesia, "A link between reactivity and local structure in acid catalysis on zeolites", *Acc. Chem. Res.*, vol. 41, no. 4, pp. 559–567, 2008.
- [40] M. Bjørgen, S. Akyalcin, U. Olsbye, S. Benard, S. Kolboe, and S. Svelle, "Methanol to hydrocarbons over large cavity zeolites: Toward a unified description of catalyst deactivation and the reaction mechanism", *J. Catal.*, vol. 275, no. 1, pp. 170–180, 2010.
- [41] R. Y. Brogaard, B. M. Weckhuysen, and J. K. Nørskov, "Guest–host interactions of arenes in h-zsm-5 and their impact on methanol-to-hydrocarbons deactivation processes", *J. Catal.*, vol. 300, pp. 235–241, 2013.
- [42] E. Epelde, M. Ibañez, A. T. Aguayo, A. G. Gayubo, J. Bilbao, and P. Castaño, "Differences among the deactivation pathway of hzsm-5 zeolite and sapo-34 in the transformation of ethylene or 1-butene to propylene", *Microporous Mesoporous Mater.*, vol. 195, pp. 284–293, 2014.
- [43] J. Dědeček, E. Tabor, and S. Sklenak, "Tuning the aluminum distribution in zeolites to increase their performance in acid-catalyzed reactions", *ChemSusChem*, vol. 12, no. 3, pp. 556–576, 2019.
- [44] S. Nystrom, A. Hoffman, and D. Hibbitts, "Tuning brønsted acid strength by altering site proximity in cha framework zeolites", *ACS catal.*, vol. 8, no. 9, pp. 7842–7860, 2018.
- [45] A. J. Hoffman, J. S. Bates, J. R. Di Iorio, S. V. Nystrom, C. T. Nimlos, R. Gounder, and D. Hibbitts, "Rigid arrangements of ionic charge in zeolite frameworks conferred by specific aluminum distributions preferentially stabilize alkanol dehydration transition states", *Angew. Chem. Int. Ed.*, vol. 59, no. 42, pp. 18 686–18 694, 2020.
- [46] J. R. Di Iorio, C. T. Nimlos, and R. Gounder, "Introducing catalytic diversity into single-site chabazite zeolites of fixed composition via synthetic control of active site proximity", *ACS catal.*, vol. 7, no. 10, pp. 6663–6674, 2017.
- [47] G. A. Somorjai and Y. Li, "Major successes of theory-and-experiment-combined studies in surface chemistry and heterogeneous catalysis", *Top. Catal.*, vol. 53, no. 5, pp. 311–325, 2010.
- [48] P. Magnoux, P. Roger, C. Canaff, V. Fouche, N. Gnep, and M. Guisnet, "New technique for the characterization of carbonaceous compounds responsible for zeolite deactivation", in *Catalyst Deactivation 1987*, B. Delmon and G. Froment, Eds., vol. 34, Elsevier, 1987, pp. 317–330.
- [49] T. Mole, J. A. Whiteside, and D. Seddon, "Aromatic co-catalysis of methanol conversion over zeolite catalysts", *J. Catal.*, vol. 82, no. 2, pp. 261–266, 1983.
- [50] D. Mores, E. Stavitski, M. H. F. Kox, J. Kornatowski, U. Olsbye, and B. M. Weckhuysen, "Space- and time-resolved in-situ spectroscopy on the coke formation in molecular sieves: Methanol-to-olefin conversion over h-zsm-5 and h-sapo-34", *Chem. Eur. J.*, vol. 14, no. 36, pp. 11 320–11 327, 2008.
- [51] I. L. C. Buurmans and B. M. Weckhuysen, "Heterogeneities of individual catalyst particles in space and time as monitored by spectroscopy", *Nat. Chem.*, vol. 4, no. 11, pp. 873–886, 2012.
- [52] J. K. Nørskov, F. Studt, F. Abild-Pedersen, and T. Bligaard, *Fundamental Concepts in Heterogeneous Catalysis*. John Wiley & Sons, Ltd, 2014.
- [53] J. K. Nørskov, F. Abild-Pedersen, F. Studt, and T. Bligaard, "Density functional theory in surface chemistry and catalysis", *PNAS*, vol. 108, no. 3, pp. 937–943, 2011.
- [54] C. H. Christensen and J. K. Nørskov, "A molecular view of heterogeneous catalysis", *J. Chem. Phys.*, vol. 128, no. 18, p. 182 503, 2008.
- [55] S. Curtarolo, G. L. W. Hart, M. B. Nardelli, N. Mingo, S. Sanvito, and O. Levy, "The high-throughput highway to computational materials design", *Nat. Mater.*, vol. 12, no. 3, pp. 191–201, 2013.
- [56] Z.-J. Zhao, S. Liu, S. Zha, D. Cheng, F. Studt, G. Henkelman, and J. Gong, "Theory-guided design of catalytic materials using scaling relationships and reactivity descriptors", *Nat. Rev. Mater.*, vol. 4, no. 12, pp. 792–804, 2019.
- [57] J. Greeley, "Theoretical heterogeneous catalysis: Scaling relationships and computational catalyst design", *Annu. Rev. Chem. Biomol. Eng.*, vol. 7, no. 1, pp. 605–635, 2016.
- [58] R. Y. Brogaard, C.-M. Wang, and F. Studt, "Methanol–alkene reactions in zeotype acid catalysts: Insights from a descriptor-based approach and microkinetic modeling", *ACS catal.*, vol. 4, no. 12, pp. 4504–4509, 2014.
- [59] M. G. Evans and M. Polanyi, "Inertia and driving force of chemical reactions", *Trans. Faraday Soc.*, vol. 34, pp. 11–24, 1938.
- [60] R. P. Bell, "Relations between the energy and entropy of solution and their significance", *Trans. Faraday Soc.*, vol. 33, pp. 496–501, 1937.
- [61] P. N. Plessow and F. Studt, "How accurately do approximate density functionals predict trends in acidic zeolite catalysis?", *J. Phys. Chem. Lett.*, vol. 11, no. 11, pp. 4305–4310, 2020.
- [62] P. Cnudde, K. Wispeleere, J. der Mynsbrugge, M. Waroquier, and V. V. Speybroeck, "Effect of temperature and branching on the nature and stability of alkene cracking intermediates in h-zsm-5", *J. Catal.*, vol. 345, pp. 53–69, 2017.
- [63] A. Ghorbanpour, J. D. Rimer, and L. C. Grabow, "Computational assessment of the dominant factors governing the mechanism of methanol dehydration over h-zsm-5 with heterogeneous aluminum distribution", *ACS catal.*, vol. 6, no. 4, pp. 2287–2298, 2016.
- [64] R. Y. Brogaard, R. Henry, Y. Schuurman, A. J. Medford, P. G. Moses, P. Beato, S. Svelle, J. K. Nørskov, and U. Olsbye, "Methanol-to-hydrocarbons conversion: The alkene methylation pathway", *J. Catal.*, vol. 314, pp. 159–169, 2014.
- [65] A. Szabo and N. S. Ostlund, *Modern Quantum Chemistry: Introduction to Advanced Electronic Structure Theory*, First. Mineola: Dover Publications, Inc., 1996.
- [66] F. Jensen, *Introduction to Computational Chemistry*. Hoboken, NJ, USA: John Wiley & Sons, Inc., 2006.
- [67] W. Koch and M. C. Holthausen, *A Chemist's Guide to Density Functional Theory*. Weinheim - New York: Wiley - VCH, 2nd edition, 2001.
- [68] J. C. Slater, "Atomic shielding constants", *Phys. Rev.*, vol. 36, pp. 57–64, 1930.
- [69] T. Kato, "On the eigenfunctions of many-particle systems in quantum mechanics", *Commun. Pure Appl. Math.*, vol. 10, no. 2, pp. 151–177, 1957.
- [70] S. F. Boys and A. C. Egerton, "Electronic wave functions - i. a general method of calculation for the stationary states of any molecular system", *Proc. R. Soc. A*, vol. 200, no. 1063, pp. 542–554, 1950.
- [71] J. C. Slater, "The theory of complex spectra", *Phys. Rev.*, vol. 34, pp. 1293–1322, 1929.
- [72] E. U. Condon, "The theory of complex spectra", *Phys. Rev.*, vol. 36, pp. 1121–1133, 1930.
- [73] G. Kresse and J. Furthmüller, "Efficiency of ab-initio total energy calculations for metals and semiconductors using a plane-wave basis set", *Comput. Mater. Sci.*, vol. 6, no. 1, pp. 15–50, 1996.
- [74] G. Kresse and J. Furthmüller, "Efficient iterative schemes for ab initio total-energy calculations using a plane-wave basis set", *Phys. Rev. B*, vol. 54, pp. 11 169–11 186, 1996.

- [75] A. Halkier, T. Helgaker, P. Jørgensen, W. Klopper, and J. Olsen, "Basis-set convergence of the energy in molecular hartree-fock calculations", *Chem. Phys. Lett.*, vol. 302, no. 5, pp. 437–446, 1999.
- [76] V. Vasilyev, "Online complete basis set limit extrapolation calculator", *Comput. Theor. Chem.*, vol. 1115, pp. 1–3, 2017.
- [77] P.-O. Löwdin, "Quantum theory of many-particle systems. iii. extension of the hartree-fock scheme to include degenerate systems and correlation effects", *Phys. Rev.*, vol. 97, pp. 1509–1520, 1955.
- [78] M. N. *, K. R. Shamasundar, and D. Mukherjee, "Reflections on size-extensivity, size-consistency and generalized extensivity in many-body theory", *Mol. Phys.*, vol. 103, no. 15-16, pp. 2277–2298, 2005.
- [79] J. A. Pople, "Quantum chemical models (nobel lecture)", *Angew. Chem. Int. Ed.*, vol. 38, no. 13-14, pp. 1894–1902, 1999.
- [80] T. J. Goncalves, P. N. Plessow, and F. Studt, "On the accuracy of density functional theory in zeolite catalysis", *ChemCatChem*, vol. 11, no. 17, pp. 4368–4376, 2019.
- [81] M. Ernzerhof and G. E. Scuseria, "Assessment of the perdew-burke-ernzerhof exchange-correlation functional", *J. Chem. Phys.*, vol. 110, no. 11, pp. 5029–5036, 1999.
- [82] N. Mardirossian and M. Head-Gordon, "Thirty years of density functional theory in computational chemistry: An overview and extensive assessment of 200 density functionals", *Mol. Phys.*, vol. 115, no. 19, pp. 2315–2372, 2017.
- [83] P. Hohenberg and W. Kohn, "Inhomogeneous electron gas", *Phys. Rev.*, vol. 136, pp. 864–871, 1964.
- [84] W. Kohn and L. J. Sham, "Self-consistent equations including exchange and correlation effects", *Phys. Rev.*, vol. 140, pp. 1133–1138, 1965.
- [85] K. Capelle, "A bird's-eye view of density-functional theory", *Braz. J. Phys.*, vol. 36, pp. 1318–1343, 2006.
- [86] R. van Meer, O. V. Gritsenko, and E. J. Baerends, "Physical meaning of virtual kohn-sham orbitals and orbital energies: An ideal basis for the description of molecular excitations", *J. Chem. Theory Comput.*, vol. 10, no. 10, pp. 4432–4441, 2014.
- [87] S. Hamel, P. Duffy, M. E. Casida, and D. R. Salahub, "Kohn-sham orbitals and orbital energies: Fictitious constructs but good approximations all the same", *J. Electron. Spectros. Relat. Phenomena*, vol. 123, no. 2, pp. 345–363, 2002.
- [88] C. Lee, W. Yang, and R. G. Parr, "Development of the colle-salvetti correlation-energy formula into a functional of the electron density", *Phys. Rev. B*, vol. 37, pp. 785–789, 1988.
- [89] A. D. Becke, "A new mixing of hartree-fock and local density-functional theories", *J. Chem. Phys.*, vol. 98, no. 2, pp. 1372–1377, 1993.
- [90] K. Lejaeghere *et al.*, "Reproducibility in density functional theory calculations of solids", *Science*, vol. 351, no. 6280, 2016.
- [91] R. A. Mata and M. A. Suhm, "Benchmarking quantum chemical methods: Are we heading in the right direction?", *Angew. Chem. Int. Ed.*, vol. 56, no. 37, pp. 11 011–11 018, 2017.
- [92] J. Paier, R. Hirschl, M. Marsman, and G. Kresse, "The perdew-burke-ernzerhof exchange-correlation functional applied to the g2-1 test set using a plane-wave basis set", *J. Chem. Phys.*, vol. 122, no. 23, p. 234 102, 2005.
- [93] J. P. Perdew, K. Burke, and M. Ernzerhof, "Generalized gradient approximation made simple", *Phys. Rev. Lett.*, vol. 77, pp. 3865–3868, 1996.
- [94] J. Perdew, A. Ruzsinszky, G. Csonka, O. Vydrov, G. Scuseria, L. Constantin, X. Zhou, and K. Burke, "Erratum: Restoring the density-gradient expansion for exchange in solids and surfaces (physical review letters (2008) 100 (136406))", *Phys. Rev. Lett.*, vol. 102, no. 3, 2009.
- [95] M. G. Medvedev, I. S. Bushmarinov, J. Sun, J. P. Perdew, and K. A. Lyssenko, "Density functional theory is straying from the path toward the exact functional", *Science*, vol. 355, no. 6320, pp. 49–52, 2017.
- [96] N. Mardirossian and M. Head-Gordon, "Exploring the limit of accuracy for density functionals based on the generalized gradient approximation: Local, global hybrid, and range-separated hybrid functionals with and without dispersion corrections", *J. Chem. Phys.*, vol. 140, no. 18, 18A527, 2014.
- [97] D. Vanderbilt, "Soft self-consistent pseudopotentials in a generalized eigenvalue formalism", *Phys. Rev. B*, vol. 41, pp. 7892–7895, 1990.
- [98] J. C. Slater, "Wave functions in a periodic potential", *Phys. Rev.*, vol. 51, pp. 846–851, 1937.
- [99] P. E. Blöchl, "Projector augmented-wave method", *Phys. Rev. B*, vol. 50, pp. 17 953–17 979, 1994.
- [100] G. Kresse and D. Joubert, "From ultrasoft pseudopotentials to the projector augmented-wave method", *Phys. Rev. B*, vol. 59, pp. 1758–1775, 1999.
- [101] S. Grimme, A. Hansen, J. G. Brandenburg, and C. Bannwarth, "Dispersion-corrected mean-field electronic structure methods", *Chem. Rev.*, vol. 116, no. 9, pp. 5105–5154, 2016.
- [102] J. Wellendorff, K. T. Lundgaard, A. Møgelhøj, V. Petzold, D. D. Landis, J. K. Nørskov, T. Bligaard, and K. W. Jacobsen, "Density functionals for surface science: Exchange-correlation model development with bayesian error estimation", *Phys. Rev. B*, vol. 85, p. 235 149, 2012.
- [103] S. Grimme, J. Antony, S. Ehrlich, and H. Krieg, "A consistent and accurate ab initio parametrization of density functional dispersion correction (dft-d) for the 94 elements h-pu", *J. Chem. Phys.*, vol. 132, no. 15, p. 154 104, 2010.
- [104] J.-D. Chai and M. Head-Gordon, "Long-range corrected hybrid density functionals with damped atom-atom dispersion corrections", *Phys. Chem. Chem. Phys.*, vol. 10, pp. 6615–6620, 2008.
- [105] A. D. Becke and E. R. Johnson, "Exchange-hole dipole moment and the dispersion interaction: High-order dispersion coefficients", *J. Chem. Phys.*, vol. 124, no. 1, p. 014 104, 2006.
- [106] S. Grimme, S. Ehrlich, and L. Goerigk, "Effect of the damping function in dispersion corrected density functional theory", *J. Comput. Chem.*, vol. 32, no. 7, pp. 1456–1465, 2011.
- [107] C. Kelley, "The bfgs method", in *Iterative Methods for Optimization*. 1999, ch. 4.
- [108] S. Goedecker, "Minima hopping: An efficient search method for the global minimum of the potential energy surface of complex molecular systems", *J. Chem. Phys.*, vol. 120, no. 21, pp. 9911–9917, 2004.
- [109] D. Sheppard, P. Xiao, W. Chemelewski, D. D. Johnson, and G. Henkelman, "A generalized solid-state nudged elastic band method", *J. Chem. Phys.*, vol. 136, no. 7, p. 074 103, 2012.
- [110] G. Henkelman and H. Jónsson, "Improved tangent estimate in the nudged elastic band method for finding minimum energy paths and saddle points", *J. Chem. Phys.*, vol. 113, no. 22, pp. 9978–9985, 2000.
- [111] G. Henkelman and H. Jónsson, "A dimer method for finding saddle points on high dimensional potential surfaces using only first derivatives", *J. Chem. Phys.*, vol. 111, no. 15, pp. 7010–7022, 1999.
- [112] P. N. Plessow, "Efficient transition state optimization of periodic structures through automated relaxed potential energy surface scans", *J. Chem. Theory Comput.*, vol. 14, no. 2, pp. 981–990, 2018.
- [113] K. Fukui, "Formulation of the reaction coordinate", *J. Phys. Chem.*, vol. 74, no. 23, pp. 4161–4163, 1970.

- [114] G. Henkelman, B. P. Uberuaga, and H. Jónsson, "A climbing image nudged elastic band method for finding saddle points and minimum energy paths", *J. Chem. Phys.*, vol. 113, no. 22, pp. 9901–9904, 2000.
- [115] V. Magnasco, "Molecular vibrations", in *Elementary Molecular Quantum Mechanics (Second Edition)*, V. Magnasco, Ed., Second Edition, Oxford: Elsevier, 2013, ch. 20, pp. 681–722.
- [116] B. G. Johnson and M. J. Frisch, "Analytic second derivatives of the gradient-corrected density functional energy. effect of quadrature weight derivatives", *Chem. Phys. Lett.*, vol. 216, no. 1, pp. 133–140, 1993.
- [117] D. A. McQuarrie, *Statistical Mechanics*, ser. Harper's Chemistry Series. New York: HarperCollins Publishing, Inc., 1976.
- [118] C. J. Cramer, *Essentials of computational chemistry : theories and models*. West Sussex, England ; New York : J. Wiley, 2002.
- [119] "Entropy contributions to transition state modelling", in *Modelling and Simulation in the Science of Micro- and Meso-Porous Materials*, C. R. A. Catlow, V. V. Speybroeck, and R. A. van Santen, Eds., Elsevier, 2018, ch. 6.
- [120] G. Piccini, M. Alessio, J. Sauer, Y. Zhi, Y. Liu, R. Kolvenbach, A. Jentys, and J. A. Lercher, "Accurate adsorption thermodynamics of small alkanes in zeolites. ab initio theory and experiment for h-chabazite", *J. Phys. Chem C*, vol. 119, no. 11, pp. 6128–6137, 2015.
- [121] J. K. Nørskov, F. Studt, F. Abild-Pedersen, and T. Bligaard, "Heterogeneous catalysis and a sustainable future", in *Fundamental Concepts in Heterogeneous Catalysis*. John Wiley & Sons, Ltd, 2014, ch. 4.
- [122] D. G. Truhlar and B. C. Garrett, "Variational transition state theory", *Annu. Rev. Phys. Chem.*, vol. 35, no. 1, pp. 159–189, 1984.
- [123] I. N. Levine, *Quantum chemistry*, 6th ed. Pearson Prentice Hall, 2009, ch. 11.
- [124] P. Atkins and J. Paula, *Atkins' physical chemistry*. Oxford University press, 2008, ch. 22.
- [125] D. A. McQuarrie and J. D. Simon, *Physical chemistry : a molecular approach*. Sausalito, Calif.: University Science Books, 1997, ch. 26.
- [126] M. Andersen, C. Panosetti, and K. Reuter, "A practical guide to surface kinetic monte carlo simulations", *Front. Chem.*, vol. 7, p. 202, 2019.
- [127] K. Reuter, "First-principles kinetic monte carlo simulations for heterogeneous catalysis: Concepts, status, and frontiers", in *Modeling and Simulation of Heterogeneous Catalytic Reactions*. John Wiley & Sons, Ltd, 2011, ch. 3.
- [128] F. J. Keil, "Molecular modelling for reactor design", *Annu. Rev. Chem. Biomol. Eng.*, vol. 9, no. 1, pp. 201–227, 2018.
- [129] G. Piccini, M. Alessio, and J. Sauer, "Ab initio calculation of rate constants for molecule–surface reactions with chemical accuracy", *Angew. Chem. Int. Ed.*, vol. 55, no. 17, pp. 5235–5237, 2016.
- [130] S. Svelle, C. Tuma, X. Rozanska, T. Kerber, and J. Sauer, "Quantum chemical modeling of zeolite-catalyzed methylation reactions: Toward chemical accuracy for barriers", *J. Am. Chem. Soc.*, vol. 131, no. 2, pp. 816–825, 2009.
- [131] W. Wang, Y. Jiang, and M. Hunger, "Mechanistic investigations of the methanol-to-olefin (mto) process on acidic zeolite catalysts by in situ solid-state nmr spectroscopy", *Catal. Today*, vol. 113, no. 1-2, pp. 102–114, 2006.
- [132] H. Yamazaki, H. Shima, H. Imai, T. Yokoi, T. Tatsumi, and J. Kondo, "Evidence for a "carbene-like" intermediate during the reaction of methoxy species with light alkenes on h-zsm-5", *Angew. Chem. Int. Ed.*, vol. 50, no. 8, pp. 1853–1856, 2011.
- [133] W. Wang, A. Buchholz, M. Seiler, and M. Hunger, "Evidence for an initiation of the methanol-to-olefin process by reactive surface methoxy groups on acidic zeolite catalysts", *J. Am. Chem. Soc.*, vol. 125, no. 49, pp. 15 260–15 267, 2003.
- [134] X. Wu, S. Xu, W. Zhang, J. Huang, J. Li, B. Yu, Y. Wei, and Z. Liu, "Direct mechanism of the first carbon–carbon bond formation in the methanol-to-hydrocarbons process", *Angew. Chem. Int. Ed.*, vol. 56, no. 31, pp. 9039–9043, 2017.
- [135] Z. Wei, Y.-Y. Chen, J. Li, P. Wang, B. Jing, Y. He, M. Dong, H. Jiao, Z. Qin, J. Wang, and W. Fan, "Methane formation mechanism in the initial methanol-to-olefins process catalyzed by sapo-34", *Catal. Sci. Technol.*, vol. 6, no. 14, pp. 5526–5533, 2016.
- [136] S. Blaszowski and R. Van Santen, "Theoretical study of c-c bond formation in the methanol-to- gasoline process", *J. Am. Chem. Soc.*, vol. 119, no. 21, pp. 5020–5027, 1997.
- [137] A. Comas-Vives, M. Valla, C. Copéret, and P. Sautet, "Cooperativity between al sites promotes hydrogen transfer and carbon-carbon bond formation upon dimethyl ether activation on alumina", *ACS Cent. Sci.*, vol. 1, no. 6, pp. 313–319, 2015.
- [138] F. Salehirad and M. Anderson, "Solid-state ¹³c mas nmr study of methanol-to-hydrocarbon chemistry over h-sapo-34", *J. Catal.*, vol. 164, no. 2, pp. 301–314, 1996.
- [139] O. Dewaele, V. Geers, G. Froment, and G. Marin, "The conversion of methanol to olefins: A transient kinetic study", *Chem. Eng. Sci.*, vol. 54, no. 20, pp. 4385–4395, 1999.
- [140] D. Lesthaeghe, V. Van Speybroeck, G. Marin, and M. Waroquier, "Understanding the failure of direct c-c coupling in the zeolite-catalyzed methanol-to-olefin process", *Angew. Chem. Int. Ed.*, vol. 45, no. 11, pp. 1714–1719, 2006.
- [141] X. Chen, M. Neidig, R. Tuinstra, and A. Malek, "Direct observation of acetyl group formation from the reaction of co with methylated h-mor by in situ diffuse reflectance infrared spectroscopy", *J. Phys. Chem. Lett.*, vol. 1, no. 20, pp. 3012–3015, 2010.
- [142] A. Chowdhury, K. Houben, G. Whiting, M. Mokhtar, A. Asiri, S. Al-Thabaiti, S. Basahel, M. Baldus, and B. Weckhuysen, "Initial carbon–carbon bond formation during the early stages of the methanol-to-olefin process proven by zeolite-trapped acetate and methyl acetate", *Angew. Chem. Int. Ed.*, vol. 55, no. 51, pp. 15 840–15 845, 2016.
- [143] D. Wragg, M. O'Brien, F. Bleken, M. Di Michiel, U. Olsbye, and H. Fjellvåg, "Watching the methanol-to-olefin process with time- and space-resolved high-energy operando x-ray diffraction", *Angew. Chem. Int. Ed.*, vol. 51, no. 32, pp. 7956–7959, 2012.
- [144] T. Janssens, S. Svelle, and U. Olsbye, "Kinetic modeling of deactivation profiles in the methanol-to-hydrocarbons (mth) reaction: A combined autocatalytic-hydrocarbon pool approach", *J. Catal.*, vol. 308, pp. 122–130, 2013.
- [145] P. Kumar, J. Thybaut, S. Svelle, U. Olsbye, and G. Marin, "Single-event microkinetics for methanol to olefins on h-zsm-5", *Ind. Eng. Chem. Res.*, vol. 52, no. 4, pp. 1491–1507, 2013.
- [146] N. Hansen, T. Kerber, J. Sauer, A. Bell, and F. Keil, "Quantum chemical modeling of benzene ethylation over h-zsm-5 approaching chemical accuracy: A hybrid mp2:dft study", *J. Am. Chem. Soc.*, vol. 132, no. 33, pp. 11 525–11 538, 2010.
- [147] Y. Liu, S. Müller, D. Berger, J. Jelic, K. Reuter, M. Tonigold, M. Sanchez-Sanchez, and J. Lercher, "Formation mechanism of the first carbon-carbon bond and the first olefin in the methanol conversion into hydrocarbons", *Angew. Chem. Int. Ed.*, vol. 55, no. 19, pp. 5723–5726, 2016.
- [148] A. Bhan, A. Allian, G. Sunley, D. Law, and E. Iglesia, "Specificity of sites within eight-membered ring zeolite channels for carbonylation of methyls to acetyls", *J. Am. Chem. Soc.*, vol. 129, no. 16, pp. 4919–4924, 2007.
- [149] D. Rasmussen, J. Christensen, B. Temel, F. Studt, P. Moses, J. Rossmeis, A. Riisager, and A. Jensen, "Ketene as a reaction intermediate in the carbonylation of dimethyl ether to methyl acetate over mordenite", *Angew. Chem. Int. Ed.*, vol. 54, no. 25, pp. 7261–7264, 2015.
- [150] F. Celik, T. Kim, A. Mlinar, and A. Bell, "An investigation into the mechanism and kinetics of dimethoxymethane carbonylation over fau and mfi zeolites", *J. Catal.*, vol. 274, no. 2, pp. 150–162, 2010.
- [151] F. Jiao, J. Li, X. Pan, J. Xiao, H. Li, H. Ma, M. Wei, Y. Pan, Z. Zhou, M. Li, S. Miao, J. Li, Y. Zhu, D. Xiao, T. He, J. Yang, F. Qi, Q. Fu, and X. Bao, "Selective conversion of syngas to light olefins", *Science*, vol. 351, no. 6277, pp. 1065–1068, 2016.

- [152] J. Buchanan, J. Santiesteban, and W. Haag, "Mechanistic considerations in acid-catalyzed cracking of olefins", *J. Catal.*, vol. 158, no. 1, pp. 279–287, 1996.
- [153] A. Corma and A. Orchillés, "Current views on the mechanism of catalytic cracking", *Microporous Mesoporous Mater.*, vol. 35–36, pp. 21–30, 2000.
- [154] Y. Kissin, "Chemical mechanisms of catalytic cracking over solid acidic catalysts: Alkanes and alkenes", *Catal. Rev.*, vol. 43, no. 1–2, pp. 85–146, 2001.
- [155] A. D. Chowdhury and J. Gascon, "The curious case of ketene in zeolite chemistry and catalysis", *Angew. Chem. Int. Ed.*, vol. 57, no. 46, pp. 14 982–14 985, 2018.
- [156] F. Furche, R. Ahlrichs, C. Hättig, W. Klopper, M. Sierka, and F. Weigend, "Turbomole", *WIREs Wiley Interdiscip. Rev. Comput. Mol. Sci.*, vol. 4, no. 2, pp. 91–100, 2014.
- [157] P. Plessow and F. Studt, "Theoretical insights into the effect of the framework on the initiation mechanism of the mto process", *Catal. Lett.*, vol. 148, no. 4, pp. 1246–1253, 2018.
- [158] S. Wang, Y. Chen, Z. Qin, T.-S. Zhao, S. Fan, M. Dong, J. Li, W. Fan, and J. Wang, "Origin and evolution of the initial hydrocarbon pool intermediates in the transition period for the conversion of methanol to olefins over h-zsm-5 zeolite", *J. Catal.*, vol. 369, pp. 382–395, 2019.
- [159] S. Csicsery, "Shape-selective catalysis in zeolites", *Zeolites*, vol. 4, no. 3, pp. 202–213, 1984.
- [160] S. Reitmeyer, R. Mukti, A. Jentys, and J. Lercher, "Surface transport processes and sticking probability of aromatic molecules in hzsm-5", *J. Phys. Chem. C*, vol. 112, no. 7, pp. 2538–2544, 2008.
- [161] S. Zheng, H. Tanaka, A. Jentys, and J. Lercher, "Novel model explaining toluene diffusion in hzsm-5 after surface modification", *J. Phys. Chem. B*, vol. 108, no. 4, pp. 1337–1343, 2004.
- [162] G. Müller, T. Narbeshuber, G. Mirth, and J. Lercher, "Infrared microscopic study of sorption and diffusion of toluene in zsm-5", *J. Phys. Chem.*, vol. 98, no. 31, pp. 7436–7439, 1994.
- [163] P. Losch, A. Pinar, M. Willinger, K. Soukup, S. Chavan, B. Vincent, P. Pale, and B. Louis, "H-zsm-5 zeolite model crystals: Structure-diffusion-activity relationship in methanol-to-olefins catalysis", *J. Catal.*, vol. 345, pp. 11–23, 2017.
- [164] R. Kolvenbach, N. Al-Yassir, S. Al-Khattaf, O. Gobin, J. Ahn, A. Jentys, and J. Lercher, "A comparative study of diffusion of benzene/p-xylene mixtures in mfi particles, pellets and grown membranes", *Catal. Today*, vol. 168, no. 1, pp. 147–157, 2011.
- [165] A. Ghysels, S. Moors, K. Hemelsoet, K. De Wispelaere, M. Waroquier, G. Sastre, and V. Van Speybroeck, "Shape-selective diffusion of olefins in 8-ring solid acid microporous zeolites", *J. Phys. Chem. C*, vol. 119, no. 41, pp. 23 721–23 734, 2015.
- [166] B. Smit and T. Maesen, "Molecular simulations of zeolites: Adsorption, diffusion, and shape selectivity", *Chem. Rev.*, vol. 108, no. 10, pp. 4125–4184, 2008.
- [167] R. Awati, P. Ravikovitch, and D. Sholl, "Efficient and accurate methods for characterizing effects of framework flexibility on molecular diffusion in zeolites: CH₄ diffusion in eight member ring zeolites", *J. Phys. Chem. C*, vol. 117, no. 26, pp. 13 462–13 473, 2013.
- [168] A. Skoulidas and D. Sholl, "Molecular dynamics simulations of self-diffusivities, corrected diffusivities, and transport diffusivities of light gases in four silica zeolites to assess influences of pore shape and connectivity", *J. Phys. Chem. A*, vol. 107, no. 47, pp. 10 132–10 141, 2003.
- [169] S. Amirjalayer, M. Tafipolsky, and R. Schmid, "Molecular dynamics simulation of benzene diffusion in mof-5: Importance of lattice dynamics", *Angew. Chem. Int. Ed.*, vol. 46, no. 3, pp. 463–466, 2007.
- [170] G. Sastre, C. Catlow, and A. Corma, "Diffusion of benzene and propylene in mcm-22 zeolite. a molecular dynamics study", *J. Phys. Chem. B*, vol. 103, no. 25, pp. 5187–5196, 1999.
- [171] D. Dubbeldam, E. Beerdse, S. Calero, and B. Smit, "Dynamically corrected transition state theory calculations of self-diffusion in anisotropic nanoporous materials", *J. Phys. Chem. B*, vol. 110, no. 7, pp. 3164–3172, 2006.
- [172] P. Cnudde, R. Demuyne, S. Vandenberghe, M. Waroquier, G. Sastre, and V. Speybroeck, "Light olefin diffusion during the mto process on h-sapo-34: A complex interplay of molecular factors", *J. Am. Chem. Soc.*, vol. 142, no. 13, pp. 6007–6017, 2020.
- [173] R. Rowland and R. Taylor, "Intermolecular nonbonded contact distances in organic crystal structures: Comparison with distances expected from van der waals radii", *J. Phys. Chem.*, vol. 100, no. 18, pp. 7384–7391, 1996.
- [174] S. Amirjalayer and R. Schmid, "Mechanism of benzene diffusion in mof-5: A molecular dynamics investigation", *Microporous Mesoporous Mater.*, vol. 125, no. 1–2, pp. 90–96, 2009.
- [175] E. Haldoupis, S. Nair, and D. Sholl, "Efficient calculation of diffusion limitations in metal organic framework materials: A tool for identifying materials for kinetic separations", *J. Am. Chem. Soc.*, vol. 132, no. 21, pp. 7528–7539, 2010.
- [176] J. Liu, S. Keskin, D. Sholl, and J. Johnson, "Molecular simulations and theoretical predictions for adsorption and diffusion of ch₄/h₂ and co₂/ch₄ mixtures in zifs", *J. Phys. Chem. C*, vol. 115, no. 25, pp. 12 560–12 566, 2011.
- [177] K. Jacobsen *et al.*, "The atomic simulation environment - a python library for working with atoms", *J. Condens.*, vol. 29, no. 27, 2017.
- [178] S. Smidstrup, A. Pedersen, K. Stokbro, and H. Jónsson, "Improved initial guess for minimum energy path calculations", *J. Chem. Phys.*, vol. 140, no. 21, 2014.
- [179] R. Brogaard, P. Moses, and J. Nørskov, "Modeling van der waals interactions in zeolites with periodic dft: Physisorption of n-alkanes in zsm-22", *Catal. Lett.*, vol. 142, no. 9, pp. 1057–1060, 2012.
- [180] R. T. Carr, M. Neurock, and E. Iglesia, "Catalytic consequences of acid strength in the conversion of methanol to dimethyl ether", *J. Catal.*, vol. 278, no. 1, pp. 78–93, 2011.
- [181] A. J. Jones and E. Iglesia, "Kinetic, spectroscopic, and theoretical assessment of associative and dissociative methanol dehydration routes in zeolites", *Angew. Chem. Int. Ed.*, vol. 53, no. 45, pp. 12 177–81, 2014.
- [182] S. R. Blaszowski and R. A. vanSanten, "Theoretical study of the mechanism of surface methoxy and dimethyl ether formation from methanol catalyzed by zeolitic protons", *J. Phys. Chem. B*, vol. 101, no. 13, pp. 2292–2305, 1997.
- [183] A. J. Jones, R. T. Carr, S. I. Zones, and E. Iglesia, "Acid strength and solvation in catalysis by mfi zeolites and effects of the identity, concentration and location of framework heteroatoms", *J. Catal.*, vol. 312, pp. 58–68, 2014.
- [184] M. Migliori, A. Aloise, E. Catizzone, and G. Giordano, "Kinetic analysis of methanol to dimethyl ether reaction over h-mfi catalyst", *Ind. Eng. Chem. Res.*, vol. 53, no. 38, pp. 14 885–14 891, 2014.
- [185] J. R. Di Iorio and R. Gounder, "Controlling the isolation and pairing of aluminum in chabazite zeolites using mixtures of organic and inorganic structure-directing agents", *Chem. Mater.*, vol. 28, no. 7, pp. 2236–2247, 2016.
- [186] X. Tang, Z. Liu, L. Huang, W. Chen, C. Li, G. Wang, G. Li, X. Yi, and A. Zheng, "Violation or abidance of löwenstein's rule in zeolites under synthesis conditions?", *ACS Catal.*, vol. 9, no. 12, pp. 10 618–10 625, 2019.
- [187] R. E. Fletcher, S. Ling, and B. Slater, "Violations of lowenstein's rule in zeolites", *Chem Sci*, vol. 8, no. 11, pp. 7483–7491, 2017.
- [188] S. Bordiga, L. Regli, D. Cocina, C. Lamberti, M. Bjorgen, and K. P. Lillerud, "Assessing the acidity of high silica chabazite h-ssz-13 by ftir using co as molecular probe: Comparison with h-sapo-34", *J. Phys. Chem. B*, vol. 109, no. 7, pp. 2779–2784, 2005.

- [189] C. M. Wang, R. Y. Brogaard, B. M. Weckhuysen, J. K. Nørskov, and F. Studt, "Reactivity descriptor in solid acid catalysis: Predicting turnover frequencies for propene methylation in zeotypes", *J. Phys. Chem. Lett.*, vol. 5, no. 9, pp. 1516–21, 2014.
- [190] S. Sklenak, J. Dedeczek, C. Li, B. Wichterlova, V. Gabova, M. Sierka, and J. Sauer, "Aluminium siting in the zsm-5 framework by combination of high resolution 27al nmr and dft/mm calculations", *Phys. Chem. Chem. Phys.*, vol. 11, no. 8, pp. 1237–47, 2009.
- [191] I. Štich, J. D. Gale, K. Terakura, and M. C. Payne, "Role of the zeolitic environment in catalytic activation of methanol", *J. Am. Chem. Soc.*, vol. 121, no. 14, pp. 3292–3302, 1999.
- [192] V. Van Speybroeck, K. Hemelsoet, L. Joos, M. Waroquier, R. G. Bell, and C. R. Catlow, "Advances in theory and their application within the field of zeolite chemistry", *Chem. Soc. Rev.*, vol. 44, no. 20, pp. 7044–111, 2015.
- [193] V. Van Speybroeck, K. De Wispelaere, J. Van der Mynsbrugge, M. Vandichel, K. Hemelsoet, and M. Waroquier, "First principle chemical kinetics in zeolites: The methanol-to-olefin process as a case study", *Chem. Soc. Rev.*, vol. 43, pp. 7326–7357, 2014.
- [194] F. Studt, "Grand challenges in computational catalysis", *Front. Catal.*, vol. 1, 2021.
- [195] C. T. Nimlos, A. J. Hoffman, Y. G. Hur, B. J. Lee, J. R. Di Iorio, D. D. Hibbitts, and R. Gounder, "Experimental and theoretical assessments of aluminum proximity in mfi zeolites and its alteration by organic and inorganic structure-directing agents", *Chem. Mater.*, vol. 32, no. 21, pp. 9277–9298, 2020.
- [196] S. R. Lonsinger, A. K. Chakraborty, D. N. Theodorou, and A. T. Bell, "The effects of local structural relaxation on aluminum siting within h-zsm-5", *Catal. Lett.*, vol. 11, no. 2, pp. 209–217, 1991.
- [197] A. E. Alvarado-Swaisgood, M. K. Barr, P. J. Hay, and A. Redondo, "Ab initio quantum chemical calculations of aluminum substitution in zeolite zsm-5", *J. Phys. Chem.*, vol. 95, no. 24, pp. 10 031–10 036, 1991.
- [198] M. DeLuca, P. Kravchenko, A. Hoffman, and D. Hibbitts, "Mechanism and kinetics of methylating c6–c12 methylbenzenes with methanol and dimethyl ether in h-mfi zeolites", *ACS catal.*, vol. 9, no. 7, pp. 6444–6460, 2019.
- [199] D. J. Parrillo, C. Lee, and R. J. Gorte, "Heats of adsorption for ammonia and pyridine in h-zsm-5: Evidence for identical brønsted-acid sites", *Appl. Catal. A-gen.*, vol. 110, no. 1, pp. 67–74, 1994.
- [200] Z. Wen, D. Yang, X. He, Y. Li, and X. Zhu, "Methylation of benzene with methanol over hzsm-11 and hzsm-5: A density functional theory study", *J. Mol. Catal. A Chem.*, vol. 424, pp. 351–357, 2016.
- [201] M. N. Mazar, S. Al-Hashimi, A. Bhan, and M. Cococcioni, "Methylation of ethene by surface methoxides: A periodic pbe+d study across zeolites", *J. Phys. Chem C*, vol. 116, no. 36, pp. 19 385–19 395, 2012.
- [202] M. Fečík, P. N. Plessow, and F. Studt, "Simple scheme to predict transition-state energies of dehydration reactions in zeolites with relevance to biomass conversion", *J. Phys. Chem C*, vol. 122, no. 40, pp. 23 062–23 067, 2018.

Appendix

A Modelling the formation of the first olefins in the MTO process

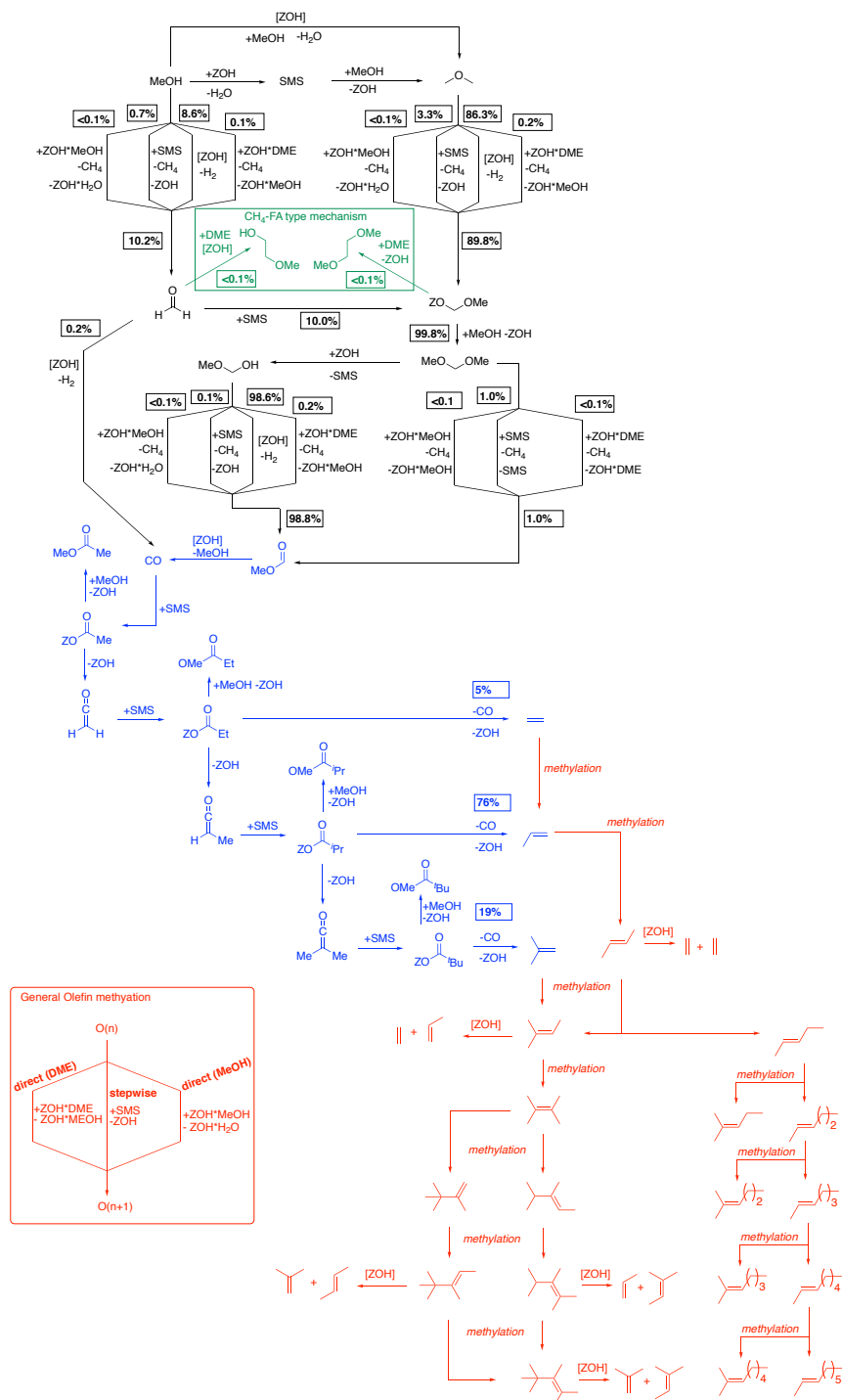
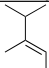
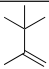
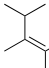
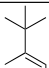
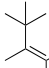
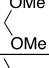
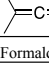


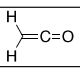
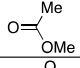
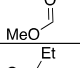
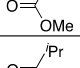
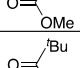
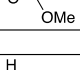
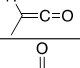
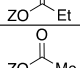
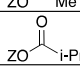
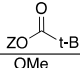
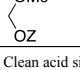
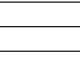
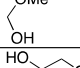
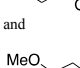
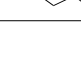
Figure A.1: Overview over the most important elementary reactions considered in this work. For a given olefin carbon-framework only the most stable isomer is shown (for example 1-butene vs. 2-butene). The corresponding isomerisations are omitted. Sensitivity analysis is shown for at $t = 0.3$ s and 400 °C.

Table A.1: List of all elementary reactions. Forward and backwards reactions are labelled i and -i. Activation free energy are in kJ/mol at a reference pressure of 1 bar.

number	reactants	products	ΔG^\ddagger	number	reactants	products	ΔG^\ddagger
1	ZOH*MeOH	ZOMe+H2O	169.30	54	C5a+ZOH*MeOH	C6a+ZOH*H2O	156.57
-1	ZOMe+H2O	ZOH*MeOH	176.90	-54	C6a+ZOH*H2O	C5a+ZOH*MeOH	199.35
2	MeOH+ZOMe	ZOH*DME	150.61	55	C2+ZOH*DME	C3+ZOH*MeOH	215.67
-2	ZOH*DME	MeOH+ZOMe	160.25	-55	C3+ZOH*MeOH	C2+ZOH*DME	275.85
3	ZOH*H2O	ZOCOMe+H2	219.73	56	C3+ZOH*DME	C4a+ZOH*MeOH	208.36
-3	ZOCOMe+H2	ZOH*DME	153.08	-56	C4a+ZOH*MeOH	C3+ZOH*DME	257.87
4	MF+ZOH	ZOH*MeOH+CO	134.65	57	C4a+ZOH*DME	C5a+ZOH*MeOH	195.16
-4	ZOH*MeOH+CO	MF+ZOH	178.30	-57	C5a+ZOH*MeOH	C4a+ZOH*DME	246.62
5	ZOCOMe+MeOH	DMM+ZOH	119.14	58	C5a+ZOH*DME	C6a+ZOH*MeOH	164.56
-5	DMM+ZOH	ZOCOMe+MeOH	120.56	-58	C6a+ZOH*MeOH	C5a+ZOH*DME	215.38
6	DMM+ZOH	hacetal+ZOMe	144.73	59	C6a+ZOH*DME	C7b+ZOH*MeOH	173.17
-6	hacetal+ZOMe	DMM+ZOH	136.98	-59	C7b+ZOH*MeOH	C6a+ZOH*DME	192.26
7	hacetal+ZOH	MF+H2+ZOH	180.85	60	C7b+ZOH*DME	C8b+ZOH*MeOH	165.01
-7	MF+H2+ZOH	hacetal+ZOH	248.55	-60	C8b+ZOH*MeOH	C7b+ZOH*DME	209.51
8	CO+ZOMe	ZO2CMe	189.77	61	C4a+ZOH*MeOH	C5b+ZOH*H2O	200.43
-8	ZO2CMe	CO+ZOMe	177.22	-61	C5b+ZOH*H2O	C4a+ZOH*MeOH	231.71
9	ZO2CMe+MeOH	MA+ZOH	96.95	62	C4a+ZOH*DME	C5b+ZOH*MeOH	207.18
-9	MA+ZOH	ZO2CMe+MeOH	149.78	-62	C5b+ZOH*MeOH	C4a+ZOH*DME	246.50
10	ZO2CMe	Ketene+ZOH	80.00	63	C5b+ZOH*MeOH	C6b+ZOH*H2O	186.87
-10	Ketene+ZOH	ZO2CMe	80.66	-63	C6b+ZOH*H2O	C5b+ZOH*MeOH	215.75
11	Ketene+ZOMe	ZO2CEt	159.14	64	C5b+ZOH*DME	C6b+ZOH*MeOH	207.91
-11	ZO2CEt	Ketene+ZOMe	203.49	-64	C6b+ZOH*MeOH	C5b+ZOH*DME	244.84
12	ZO2CEt+MeOH	MeO2CEt+ZOH	81.37	65	C5b+ZOH*MeOH	C6c+ZOH*H2O	176.18
-12	MeO2CEt+ZOH	ZO2CEt+MeOH	133.81	-65	C6c+ZOH*H2O	C5b+ZOH*MeOH	218.67
13	ZO2CEt	Mketene+ZOH	80.00	66	C5b+ZOH*DME	C6c+ZOH*MeOH	183.15
-13	Mketene+ZOH	ZO2CEt	81.71	-66	C6c+ZOH*MeOH	C5b+ZOH*DME	233.67
14	Mketene+ZOMe	ZO2CiPr	139.36	67	C6b+ZOH*MeOH	C7c+ZOH*H2O	194.40
-14	ZO2CiPr	Mketene+ZOMe	192.41	-67	C7c+ZOH*H2O	C6b+ZOH*MeOH	227.40
15	ZO2CiPr+MeOH	MeO2CiPr+ZOH	83.09	68	C6b+ZOH*DME	C7c+ZOH*MeOH	194.09
-15	MeO2CiPr+ZOH	ZO2CiPr+MeOH	131.83	-68	C7c+ZOH*MeOH	C6b+ZOH*DME	235.13
16	ZO2CiPr	ZOH+CO+C3	130.46	69	C7c+ZOH*MeOH	C8c+ZOH*H2O	201.45
-16	ZOH+CO+C3	ZO2CiPr	215.14	-69	C8c+ZOH*H2O	C7c+ZOH*MeOH	228.81
17	ZOH*MeOH	ZOH+H2+FA	225.85	70	C6b+ZOH*MeOH	C7d+ZOH*H2O	172.97
-17	ZOH+H2+FA	ZOH*MeOH	206.29	-70	C7d+ZOH*H2O	C6b+ZOH*MeOH	212.87
18	FA+ZOMe	ZOCOMe	173.11	71	C6b+ZOH*DME	C7d+ZOH*MeOH	190.44
-18	ZOCOMe	FA+ZOMe	137.40	-71	C7d+ZOH*MeOH	C6b+ZOH*DME	238.37
19	ZOH+MeOH	ZOH*MeOH	81.74	72	C7c+ZOH*MeOH	C8d+ZOH*H2O	198.41
-19	ZOH*MeOH	ZOH+MeOH	80.00	-72	C8d+ZOH*H2O	C7c+ZOH*MeOH	237.64
20	ZOH+DME	ZOH*DME	80.00	73	C7c+ZOH*DME	C8d+ZOH*MeOH	186.88
-20	ZOH*DME	ZOH+DME	81.20	-73	C8d+ZOH*MeOH	C7c+ZOH*DME	234.16
21	ZOH+H2O	ZOH*H2O	119.12	74	C8a+ZOMe	C8a+ZOH	115.49
-21	ZOH*H2O	ZOH+H2O	80.00	-74	C8a+ZOH	C8a+ZOMe	168.96
22	ZOMe+MeOH	ZOH+CH4+FA	237.36	75	C8a+ZOMe	C9a+ZOH	129.89
-22	ZOH+CH4+FA	ZOMe+MeOH	345.19	-75	C9a+ZOH	C8a+ZOMe	155.59
23	ZOMe+DMM	ZOMe+CH4+MF	205.35	76	C5a+ZOH	C3+C2+ZOH	211.49
-23	ZOMe+CH4+MF	ZOMe+DMM	394.43	-76	C3+C2+ZOH	C5a+ZOH	184.96
24	ZOMe+hacetal	ZOH+CH4+MF	215.05	77	C8a+ZOH	C3+C5a+ZOH	168.11
-24	ZOH+CH4+MF	ZOMe+hacetal	411.88	-77	C3+C5a+ZOH	C8a+ZOH	183.10
25	ZOMe+DME	ZOCOMe+CH4	232.28	78	C9a+ZOH	C4b+C5a+ZOH	86.76
-25	ZOCOMe+CH4	ZOMe+DME	295.96	-78	C4b+C5a+ZOH	C9a+ZOH	144.60
26	ZOH*DME+DME	ZOCOMe+CH4+MeOH	244.72	79	C7a+ZOH	C3+C4a+ZOH	186.87
-26	ZOCOMe+CH4+MeOH	ZOH*DME+DME	298.76	-79	C7a+ZOH	C7a+ZOH	190.78
27	ZOH*MeOH+DME	ZOCOMe+CH4+H2O	260.29	80	C3+C4a+ZOH	C2+C5a+ZOH	179.25
-27	ZOCOMe+CH4+H2O	ZOH*MeOH+DME	331.57	-80	C7a+ZOH	C7a+ZOH	174.43
28	ZOH*DME+DMM	ZOMe+CH4+MF+MeOH	234.89	81	C2+C5a+ZOH	C7b+ZOH	129.86
-28	ZOMe+CH4+MF+MeOH	ZOH*DME+DMM	414.33	-81	C7b+ZOH	C6a+ZOMe	162.06
29	ZOH*MeOH+DMM	ZOMe+CH4+MF+H2O	254.99	82	C7b+ZOMe	C8b+ZOH	109.95
-29	ZOMe+CH4+MF+H2O	ZOH*MeOH+DMM	451.67	-82	C8b+ZOH	C7b+ZOMe	167.56
30	ZOH*DME+hacetal	ZOH*MeOH+CH4+MF	208.33	83	C8b+ZOMe	C9a+ZOH	129.21
-30	ZOH*MeOH+CH4+MF	ZOH*DME+hacetal	393.79	-83	C9a+ZOH	C8b+ZOMe	160.12
31	ZOH*MeOH+hacetal	ZOH*H2O+CH4+MF	247.56	84	C8b+ZOH	C4b+C4a+ZOH	111.15
-31	ZOH*H2O+CH4+MF	ZOH*MeOH+hacetal	422.87	-84	C4b+C4a+ZOH	C8b+ZOH	135.34
32	ZOH*MeOH+DME	ZOH*MeOH+CH4+FA	228.16	85	C4a+ZOMe	C5b+ZOH	171.07
-32	ZOH*MeOH+CH4+FA	ZOH*MeOH+DME	327.55	-85	C5b+ZOH	C4a+ZOMe	223.49
33	ZOH*MeOH+MeOH	ZOH*H2O+CH4+FA	274.55	86	C5b+ZOMe	C6c+ZOH	149.22
-33	ZOH*H2O+CH4+FA	ZOH*MeOH+MeOH	360.86	-86	C6c+ZOH	C5b+ZOMe	212.84
34	ZOH*MeOH+MeOH	ZOH*DME+H2O	192.44	87	C5b+ZOMe	C6b+ZOH	159.18
-34	ZOH*DME+H2O	ZOH*MeOH+MeOH	209.68	-87	C6b+ZOH	C5b+ZOMe	209.20
35	FA+ZOH	ZOH+CO+H2	251.14	88	C6b+ZOMe	C7c+ZOH	146.30
-35	ZOH+CO+H2	FA+ZOH	322.17	-88	C7c+ZOH	C6b+ZOMe	200.44
36	FA+ZOH*DME	s.ch4-fa+ZOH	273.67	89	C7c+ZOMe	C8c+ZOH	173.57
-36	s.ch4-fa+ZOH	FA+ZOH*DME	455.73	-89	C8c+ZOH	C7c+ZOMe	222.07
37	DME+ZOCOMe	s.ch4-fa+ZOH	244.33	90	C8c+ZOMe	C9b+ZOH	170.89
-37	s.ch4-fa+ZOH	DME+ZOCOMe	452.24	-90	C9b+ZOH	C8c+ZOMe	219.60
38	ZO2CEt	ZOH+CO+C2	172.47	91	C6b+ZOMe	C7d+ZOH	141.27
-38	ZOH+CO+C2	ZO2CEt	239.31	-91	C7d+ZOH	C6b+ZOMe	202.30
39	ZO2CiPr	Dketene+ZOH	80.00	92	C7c+ZOMe	C8d+ZOH	153.97
-39	Dketene+ZOH	ZO2CiPr	82.12	-92	C8d+ZOH	C7c+ZOMe	214.34
40	Dketene+ZOMe	ZO2CtBu	135.68	93	C8c+ZOMe	C9c+ZOH	142.23
-40	ZO2CtBu	Dketene+ZOMe	117.42	-93	C9c+ZOH	C8c+ZOMe	208.09
41	ZO2CtBu+MeOH	MeO2CtBu+ZOH	83.09	94	C4a+ZOH	ZOH+C2+C2	245.73
-41	MeO2CtBu+ZOH	ZO2CtBu+MeOH	203.42	-94	ZOH+C2+C2	C4a+ZOH	210.48
42	ZO2CtBu	ZOH+CO+C4b	9.97	95	C5b+ZOH	ZOH+C3+C2	238.16
-42	ZOH+CO+C4b	ZO2CtBu	178.68	-95	ZOH+C3+C2	C5b+ZOH	232.76
43	C4b+ZOMe	C5a+ZOH	147.03	96	C6c+ZOH	ZOH+C4b+C2	186.32
-43	C5a+ZOH	C4b+ZOMe	205.64	-96	ZOH+C4b+C2	C6c+ZOH	176.85
44	C2+ZOMe	C3+ZOH	176.46	97	C6c+ZOH	ZOH+C3+C3	199.15
-44	C3+ZOH	C2+ZOMe	249.74	-97	ZOH+C3+C3	C6c+ZOH	194.40
45	C3+ZOMe	C4a+ZOH	155.48	98	C6b+ZOH	ZOH+C4a+C2	211.07
-45	C4a+ZOH	C3+ZOMe	218.09	-98	ZOH+C4a+C2	C6b+ZOH	209.26
46	C4a+ZOMe	C5a+ZOH	153.79	99	C7d+ZOH	ZOH+C3+C4a	209.31
-46	C5a+ZOH	C4a+ZOMe	218.35	-99	ZOH+C3+C4a	C7d+ZOH	219.74
47	C5a+ZOMe	C6a+ZOH	132.43	100	C7d+ZOH	ZOH+C5a+C2	167.51
-47	C6a+ZOH	C5a+ZOMe	196.34	-100	ZOH+C5a+C2	C7d+ZOH	169.22
48	C6a+ZOMe	C7a+ZOH	146.16	101	C7c+ZOH	ZOH+C3+C4a	215.31
-48	C7a+ZOH	C6a+ZOMe	187.70	-101	ZOH+C3+C4a	C7c+ZOH	232.64
49	C2+ZOH*MeOH	C3+ZOH*H2O	208.17	102	C8c+ZOH	ZOH+C5b+C3	200.18
-49	C3+ZOH*H2O	C2+ZOH*MeOH	260.31	-102	ZOH+C5b+C3	C8c+ZOH	221.43
50	C6a+ZOH*MeOH	C7b+ZOH*H2O	139.96	103	C8d+ZOH	ZOH+C5b+C3	235.60
-50	C7b+ZOH*H2O	C6a+ZOH*MeOH	151.02	-103	ZOH+C5b+C3	C8d+ZOH	244.98
51	C7b+ZOH*MeOH	C8b+ZOH*H2O	156.20	104	C9b+ZOH	ZOH+C6b+C3	201.30
-51	C8b+ZOH*H2O	C7b+ZOH*MeOH	192.67	-104	ZOH+C6b+C3	C9b+ZOH	223.87
52	C3+ZOH*MeOH	C4a+ZOH*H2O	194.75	105	C9c+ZOH	ZOH+C6b+C3	232.71
-52	C4a+ZOH*H2O	C3+ZOH*MeOH	236.23	-105	ZOH+C6b+C3	C9c+ZOH	238.13
53	C4a+ZOH*MeOH	C5a+ZOH*H2O	177.96				
-53	C5a+ZOH*H2O	C4a+ZOH*MeOH	221.38				

Table A.2: List and explanation of species abbreviations.

Number	Abbreviation	Details
1	C2	Ethylene
2	C3	Propylene
3	C4a	2-butene
4	C4b	Iso-butene
5	C5a	2-methyl-2-butene
6	C5b	2-pentene
7	C6a	Tetra-methyl-ethylene
8	C6b	2-hexene
9	C6c	2-methyl-2-pentene
10	C7a	
11	C7b	
12	C7c	2-heptene
13	C7d	2-methyl-2-hexene
14	C8a	
15	C8b	
16	C8c	2-octene
17	C8d	2-methyl-2-heptene
18	C9a	
19	C9b	2-nonene
20	C9c	2-methyl-2-octene
21	CH4	
22	CO	
23	DME	Dimethyl ether
24	DMM	
25	Dketene	
26	FA	Formaldehyde
27	H2	

Number	Abbreviation	Details
28	H2O	
29	Ketene	
30	MA	
31	MF	
32	MeO2CEt	
33	MeO2CiPr	
34	MeO2CtBu	
35	MeOH	
36	Mketene	
37	ZO2CEt	
38	ZO2CMe	
39	ZO2CiPr	
40	ZO2CtBu	
41	ZOCOMe	
42	ZOH	Clean acid site
43	ZOH*DME	
44	ZOH*H2O	
45	ZOH*MeOH	
46	ZOMe	SMS
47	hacetal	 and 
48	s ch4-fa	

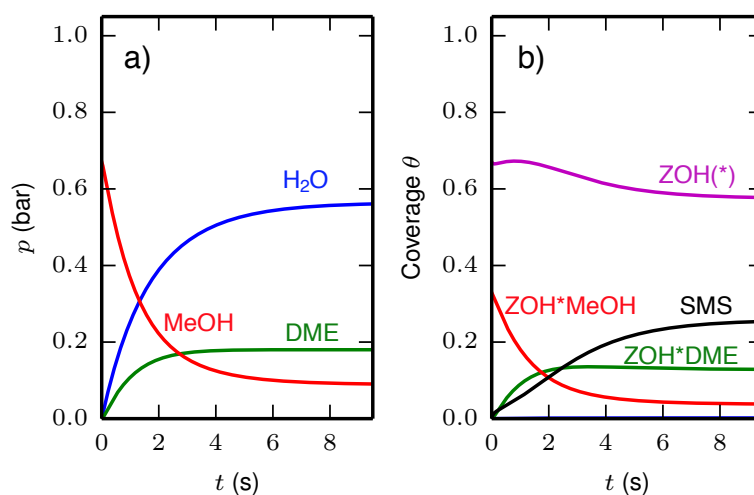


Figure A.2: Kinetics of MeOH/DME-equilibration (at 400 °C) without considering initiation reactions a) partial pressures and b) coverages. The formation of SMS and the adsorption of DME is the reason why partial pressures of water and DME are not identical.

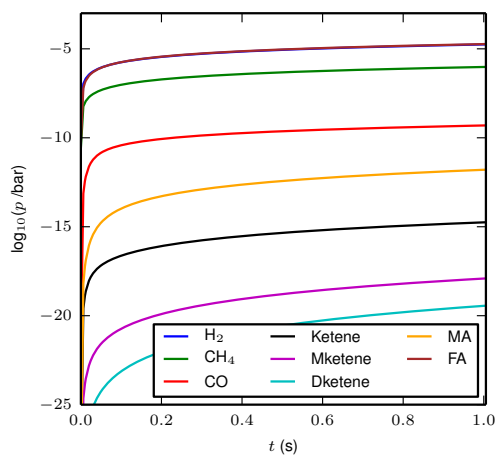


Figure A.3: Partial pressures of selected intermediates (at 400 °C). H₂ and FA have near-identical pressures.

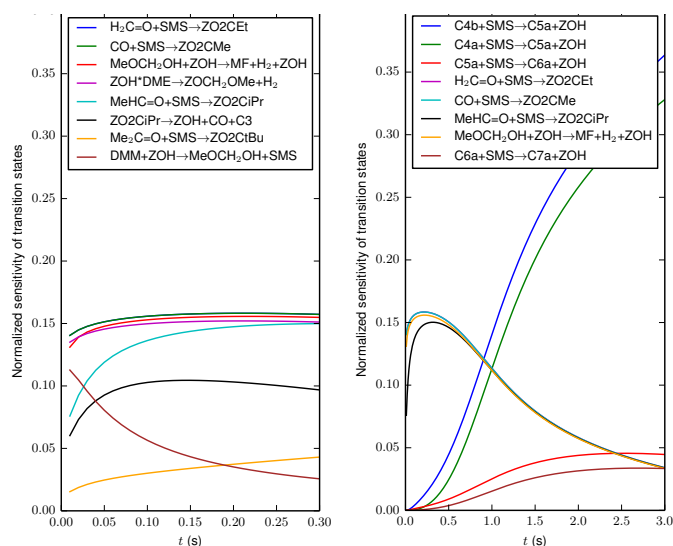


Figure A.4: Normalised sensitivities at 400 °C as a function of time for two different time scales, with the most important reactions plotted in each case.

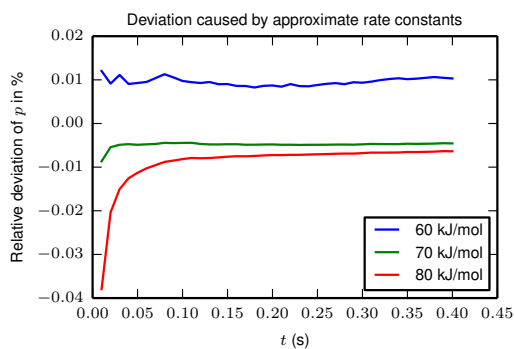


Figure A.5: Relative deviations of $\frac{p - p_{ref}}{p_{ref}}$ of propene obtained at 400 °C relative to the pressures obtained with barriers of 50 kJ/mol.

Table A.3: Sensitivity according to equation 4.1.

reaction number	reactants	products	t = 0.1 s	t = 3 s
			s_i ($\frac{\text{bar}}{\text{K} \cdot \text{mol}}$)	
1	ZOH*MeOH	ZOMe+H2O	-1.96E-23	-4.51E-13
2	MeOH+ZOMe	ZOH*DME	6.20E-25	-3.83E-15
3	ZOH*DME	ZOCOMe+H2	-3.00E-21	-5.35E-12
4	MF+ZOH	ZOH*MeOH+CO	-1.67E-22	-1.35E-13
5	ZOCOMe+MeOH	DMM+ZOH	-2.07E-23	-1.69E-14
6	DMM+ZOH	hacetal+ZOMe	-5.09E-22	-4.35E-13
7	hacetal+ZOH	MF+H2+ZOH	-3.07E-21	-5.49E-12
8	CO+ZOMe	ZO2CMe	-3.12E-21	-5.57E-12
9	ZO2CMe+MeOH	MA+ZOH	1.49E-21	1.51E-12
10	ZO2CMe	Ketene+ZOH	-1.26E-26	-1.10E-17
11	Ketene+ZOMe	ZO2CEt	-3.12E-21	-5.58E-12
12	ZO2CEt+MeOH	MeO2CEt+ZOH	1.45E-22	1.16E-13
13	ZO2CEt	Mketene+ZOH	-5.74E-26	-9.30E-17
14	Mketene+ZOMe	ZO2CiPr	-2.97E-21	-5.52E-12
15	ZO2CiPr+MeOH	MeO2CiPr+ZOH	9.14E-23	6.91E-14
16	ZO2CiPr	ZOH+CO+C3	-1.92E-21	-1.45E-12
17	ZOH*MeOH	ZOH+H2+FA	-2.24E-24	-1.07E-14
18	FA+ZOMe	ZOCOMe	2.89E-21	5.29E-12
19	ZOH+MeOH	ZOH*MeOH	-5.01E-30	-5.72E-20
20	ZOH+DME	ZOH*DME	-1.00E-29	-5.05E-22
21	ZOH+H2O	ZOH*H2O	-4.00E-29	5.05E-22
22	ZOMe+MeOH	ZOH+CH4+FA	-1.72E-25	-7.81E-16
23	ZOMe+DMM	ZOMe+CH4+MF	-3.60E-23	-5.86E-14
24	ZOMe+hacetal	ZOH+CH4+MF	-3.01E-24	-5.39E-15
25	ZOMe+DME	ZOCOMe+CH4	-1.14E-22	-2.03E-13
26	ZOH*DME+DME	ZOCOMe+CH4+MeOH	-6.21E-24	-1.11E-14
27	ZOH*MeOH+DME	ZOCOMe+CH4+H2O	-1.14E-25	-2.04E-16
28	ZOH*DME+DMM	ZOMe+CH4+MF+MeOH	-9.27E-26	-1.51E-16
29	ZOH*MeOH+DMM	ZOMe+CH4+MF+H2O	-7.23E-28	-1.20E-18
30	ZOH*DME+hacetal	ZOH*MeOH+CH4+MF	-5.05E-24	-9.02E-15
31	ZOH*MeOH+hacetal	ZOH*H2O+CH4+MF	-1.34E-27	-2.44E-18
32	ZOH*MeOH+DME	ZOH*MeOH+CH4+FA	-2.65E-25	-1.21E-15
33	ZOH*MeOH+MeOH	ZOH*H2O+CH4+FA	4.30E-29	-1.62E-19
34	ZOH*MeOH+MeOH	ZOH*DME+H2O	-3.25E-26	-6.18E-16
35	FA+ZOH	ZOH+CO+H2	-2.21E-24	-8.85E-15
36	FA+ZOH*DME	s_ch4-fa+ZOH	-7.50E-29	5.00E-24
37	DME+ZOCOMe	s_ch4-fa+ZOH	1.50E-29	5.15E-22
38	ZO2CEt	ZOH+CO+C2	-1.35E-22	-4.98E-16
39	ZO2CiPr	Dketene+ZOH	-3.05E-26	-1.06E-16
40	Dketene+ZOMe	ZO2CtBu	-8.54E-22	-3.20E-12
41	ZO2CtBu+MeOH	MeO2CtBu+ZOH	1.69E-28	6.50E-19
42	ZO2CtBu	ZOH+CO+C4b	3.16E-29	3.35E-17
43	C4b+ZOMe	C5a+ZOH	-3.93E-22	-5.95E-11
44	C2+ZOMe	C3+ZOH	-2.01E-26	-7.55E-16
45	C3+ZOMe	C4a+ZOH	-6.15E-23	-1.52E-12
46	C4a+ZOMe	C5a+ZOH	-1.34E-22	-5.37E-11
47	C5a+ZOMe	C6a+ZOH	-8.85E-23	-7.30E-12
48	C6a+ZOMe	C7a+ZOH	-2.53E-23	-5.47E-12
49	C2+ZOH*MeOH	C3+ZOH*H2O	7.25E-29	-3.30E-19
50	C6a+ZOH*MeOH	C7b+ZOH*H2O	-7.06E-25	2.31E-14
51	C7b+ZOH*MeOH	C8b+ZOH*H2O	-6.82E-29	-4.85E-18
52	C3+ZOH*MeOH	C4a+ZOH*H2O	-8.25E-27	-2.03E-16
53	C4a+ZOH*MeOH	C5a+ZOH*H2O	-2.66E-25	-7.70E-14
54	C5a+ZOH*MeOH	C6a+ZOH*H2O	-1.77E-25	-1.45E-14
55	C2+ZOH*DME	C3+ZOH*MeOH	-1.29E-29	-3.28E-19
56	C3+ZOH*DME	C4a+ZOH*MeOH	-2.44E-27	-6.06E-17
57	C4a+ZOH*DME	C5a+ZOH*MeOH	-4.17E-26	-1.21E-14
58	C5a+ZOH*DME	C6a+ZOH*MeOH	-1.44E-25	-1.18E-14
59	C6a+ZOH*DME	C7b+ZOH*MeOH	-6.28E-27	1.99E-16
60	C7b+ZOH*DME	C8b+ZOH*MeOH	-3.58E-29	-3.43E-18
61	C4a+ZOH*MeOH	C5b+ZOH*H2O	7.21E-28	7.27E-16
62	C4a+ZOH*DME	C5b+ZOH*MeOH	7.91E-28	7.41E-16
63	C5b+ZOH*MeOH	C6b+ZOH*H2O	-1.57E-29	-1.34E-17
64	C5b+ZOH*DME	C6b+ZOH*MeOH	2.47E-29	-1.08E-18
65	C5b+ZOH*MeOH	C6c+ZOH*H2O	-4.93E-30	6.57E-18
66	C5b+ZOH*DME	C6c+ZOH*MeOH	-1.49E-29	6.46E-18
67	C6b+ZOH*MeOH	C7c+ZOH*H2O	-1.47E-32	1.08E-19
68	C6b+ZOH*DME	C7c+ZOH*MeOH	4.95E-30	4.29E-19
69	C7c+ZOH*MeOH	C8c+ZOH*H2O	-1.35E-34	9.14E-25
70	C6b+ZOH*MeOH	C7d+ZOH*H2O	1.03E-29	-2.77E-18
71	C6b+ZOH*DME	C7d+ZOH*MeOH	-7.99E-29	-4.32E-19
72	C7c+ZOH*MeOH	C8d+ZOH*H2O	-2.83E-34	-4.44E-24
73	C7c+ZOH*DME	C8d+ZOH*MeOH	-8.56E-34	-4.57E-22
74	C7a+ZOMe	C8a+ZOH	-3.78E-25	-2.91E-14
75	C8a+ZOMe	C9a+ZOH	-4.64E-24	-3.78E-13
76	C5a+ZOH	C3+C2+ZOH	3.81E-28	2.62E-16
77	C8a+ZOH	C3+C5a+ZOH	1.45E-26	1.08E-14
78	C9a+ZOH	C4b+C5a+ZOH	-1.40E-27	-1.19E-16
79	C7a+ZOH	C3+C4a+ZOH	2.34E-28	6.78E-17
80	C7a+ZOH	C2+C5a+ZOH	2.56E-28	1.38E-16
81	C6a+ZOMe	C7b+ZOH	-2.87E-23	9.11E-13
82	C7b+ZOMe	C8b+ZOH	-1.65E-24	-1.28E-13
83	C8b+ZOMe	C9a+ZOH	-9.40E-24	-1.92E-12
84	C8b+ZOH	C4b+C4a+ZOH	8.51E-24	1.84E-12
85	C4a+ZOMe	C5b+ZOH	8.97E-25	9.36E-13
86	C5b+ZOMe	C6c+ZOH	-1.55E-28	5.46E-15
87	C5b+ZOMe	C6b+ZOH	-5.87E-27	-1.28E-14
88	C6b+ZOMe	C7c+ZOH	1.12E-27	3.63E-15
89	C7c+ZOMe	C8c+ZOH	4.64E-33	-8.62E-22
90	C8c+ZOMe	C9b+ZOH	1.05E-35	-6.45E-23
91	C6b+ZOMe	C7d+ZOH	-3.37E-27	-5.38E-15
92	C7c+ZOMe	C8d+ZOH	-2.49E-32	4.26E-19
93	C8c+ZOMe	C9c+ZOH	-2.43E-33	7.99E-22
94	C4a+ZOH	ZOH+C2+C2	-1.58E-29	3.17E-18
95	C5b+ZOH	ZOH+C3+C2	-1.45E-31	-6.47E-20
96	C6c+ZOH	ZOH+C4b+C2	-1.74E-27	-3.43E-15
97	C6c+ZOH	ZOH+C3+C3	-1.66E-28	-1.17E-16
98	C6b+ZOH	ZOH+C4a+C2	-7.96E-29	-3.81E-19
99	C7d+ZOH	ZOH+C3+C4a	-8.34E-29	-3.05E-18
100	C7d+ZOH	ZOH+C5a+C2	-6.03E-27	-1.30E-14
101	C7c+ZOH	ZOH+C3+C4a	2.04E-31	-3.22E-19
102	C8c+ZOH	ZOH+C5b+C3	5.79E-33	-7.43E-22
103	C8d+ZOH	ZOH+C5b+C3	7.00E-34	-9.50E-22
104	C9b+ZOH	ZOH+C6b+C3	2.71E-35	-5.63E-22
105	C9c+ZOH	ZOH+C6b+C3	1.66E-35	-1.37E-23

B Diffusion limitations in H-SSZ-13 zeolite

B.1 Inclusion of an acid site in the 8-ring

In order to study if the acid site can interact directly with the guest molecule during diffusion a second acid site was placed in the 8-membered ring. Table B.1 compares the transition state energies obtained for this situation with those obtained for a single acid site located so that it doesn't interfere with diffusion.

Table B.1: Stabilisation of the transition state during diffusion via an acid site located in the 8-ring.

Molecule	TS energy (eV)
Isobutene single site	1.19
Isobutene with 2nd site	0.53
Propene single site	-0.12
Propene with 2nd site	-0.56

B.2 Barriers for adsorption/desorption and reorientation in the cavity

To investigate potential energy barriers associated with adsorption/desorption at the acid site potential energy scans were carried out. The scan was performed between the adsorbed structure on the acid site and a state with its orientation and proximity being such that it can travel through the 8-ring.

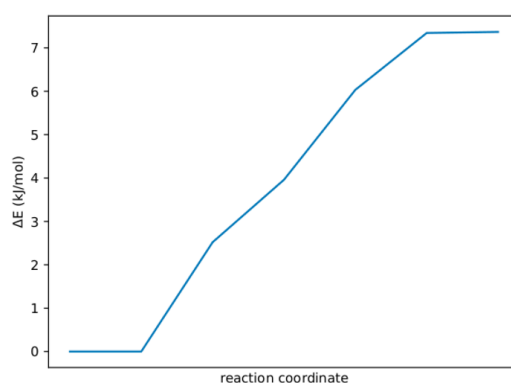


Figure B.1: Potential energy scan from benzene adsorbed on the acid site to benzene with correct position and orientation to diffuse through the 8-ring.

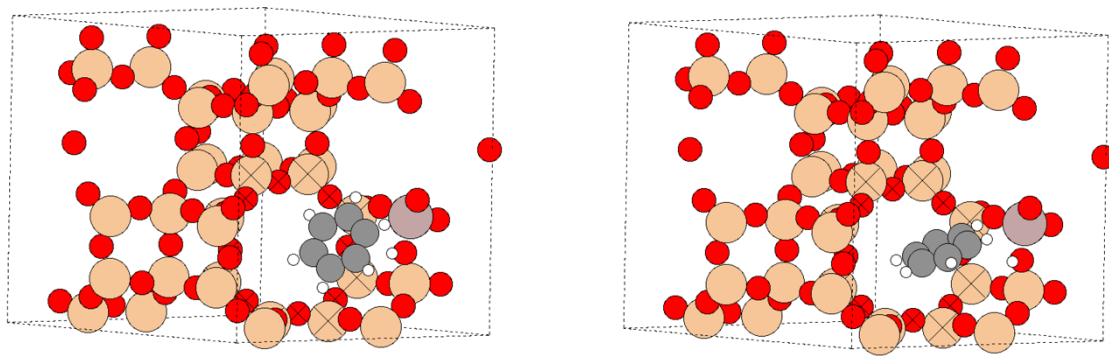


Figure B.2: (left) shows adsorbed benzene satisfying the distance criteria of the C-H distance being smaller than 2.4 Angstrom (right) the state before travelling through the 8-ring. The ring is indicated via cross marks.

B.3 Barriers for alkoxide formation and desorption

Table B.2: Barriers for desorption from an alkoxide. Values are listed relative to the gas phase.

Molecule	Barrier (eV)
Ethene	1.24
Propene	1.31
Cyclobutene	0.79

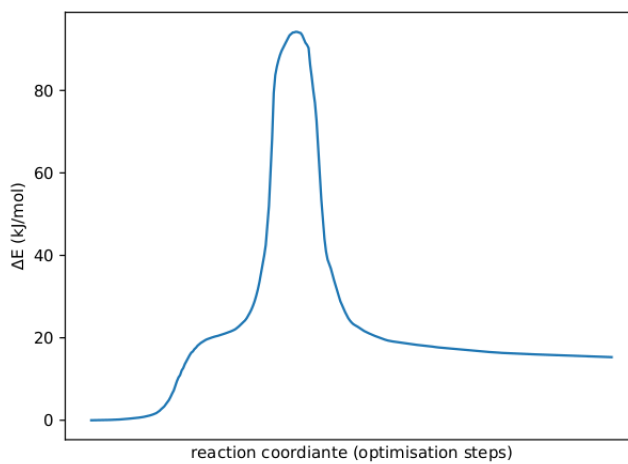


Figure B.3: Reaction path for alkoxide desorption to ethene.

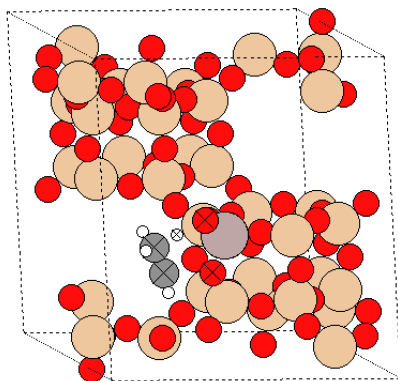


Figure B.4: Illustration of the desorption of ethene from an alkoxide to a free olefin. Atoms involved in bond making and breaking are highlighted with a cross.

B.4 Full data set for guest molecules in the cavity

Table B.3: The most stable structure for each class of adsorption geometry within the zeolite. A cross marks states that do not form or could not be found. Total energies are given in eV.

Molecule	vdW-complex	π -complex	Alkoxide
Ethene	-894.96	-895.25	-895.57
Propene	-911.92	-912.15	-912.25
Trans-2-butene	-928.73	-928.97	928.82
Cyclobutene	-919.87	-920.01	-920.18
Cis-2-butene	-928.67	-928.82	-928.62
Isobutene	-928.71	-929.01	-928.84
Isobutane	-937.12	X	X
Methanol	-894.03	X	X
Benzene	-939.50	-939.61	X
P-Xylene	-973.05	X	X
Tetra-methyl-ethylene	-962.16	X	-961.99
Durene	-1006.73	X	X

In most cases formation of a π -complex was possible on the protonated oxygen shown in Figure B.2. For trans-2-butene however steric hinderance leads to a more stable π -complex forming on a different oxygen. Table B.4 shows the most stable π -complexes found at each accessible oxygen of the acid site.

Table B.4: The most stable π -complexes found at each accessible oxygen of the acid site for trans-2-butene. The oxygen labelling is ordered via their clean sites stability.

Oxygen	Energy (eV)
O1	-928.81
O2	-928.86
O3	-928.97

B.5 Distortion energy of the ring and separate plots of the PBE and D3 contributions

Figure B.5 shows both the distortion energy, which is defined as the energy of the distorted zeolite plus distorted molecule minus undistorted molecule and zeolite and the split up PBE and D3 contributions.

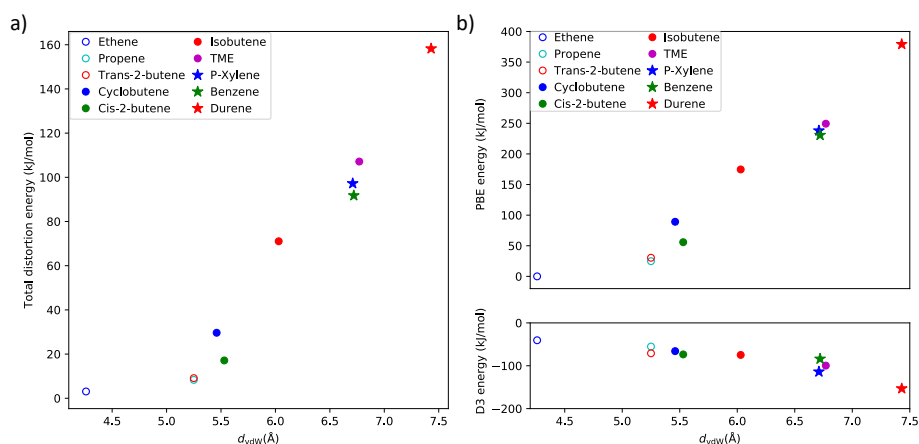


Figure B.5: (left) distortion energy plotted against d_{vdW} . (right) PBE and D3 contributions to the PBE-D3 energy. The PBE contribution is referenced relative to ethene.

B.6 Comparison between the PBE-D3 and the BEEF functionals

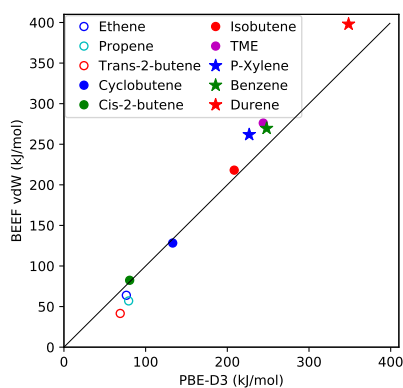


Figure B.6: Single point energy comparison for the PBE-D3 and BEEF functionals.

B.7 Choice of dispersion correction

The D3-correction can be applied with the zero-damping function (as used in the main text) or Becke-Johnson (BJ) damping. The effect of BJ-damping is tested through single-point energy calculations. Differences for barriers are shown in Figure B.7 and are on the order of 10 kJ/mol. There is no systematic trend in terms of which damping function yields larger or smaller barriers.

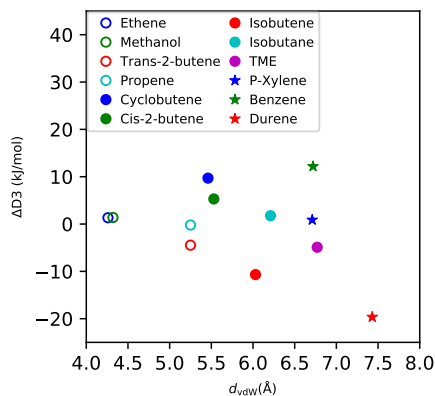


Figure B.7: Differences in D3-dispersion correction: Becke-Johnson damping minus zero-damping.

B.8 Investigation of lateral interactions

To see if lateral interactions play a significant role calculations were done for a 2 by 2 super cell containing one benzene molecule i.e. with the standard single cell calculation having 100% occupation and the super cell calculation has 25 percent occupation (Figure B.8).

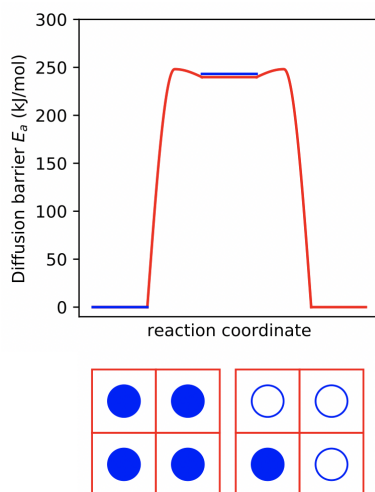


Figure B.8: The energy profile for benzene is shown in red using the normal regime of one benzene per unit cell depicted in the lower left corner i.e. 100 percent benzene occupation. In the right-hand corner the regime for a 2 by 2 supercell with 25 percent occupation is shown. The blue lines show the energy of the minima and intermediate in the 2 by 2 super cell system.

C Trends in reactivity due to proximate acid sites in H-SSZ-13

C.1 Oxygen labels

The oxygens were labelled via their stability in the single site per unit cell regime as calculated with the PBE-D3 functional i.e. the most stable oxygen location is O1 and the next most stable is O2. One of the locations is difficult to access and is labelled OX.

Table C.1: Comparison of oxygen labels used in this work to crystallographic labels.

Oxygen labels used in this work	Crystallographic labels
O1	O4
OX	O1
O3	O2
O2	O3

C.2 All possible clean sites energies for two Al per unit cell in H-SSZ-13

All possible combinations of Al location and H location were calculated. The second Al can be placed in 35 different locations in the unit cell. For each choice of two alumina the protons can arrange in 16 different ways when the sitting of the proton on the oxygen neighbours of the alumina is considered. Thus, in total there are 560 different structures. The resulting structures are shown against the Al-Al distance below.

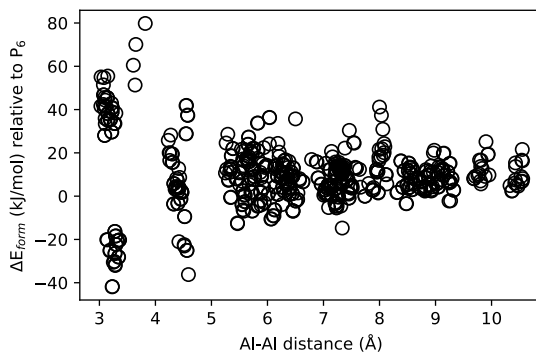


Figure C.1: Formation energy of Al-pairs with two Al-atoms per unit cell (defined in equation 6.1 of the main text) as a function of the spatial distance of the two Al nuclei.

Figure C.2 shows all 16 combinations of the protons of a given Al configuration for the 10 points studied. In general, the acid sites cannot be combined by taking the two most stable configurations from the single site case. If they did combine additively the leftmost columns in Figure C.2 would contain the most stable state and it would be black.

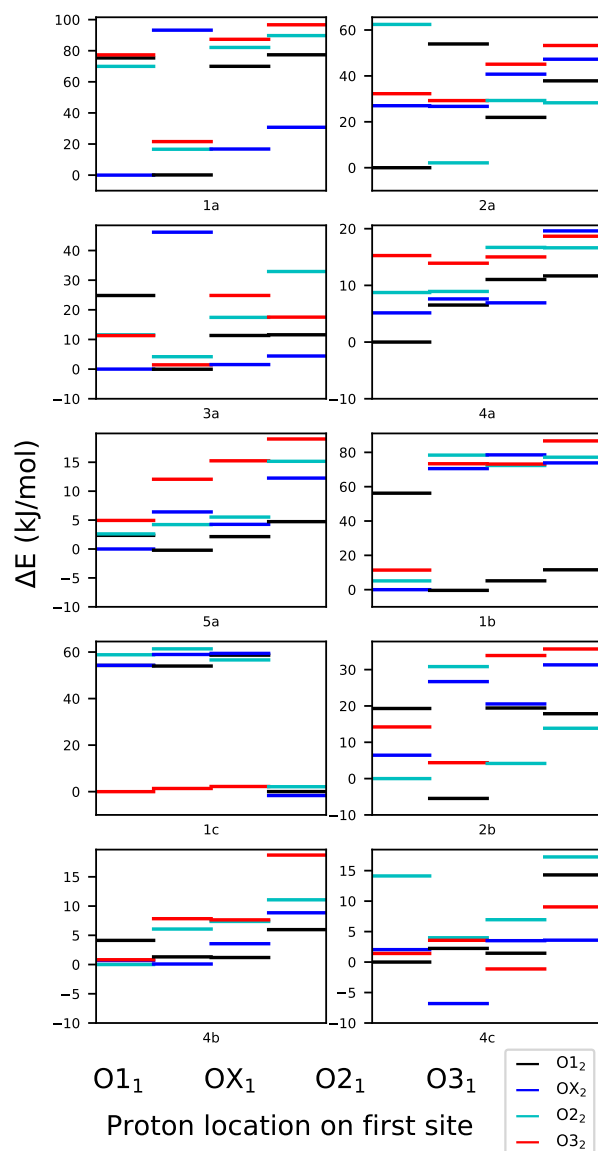


Figure C.2: All possible combinations of proton positions for a given Al distribution. The subscript labels the acid site.

Ammonia was adsorbed at $O1$ of the first acid site (the oxygen which can be expected to give the lowest barrier heights for a given reaction) with the proton of the second site chosen to be in its most stable position at the second site given there is a proton at $O1$ of the first site (the proton acts as a proxy for the transition state or adsorbate in the clean sites calculations). This was done because ammonia is known to correlate well with acidity. The ammonia adsorption energies for all 35 different motifs are shown in Figure C.3. In addition to achieving a good range of possible ammonia binding energies, the points were also chosen to give a good range of neighbour numbers and stabilities. In further calculations no additional assumptions were made about the locations of the protons, this simple computational screening only provided the Al locations.

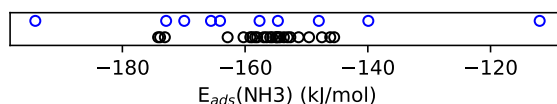


Figure C.3: Ammonia adsorption energies at O1 of the first site for all possible motifs with two acid sites per cell. The proton of the second site is chosen to be in the most stable position possible. The offset blue points indicate motifs which were studied in more detail in the main text.

C.3 Variational approach for choosing the proton sitting

For the 10 Al combinations used throughout adsorption and transition state energies were found at a given oxygen of the first site with the position of the proton on the second site allowed to vary i.e. all four sittings of the proton on the second site are explicitly calculated with the most stable configuration always being taken to be representative of the true reaction barrier. This is demonstrated in Figure C.4.

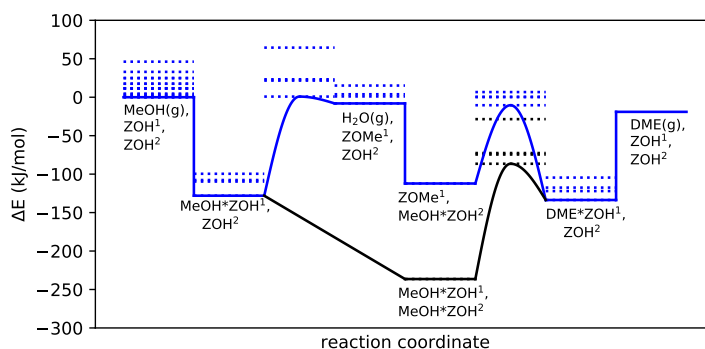


Figure C.4: Reaction coordinate against energy for state 3a in the case where the second site is not occupied by an adsorbate. The acid sites are labelled with superscripts. The different sitting of the proton on the second site are shown with dotted lines. The most stable reaction path which is found variationally is shown with a solid line.

C.4 Outline of scanning procedures

A given adsorption or TS event can take place with the reactant having many different orientations. For all reaction types in this work transition state and adsorption structures were systematically reoriented to find reasonably stable structures. In many cases this means the structures were rotated along the two angles around which the structure can move and also twisted in a screw like fashion to see if additional stabilisation could be achieved. For all methanol adsorptions the adsorbate was automatically twisted through angles of 0, -90, 90 and 180 degrees around the O-H vector of the acid site as well as bridged in both directions across the 6dr ring. Methanol adsorptions across 2 acid sites were briefly explored in test calculations and found to give unfavourable energies. The main criteria which affect the TS energy are the number of hydrogen bonds, the strength of the acid site oxygen and the confinement effects of the framework. Figure C.5 and Table C.2 present the transition state energies for SMS formation at each of the 3 different oxygens considered. The results show framework is able to significantly stabilise the transition state, by as much as 50 kJ/mol in some cases.

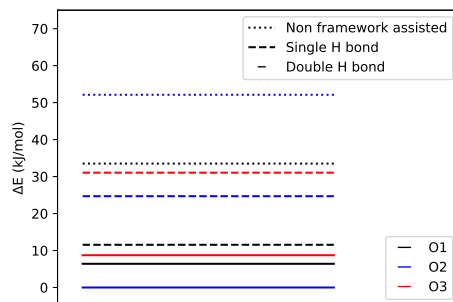


Figure C.5: Different isomers for SMS formation. The structures are categorised by the number of hydrogen bonds they form with the framework.

Table C.2: Raw energies used in Figure C.5. X denotes transition states that could be found.

	Double H bond	Single H bond	Non-framework assisted
O1	-892.61	-892.55	-892.33
O2	-892.67	-892.41	-892.14
O3	-892.58	-892.35	X

C.5 Correlations with ammonia including trend lines

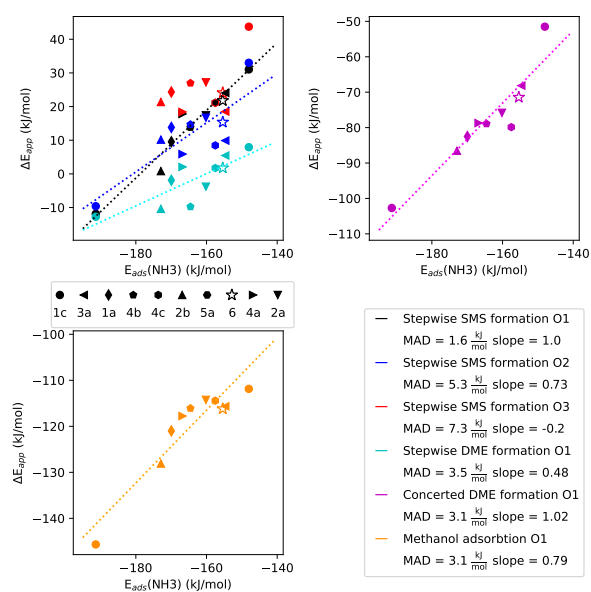


Figure C.6: Correlations of the reaction barriers studied in the main text with ammonia adsorption.

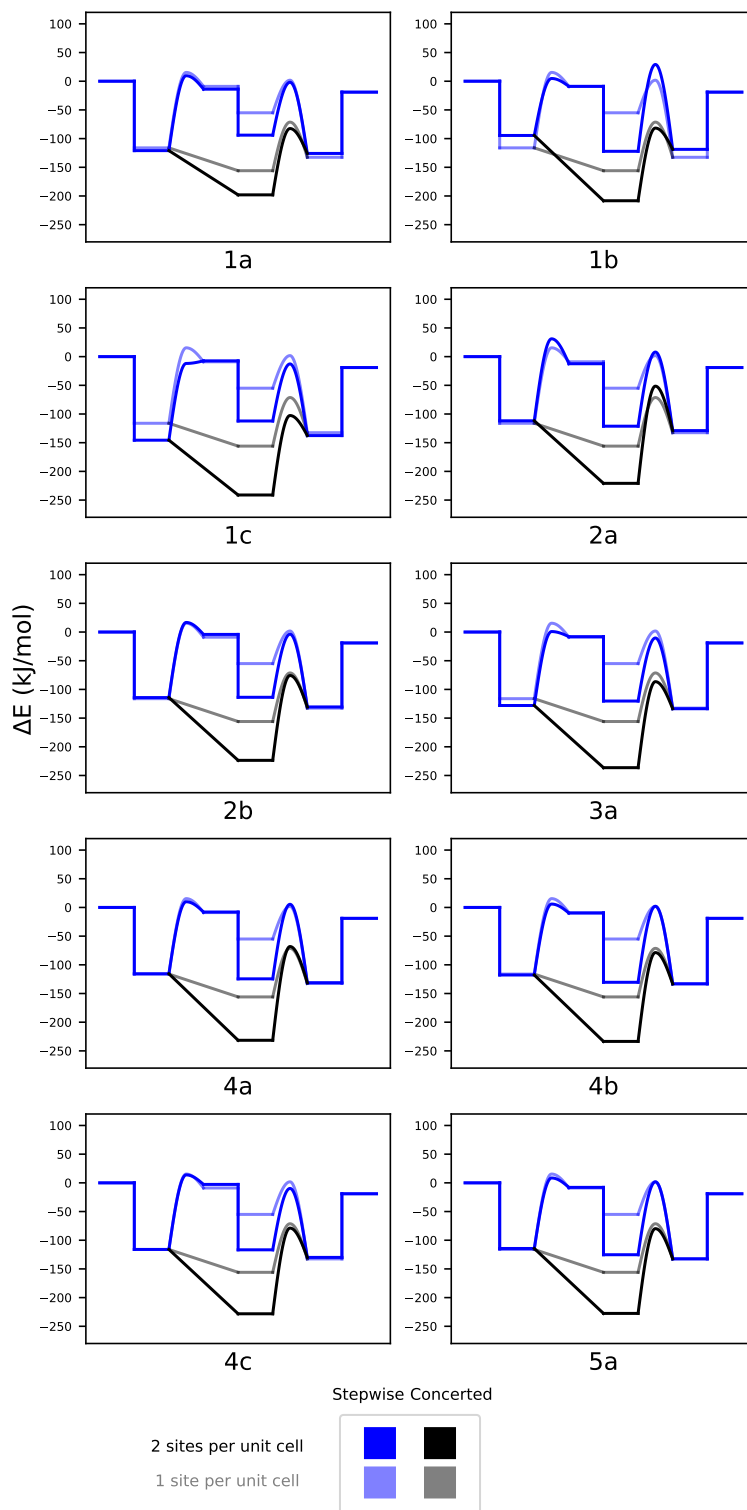


Figure C.7: Full energy profiles for the 10 Al combinations considered. See main text for reaction coordinate labels.

Table C.3: Computed total energies according to the nomenclature introduced in the main text.

State	Energy (eV)	State	Energy (eV)
TS_dme_formation_concerted_1a	-926.072	MIN_methanol_adsorption_on_2nd_site_1a	-895.832
TS_dme_formation_concerted_1b	-925.961	MIN_methanol_adsorption_on_2nd_site_1b	-896.076
TS_dme_formation_concerted_1c	-926.091	MIN_methanol_adsorption_on_2nd_site_1c	-895.765
TS_dme_formation_concerted_2a	-925.576	MIN_methanol_adsorption_on_2nd_site_2a	-895.957
TS_dme_formation_concerted_2b	-925.697	MIN_methanol_adsorption_on_2nd_site_2b	-895.765
TS_dme_formation_concerted_3a	-925.789	MIN_methanol_adsorption_on_2nd_site_3a	-895.763
TS_dme_formation_concerted_4a	-925.525	MIN_methanol_adsorption_on_2nd_site_4a	-895.78
TS_dme_formation_concerted_4b	-925.573	MIN_methanol_adsorption_on_2nd_site_4b	-895.794
TS_dme_formation_concerted_4c	-925.655	MIN_methanol_adsorption_on_2nd_site_4c	-895.824
TS_dme_formation_concerted_5a	-925.586	MIN_methanol_adsorption_on_2nd_site_5a	-895.715
TS_dme_formation_concerted_6	-923.808	MIN_methanol_coadsorbed_1a	-927.116
TS_dme_formation_stepwise_O1_1a	-911.013	MIN_methanol_coadsorbed_1b	-925.946
TS_dme_formation_stepwise_O1_1b	-910.588	MIN_methanol_coadsorbed_1c	-927.001
TS_dme_formation_stepwise_O1_1c	-910.935	MIN_methanol_coadsorbed_2a	-926.554
TS_dme_formation_stepwise_O1_2a	-910.737	MIN_methanol_coadsorbed_2b	-926.614
TS_dme_formation_stepwise_O1_2b	-910.726	MIN_methanol_coadsorbed_3a	-926.75
TS_dme_formation_stepwise_O1_3a	-910.776	MIN_methanol_coadsorbed_4a	-926.444
TS_dme_formation_stepwise_O1_4a	-910.538	MIN_methanol_coadsorbed_4b	-926.447
TS_dme_formation_stepwise_O1_4b	-910.512	MIN_methanol_coadsorbed_4c	-926.688
TS_dme_formation_stepwise_O1_4c	-910.715	MIN_methanol_coadsorbed_5a	-926.46
TS_dme_formation_stepwise_O1_5a	-910.516	MIN_methanol_coadsorbed_6	-924.684
TS_dme_formation_stepwise_O1_6	-908.826	MIN_silicate_6	-860.887
TS_sms_formation_stepwise_O1_1a	-894.885	MIN_surface_methoxy_species_O1_1a	-880.904
TS_sms_formation_stepwise_O1_1b	-894.367	MIN_surface_methoxy_species_O1_1b	-880.751
TS_sms_formation_stepwise_O1_1c	-894.916	MIN_surface_methoxy_species_O1_1c	-880.645
TS_sms_formation_stepwise_O1_2a	-894.488	MIN_surface_methoxy_species_O1_2a	-880.714
TS_sms_formation_stepwise_O1_2b	-894.497	MIN_surface_methoxy_species_O1_2b	-880.497
TS_sms_formation_stepwise_O1_3a	-894.65	MIN_surface_methoxy_species_O1_3a	-880.519
TS_sms_formation_stepwise_O1_4a	-894.336	MIN_surface_methoxy_species_O1_4a	-880.444
TS_sms_formation_stepwise_O1_4b	-894.34	MIN_surface_methoxy_species_O1_4b	-880.402
TS_sms_formation_stepwise_O1_4c	-894.461	MIN_surface_methoxy_species_O1_4c	-880.409
TS_sms_formation_stepwise_O1_5a	-894.306	MIN_surface_methoxy_species_O1_5a	-880.383
TS_sms_formation_stepwise_O1_6	-892.609	MIN_surface_methoxy_species_O1_6	-878.704
TS_sms_formation_stepwise_O1_with_MeOH_on_2nd_site_1a	-925.885	MIN_NH3_adsorption_O1_1a	-886.032
TS_sms_formation_stepwise_O1_with_MeOH_on_2nd_site_1b	-925.481	MIN_NH3_adsorption_O1_1b	-885.325
TS_sms_formation_stepwise_O1_with_MeOH_on_2nd_site_1c	-926.121	MIN_NH3_adsorption_O1_1c	-886.063
TS_sms_formation_stepwise_O1_with_MeOH_on_2nd_site_2a	-925.847	MIN_NH3_adsorption_O1_2a	-885.63
TS_sms_formation_stepwise_O1_with_MeOH_on_2nd_site_2b	-925.902	MIN_NH3_adsorption_O1_2b	-885.624
TS_sms_formation_stepwise_O1_with_MeOH_on_2nd_site_3a	-926.079	MIN_NH3_adsorption_O1_3a	-885.738
TS_sms_formation_stepwise_O1_with_MeOH_on_2nd_site_4a	-925.766	MIN_NH3_adsorption_O1_4a	-885.475
TS_sms_formation_stepwise_O1_with_MeOH_on_2nd_site_4b	-925.756	MIN_NH3_adsorption_O1_4b	-885.539
TS_sms_formation_stepwise_O1_with_MeOH_on_2nd_site_4c	-925.908	MIN_NH3_adsorption_O1_4c	-885.596
TS_sms_formation_stepwise_O1_with_MeOH_on_2nd_site_5a	-925.715	MIN_NH3_adsorption_O1_5a	-885.444
TS_sms_formation_stepwise_O2_1a	-894.841	MIN_NH3_adsorption_O1_6	-883.732
TS_sms_formation_stepwise_O2_1b	-894.832	MIN_clean_sites_structure_1a	-864.75
TS_sms_formation_stepwise_O2_1c	-894.893	MIN_clean_sites_structure_1b	-864.648
TS_sms_formation_stepwise_O2_2a	-894.467	MIN_clean_sites_structure_1c	-864.56
TS_sms_formation_stepwise_O2_2b	-894.504	MIN_clean_sites_structure_2a	-864.576
TS_sms_formation_stepwise_O2_3a	-894.553	MIN_clean_sites_structure_2b	-864.444
TS_sms_formation_stepwise_O2_4a	-894.483	MIN_clean_sites_structure_3a	-864.426
TS_sms_formation_stepwise_O2_4b	-894.463	MIN_clean_sites_structure_4a	-864.352
TS_sms_formation_stepwise_O2_4c	-894.452	MIN_clean_sites_structure_4b	-864.291
TS_sms_formation_stepwise_O2_5a	-894.437	MIN_clean_sites_structure_4c	-864.371
TS_sms_formation_stepwise_O2_6	-892.676	MIN_clean_sites_structure_5a	-864.292
TS_sms_formation_stepwise_O3_1a	-894.731	MIN_clean_sites_structure_6	-862.601
TS_sms_formation_stepwise_O3_1b	-894.802	MIN_dme_adsorption_O1_1a	-912.298
TS_sms_formation_stepwise_O3_1c	-894.325	MIN_dme_adsorption_O1_1b	-912.122
TS_sms_formation_stepwise_O3_2a	-894.356	MIN_dme_adsorption_O1_1c	-912.229
TS_sms_formation_stepwise_O3_2b	-894.395	MIN_dme_adsorption_O1_2a	-912.155
TS_sms_formation_stepwise_O3_3a	-894.438	MIN_dme_adsorption_O1_2b	-912.04
TS_sms_formation_stepwise_O3_4a	-894.394	MIN_dme_adsorption_O1_3a	-912.054
TS_sms_formation_stepwise_O3_4b	-894.333	MIN_dme_adsorption_O1_4a	-911.955
TS_sms_formation_stepwise_O3_4c	-894.325	MIN_dme_adsorption_O1_4b	-911.916
TS_sms_formation_stepwise_O3_5a	-894.306	MIN_dme_adsorption_O1_4c	-911.961
TS_sms_formation_stepwise_O3_6	-892.585	MIN_dme_adsorption_O1_5a	-911.907
MIN_methanol_adsorption_O1_with_MeOH_on_2nd_site_1a	-927.27	MIN_dme_adsorption_O1_6	-910.215
MIN_methanol_adsorption_O1_with_MeOH_on_2nd_site_1b	-927.274	MIN_methanol_adsorption_O1_1a	-896.238
MIN_methanol_adsorption_O1_with_MeOH_on_2nd_site_1c	-927.526	MIN_methanol_adsorption_O1_1b	-895.861
MIN_methanol_adsorption_O1_with_MeOH_on_2nd_site_2a	-927.332	MIN_methanol_adsorption_O1_1c	-896.303
MIN_methanol_adsorption_O1_with_MeOH_on_2nd_site_2b	-927.229	MIN_methanol_adsorption_O1_2a	-895.969
MIN_methanol_adsorption_O1_with_MeOH_on_2nd_site_3a	-927.343	MIN_methanol_adsorption_O1_2b	-895.862
MIN_methanol_adsorption_O1_with_MeOH_on_2nd_site_4a	-927.219	MIN_methanol_adsorption_O1_3a	-895.986
MIN_methanol_adsorption_O1_with_MeOH_on_2nd_site_4b	-927.178	MIN_methanol_adsorption_O1_4a	-895.784
MIN_methanol_adsorption_O1_with_MeOH_on_2nd_site_4c	-927.203	MIN_methanol_adsorption_O1_4b	-895.745
MIN_methanol_adsorption_O1_with_MeOH_on_2nd_site_5a	-927.117	MIN_methanol_adsorption_O1_4c	-895.807
MIN_surface_methoxy_species_O1_with_MeOH_on_2nd_site_1a	-911.967	MIN_methanol_adsorption_O1_5a	-895.711
MIN_surface_methoxy_species_O1_with_MeOH_on_2nd_site_1b	-912.157	MIN_methanol_adsorption_O1_6	-894.039
MIN_surface_methoxy_species_O1_with_MeOH_on_2nd_site_1c	-911.965		
MIN_surface_methoxy_species_O1_with_MeOH_on_2nd_site_2a	-912.076		
MIN_surface_methoxy_species_O1_with_MeOH_on_2nd_site_2b	-911.866		
MIN_surface_methoxy_species_O1_with_MeOH_on_2nd_site_3a	-911.915		
MIN_surface_methoxy_species_O1_with_MeOH_on_2nd_site_4a	-911.885		
MIN_surface_methoxy_species_O1_with_MeOH_on_2nd_site_4b	-911.886		
MIN_surface_methoxy_species_O1_with_MeOH_on_2nd_site_4c	-911.824		
MIN_surface_methoxy_species_O1_with_MeOH_on_2nd_site_5a	-911.833		
MIN_methanol_adsorption_on_surface_methoxy_species_O1_6	-909.413		

Table C.4: Computed reaction and activation energies according to the nomenclature introduced in the main text.

State	Energy (kJ/mol)	State	Energy (kJ/mol)
MIN_clean_sites_structure_1a	-41.93	TS_sms_formation_stepwise_O1_with_MeOH_on_2nd_site_1a	17.30
MIN_clean_sites_structure_1b	-32.05	TS_sms_formation_stepwise_O1_with_MeOH_on_2nd_site_1b	79.93
MIN_clean_sites_structure_1c	-23.53	TS_sms_formation_stepwise_O1_with_MeOH_on_2nd_site_1c	-11.77
MIN_clean_sites_structure_2a	-25.11	TS_sms_formation_stepwise_O1_with_MeOH_on_2nd_site_2a	33.13
MIN_clean_sites_structure_2b	-12.38	TS_sms_formation_stepwise_O1_with_MeOH_on_2nd_site_2b	9.33
MIN_clean_sites_structure_3a	-10.59	TS_sms_formation_stepwise_O1_with_MeOH_on_2nd_site_3a	-7.98
MIN_clean_sites_structure_4a	-3.50	TS_sms_formation_stepwise_O1_with_MeOH_on_2nd_site_4a	23.85
MIN_clean_sites_structure_4b	2.41	TS_sms_formation_stepwise_O1_with_MeOH_on_2nd_site_4b	26.17
MIN_clean_sites_structure_4c	-5.33	TS_sms_formation_stepwise_O1_with_MeOH_on_2nd_site_4c	14.35
MIN_clean_sites_structure_5a	2.33	TS_sms_formation_stepwise_O1_with_MeOH_on_2nd_site_5a	22.50
MIN_clean_sites_structure_6	0.00	TS_sms_formation_stepwise_O1_intrinsic_1a	130.54
MIN_NH3_adsorption_O1_1a	-169.95	TS_sms_formation_stepwise_O1_intrinsic_1b	144.18
MIN_NH3_adsorption_O1_1b	-111.65	TS_sms_formation_stepwise_O1_intrinsic_1c	133.79
MIN_NH3_adsorption_O1_1c	-191.34	TS_sms_formation_stepwise_O1_intrinsic_2a	142.89
MIN_NH3_adsorption_O1_2a	-148.03	TS_sms_formation_stepwise_O1_intrinsic_2b	131.64
MIN_NH3_adsorption_O1_2b	-160.17	TS_sms_formation_stepwise_O1_intrinsic_3a	128.91
MIN_NH3_adsorption_O1_3a	-172.91	TS_sms_formation_stepwise_O1_intrinsic_4a	139.71
MIN_NH3_adsorption_O1_4a	-154.69	TS_sms_formation_stepwise_O1_intrinsic_4b	135.57
MIN_NH3_adsorption_O1_4b	-166.79	TS_sms_formation_stepwise_O1_intrinsic_4c	129.90
MIN_NH3_adsorption_O1_4c	-164.55	TS_sms_formation_stepwise_O1_intrinsic_5a	135.56
MIN_NH3_adsorption_O1_5a	-157.52	TS_sms_formation_stepwise_O1_intrinsic_6	137.97
MIN_NH3_adsorption_O1_6	-155.40	TS_sms_formation_stepwise_O2_intrinsic_1a	134.81
MIN_methanol_adsorption_O1_1a	-121.00	TS_sms_formation_stepwise_O2_intrinsic_1b	99.34
MIN_methanol_adsorption_O1_1b	-94.57	TS_sms_formation_stepwise_O2_intrinsic_1c	136.06
MIN_methanol_adsorption_O1_1c	-145.67	TS_sms_formation_stepwise_O2_intrinsic_2a	144.86
MIN_methanol_adsorption_O1_2a	-111.86	TS_sms_formation_stepwise_O2_intrinsic_2b	130.94
MIN_methanol_adsorption_O1_2b	-114.25	TS_sms_formation_stepwise_O2_intrinsic_3a	138.26
MIN_methanol_adsorption_O1_3a	-128.09	TS_sms_formation_stepwise_O2_intrinsic_4a	125.55
MIN_methanol_adsorption_O1_4a	-115.65	TS_sms_formation_stepwise_O2_intrinsic_4b	123.64
MIN_methanol_adsorption_O1_4b	-117.76	TS_sms_formation_stepwise_O2_intrinsic_4c	130.77
MIN_methanol_adsorption_O1_4c	-116.08	TS_sms_formation_stepwise_O2_intrinsic_5a	122.89
MIN_methanol_adsorption_O1_5a	-114.43	TS_sms_formation_stepwise_O2_intrinsic_6	131.55
MIN_methanol_adsorption_O1_6	-116.18	TS_sms_formation_stepwise_O3_intrinsic_1a	145.33
TS_sms_formation_stepwise_O1_1a	9.54	TS_sms_formation_stepwise_O3_intrinsic_1b	102.19
TS_sms_formation_stepwise_O1_1b	49.62	TS_sms_formation_stepwise_O3_intrinsic_1c	190.84
TS_sms_formation_stepwise_O1_2a	-11.88	TS_sms_formation_stepwise_O3_intrinsic_2a	155.59
TS_sms_formation_stepwise_O1_2b	31.03	TS_sms_formation_stepwise_O3_intrinsic_2b	141.45
TS_sms_formation_stepwise_O1_2b	17.39	TS_sms_formation_stepwise_O3_intrinsic_3a	149.44
TS_sms_formation_stepwise_O1_3a	0.82	TS_sms_formation_stepwise_O3_intrinsic_4a	134.16
TS_sms_formation_stepwise_O1_4a	24.06	TS_sms_formation_stepwise_O3_intrinsic_4b	136.17
TS_sms_formation_stepwise_O1_4b	17.81	TS_sms_formation_stepwise_O3_intrinsic_4c	143.06
TS_sms_formation_stepwise_O1_4c	13.82	TS_sms_formation_stepwise_O3_intrinsic_5a	135.52
TS_sms_formation_stepwise_O1_5a	21.13	TS_sms_formation_stepwise_O3_intrinsic_6	140.28
TS_sms_formation_stepwise_O1_6	21.78	MIN_surface_methoxy_species_O1_and_H2O(g)_1a	-13.85
TS_sms_formation_stepwise_O2_1a	13.81	MIN_surface_methoxy_species_O1_and_H2O(g)_1b	-8.99
TS_sms_formation_stepwise_O2_1b	4.77	MIN_surface_methoxy_species_O1_and_H2O(g)_1c	-7.35
TS_sms_formation_stepwise_O2_1c	-9.61	MIN_surface_methoxy_species_O1_and_H2O(g)_2a	-12.39
TS_sms_formation_stepwise_O2_2a	33.01	MIN_surface_methoxy_species_O1_and_H2O(g)_2b	-4.15
TS_sms_formation_stepwise_O2_2b	16.69	MIN_surface_methoxy_species_O1_and_H2O(g)_3a	-8.08
TS_sms_formation_stepwise_O2_3a	10.17	MIN_surface_methoxy_species_O1_and_H2O(g)_4a	-7.98
TS_sms_formation_stepwise_O2_4a	9.89	MIN_surface_methoxy_species_O1_and_H2O(g)_4b	-9.81
TS_sms_formation_stepwise_O2_4b	5.88	MIN_surface_methoxy_species_O1_and_H2O(g)_4c	-2.73
TS_sms_formation_stepwise_O2_4c	14.69	MIN_surface_methoxy_species_O1_and_H2O(g)_5a	-7.88
TS_sms_formation_stepwise_O2_5a	8.46	MIN_surface_methoxy_species_O1_and_H2O(g)_6	-8.93
TS_sms_formation_stepwise_O2_6	15.37	MIN_surface_methoxy_species_O1_with_MeOH_on_2nd_site_1a	-94.00
TS_sms_formation_stepwise_O3_1a	24.33	MIN_surface_methoxy_species_O1_with_MeOH_on_2nd_site_1b	-122.18
TS_sms_formation_stepwise_O3_1b	7.63	MIN_surface_methoxy_species_O1_with_MeOH_on_2nd_site_1c	-112.20
TS_sms_formation_stepwise_O3_1c	45.16	MIN_surface_methoxy_species_O1_with_MeOH_on_2nd_site_2a	-121.28
TS_sms_formation_stepwise_O3_2a	43.74	MIN_surface_methoxy_species_O1_with_MeOH_on_2nd_site_2b	-113.76
TS_sms_formation_stepwise_O3_2b	27.20	MIN_surface_methoxy_species_O1_with_MeOH_on_2nd_site_3a	-120.30
TS_sms_formation_stepwise_O3_3a	21.35	MIN_surface_methoxy_species_O1_with_MeOH_on_2nd_site_4a	-124.47
TS_sms_formation_stepwise_O3_4a	18.51	MIN_surface_methoxy_species_O1_with_MeOH_on_2nd_site_4b	-130.49
TS_sms_formation_stepwise_O3_4b	18.41	MIN_surface_methoxy_species_O1_with_MeOH_on_2nd_site_4c	-116.75
TS_sms_formation_stepwise_O3_4c	26.98	MIN_surface_methoxy_species_O1_with_MeOH_on_2nd_site_5a	-125.31
TS_sms_formation_stepwise_O3_5a	21.09	MIN_methanol_adsorption_on_surface_methoxy_species_O1_6	-54.89
TS_sms_formation_stepwise_O3_6	24.10	MIN_methanol_adsorption_O1_with_MeOH_on_2nd_site_1a	-198.11
TS_dme_formation_stepwise_O1_1a	-1.89	MIN_methanol_adsorption_O1_with_MeOH_on_2nd_site_1b	-208.38
TS_dme_formation_stepwise_O1_1b	29.18	MIN_methanol_adsorption_O1_with_MeOH_on_2nd_site_1c	-241.21
TS_dme_formation_stepwise_O1_1c	-12.74	MIN_methanol_adsorption_O1_with_MeOH_on_2nd_site_2a	-220.90
TS_dme_formation_stepwise_O1_2a	7.93	MIN_methanol_adsorption_O1_with_MeOH_on_2nd_site_2b	-223.69
TS_dme_formation_stepwise_O1_2b	-3.80	MIN_methanol_adsorption_O1_with_MeOH_on_2nd_site_3a	-236.47
TS_dme_formation_stepwise_O1_3a	-10.41	MIN_methanol_adsorption_O1_with_MeOH_on_2nd_site_4a	-231.60
TS_dme_formation_stepwise_O1_4a	5.46	MIN_methanol_adsorption_O1_with_MeOH_on_2nd_site_4b	-233.56
TS_dme_formation_stepwise_O1_4b	2.07	MIN_methanol_adsorption_O1_with_MeOH_on_2nd_site_4c	-228.27
TS_dme_formation_stepwise_O1_4c	-9.76	MIN_methanol_adsorption_O1_with_MeOH_on_2nd_site_5a	-227.63
TS_dme_formation_stepwise_O1_5a	1.74	MIN_methanol_coadsorbed_6	-155.93
TS_dme_formation_stepwise_O1_6	1.77	MIN_dme_adsorption_O1_1a	-125.90
TS_dme_formation_concerted_1a	-82.51	MIN_dme_adsorption_O1_1b	-118.78
TS_dme_formation_concerted_1b	-81.72	MIN_dme_adsorption_O1_1c	-137.65
TS_dme_formation_concerted_1c	-102.70	MIN_dme_adsorption_O1_2a	-128.96
TS_dme_formation_concerted_2a	-51.50	MIN_dme_adsorption_O1_2b	-130.57
TS_dme_formation_concerted_2b	-75.82	MIN_dme_adsorption_O1_3a	-133.68
TS_dme_formation_concerted_3a	-86.55	MIN_dme_adsorption_O1_4a	-131.18
TS_dme_formation_concerted_4a	-68.16	MIN_dme_adsorption_O1_4b	-133.35
TS_dme_formation_concerted_4b	-78.71	MIN_dme_adsorption_O1_4c	-129.98
TS_dme_formation_concerted_4c	-78.91	MIN_dme_adsorption_O1_5a	-132.44
TS_dme_formation_concerted_5a	-79.87	MIN_dme_adsorption_O1_6	-132.23
TS_dme_formation_concerted_6	-71.44		

D Trends in reactivity due to changing the choice of T-site in H-ZSM-5

D.1 Clean sites stabilities, ammonia adsorption data and choices of oxygen

Ammonia was adsorbed and clean sites structures were calculated at all possible $12 \times 4 = 48$ possible oxygens. Where the factor of 12 comes from the number of different T-site choices and the factor of 4 comes from the 4 different oxygens for each T-site. Figure D.1 presents the ammonia adsorption energies and clean sites structures for the structures which were deemed to be reasonably stable, acidic and also accessible. From these 24 structures the oxygen with the most stable proton binding for a given T-site choice was taken in all further calculations. Table 7.1 presents 12 choices of oxygen location used also their stabilities. Table D.1 gives more information about the accessibility of these 12 oxygens from the pores of MFI.

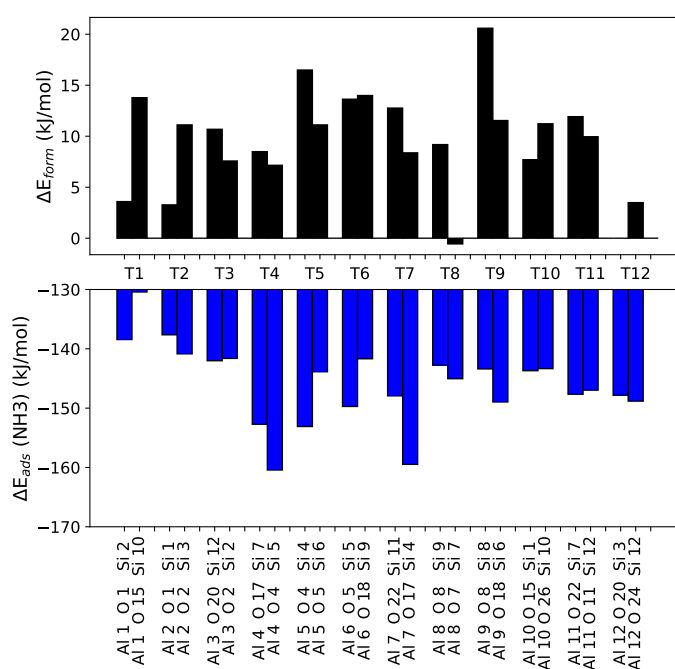


Figure D.1: Cleans sites energies referenced to the most stable location at T12 and NH3 adsorption data for all oxygens which were deemed to be both stable and accessible.

Table D.1: Locations of different Al-substituted T sites in H-ZSM-5. Sites which can be accessed via both the straight and sinusoidal channel are labelled as intersection.

T site	Al location	Choice of T site	Oxygen accessible from
T1	Intersection	Al-1-O1-Si-2	Straight and Sinusoidal
T2	Intersection	Al-2-O-1-Si-1	Straight and Sinusoidal
T3	Intersection	Al-3-O-2-Si-2	Straight and Sinusoidal
T4	Sinusoidal	Al-4-O-4-Si-5	Sinusoidal
T5	Intersection	Al-5-O-5-Si-6	Straight and Sinusoidal
T6	Intersection	Al-6-O-5-Si-5	Straight and Sinusoidal
T7	Intersection	Al-7-O-17-Si 4	Sinusoidal
T8	Straight	Al-8-O-7-Si-7	Straight and Sinusoidal
T9	Intersection	Al-9-O-18-Si 6	Straight and Sinusoidal
T10	Sinusoidal	Al-10-O-15-Si 1	Straight and Sinusoidal
T11	Straight	Al-11-O-11-Si-12	Straight and Sinusoidal
T12	Intersection	Al-12-O-20-Si-3	Straight and Sinusoidal

D.2 Methodology used for transition state calculations

For each calculation at a given oxygen different transition state isomers were automatically generated so as to align the transition state along the different pore directions e.g. up along the straight pore, down along the straight pore, left along the sinusoidal pore and right along the sinusoidal pore. Figure D.2 shows the spread in different energies achieved with the most stable isomer always been taken when any results are plotted in the main text.

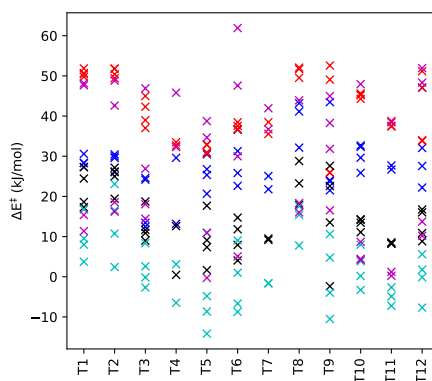


Figure D.2: Scatter graph of transition state energies of all transition states calculated. Only the most stable transition state for a given reaction and T-site is presented in the main text.

D.3 Correlations of the barriers against ethene and ammonia adsorption

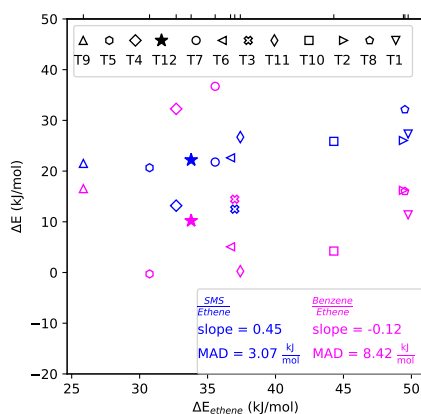


Figure D.3: Transition state energies of stepwise surface methoxy species formation (blue) and benzene (magenta) methylation via a SMS compared to that of ethene.

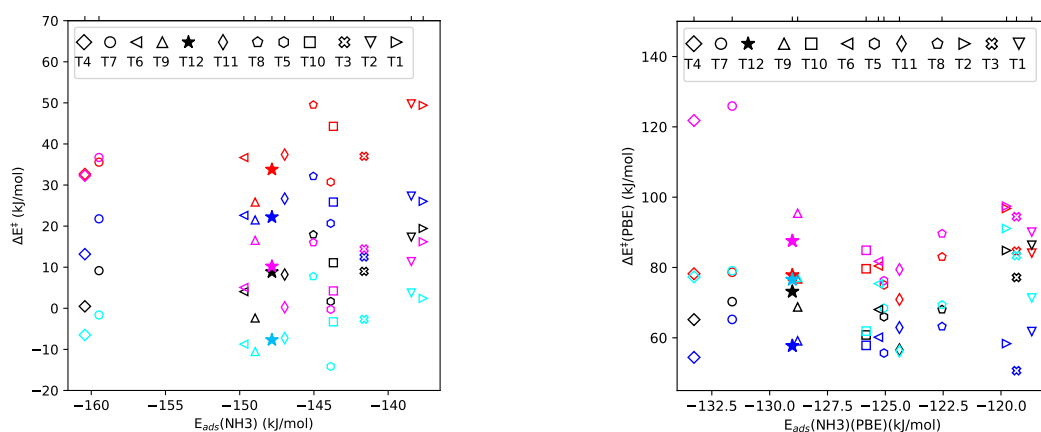


Figure D.4: Correlation of transition state energies with ammonia adsorption with and without the D3 dispersion correction.

Table D.2: Computed total energies.

State	Energy (eV)	State	Energy (eV)
MIN_NH3_adsorption_Al1.O.1.Si.2	-2322.607	TS_benzene_methylation_Al1.O.1.Si.2	-2393.851
MIN_NH3_adsorption_Al2.O.1.Si.1	-2322.602	TS_benzene_methylation_Al2.O.1.Si.1	-2393.822
MIN_NH3_adsorption_Al3.O.2.Si.2	-2322.599	TS_benzene_methylation_Al3.O.2.Si.2	-2393.759
MIN_NH3_adsorption_Al4.O.4.Si.5	-2322.798	TS_benzene_methylation_Al4.O.4.Si.5	-2393.574
MIN_NH3_adsorption_Al5.O.5.Si.6	-2322.585	TS_benzene_methylation_Al5.O.5.Si.6	-2393.832
MIN_NH3_adsorption_Al6.O.5.Si.5	-2322.62	TS_benzene_methylation_Al6.O.5.Si.5	-2393.743
MIN_NH3_adsorption_Al7.O.17.Si.4	-2322.776	TS_benzene_methylation_Al7.O.17.Si.4	-2393.544
MIN_NH3_adsorption_Al8.O.7.Si.7	-2322.719	TS_benzene_methylation_Al8.O.7.Si.7	-2393.856
MIN_NH3_adsorption_Al9.O.18.Si.6	-2322.634	TS_benzene_methylation_Al9.O.18.Si.6	-2393.679
MIN_NH3_adsorption_Al10.O.15.Si.1	-2322.619	TS_benzene_methylation_Al10.O.15.Si.1	-2393.871
MIN_NH3_adsorption_Al11.O.11.Si.12	-2322.63	TS_benzene_methylation_Al11.O.11.Si.12	-2393.84
MIN_NH3_adsorption_Al12.O.20.Si.3	-2322.742	TS_benzene_methylation_Al12.O.20.Si.3	-2393.888
MIN_clean_sites_structure_Al1.O.1.Si.2	-2301.652	TS_ethylene_methylation_Al1.O.1.Si.2	-2349.324
MIN_clean_sites_structure_Al2.O.1.Si.1	-2301.656	TS_ethylene_methylation_Al2.O.1.Si.1	-2349.348
MIN_clean_sites_structure_Al3.O.2.Si.2	-2301.611	TS_ethylene_methylation_Al3.O.2.Si.2	-2349.396
MIN_clean_sites_structure_Al4.O.4.Si.5	-2301.615	TS_ethylene_methylation_Al4.O.4.Si.5	-2349.441
MIN_clean_sites_structure_Al5.O.5.Si.6	-2301.574	TS_ethylene_methylation_Al5.O.5.Si.6	-2349.382
MIN_clean_sites_structure_Al6.O.5.Si.5	-2301.548	TS_ethylene_methylation_Al6.O.5.Si.5	-2349.286
MIN_clean_sites_structure_Al7.O.17.Si.4	-2301.603	TS_ethylene_methylation_Al7.O.17.Si.4	-2349.426
MIN_clean_sites_structure_Al8.O.7.Si.7	-2301.695	TS_ethylene_methylation_Al8.O.7.Si.7	-2349.379
MIN_clean_sites_structure_Al9.O.18.Si.6	-2301.57	TS_ethylene_methylation_Al9.O.18.Si.6	-2349.453
MIN_clean_sites_structure_Al10.O.15.Si.1	-2301.61	TS_ethylene_methylation_Al10.O.15.Si.1	-2349.327
MIN_clean_sites_structure_Al11.O.11.Si.12	-2301.586	TS_ethylene_methylation_Al11.O.11.Si.12	-2349.326
MIN_clean_sites_structure_Al12.O.20.Si.3	-2301.69	TS_ethylene_methylation_Al12.O.20.Si.3	-2349.514
MIN_methanol_adsorption_Al1.O.1.Si.2	-2333.084	TS_propylene_methylation_Al1.O.1.Si.2	-2366.386
MIN_methanol_adsorption_Al2.O.1.Si.1	-2333.09	TS_propylene_methylation_Al2.O.1.Si.1	-2366.385
MIN_methanol_adsorption_Al3.O.2.Si.2	-2333.019	TS_propylene_methylation_Al3.O.2.Si.2	-2366.412
MIN_methanol_adsorption_Al4.O.4.Si.5	-2333.122	TS_propylene_methylation_Al4.O.4.Si.5	-2366.5
MIN_methanol_adsorption_Al5.O.5.Si.6	-2333.055	TS_propylene_methylation_Al5.O.5.Si.6	-2366.409
MIN_methanol_adsorption_Al6.O.5.Si.5	-2333.033	TS_propylene_methylation_Al6.O.5.Si.5	-2366.35
MIN_methanol_adsorption_Al7.O.17.Si.4	-2333.123	TS_propylene_methylation_Al7.O.17.Si.4	-2366.425
MIN_methanol_adsorption_Al8.O.7.Si.7	-2333.139	TS_propylene_methylation_Al8.O.7.Si.7	-2366.432
MIN_methanol_adsorption_Al9.O.18.Si.6	-2333.042	TS_propylene_methylation_Al9.O.18.Si.6	-2366.471
MIN_methanol_adsorption_Al10.O.15.Si.1	-2333.118	TS_propylene_methylation_Al10.O.15.Si.1	-2366.396
MIN_methanol_adsorption_Al11.O.11.Si.12	-2332.999	TS_propylene_methylation_Al11.O.11.Si.12	-2366.354
MIN_methanol_adsorption_Al12.O.20.Si.3	-2333.206	TS_propylene_methylation_Al12.O.20.Si.3	-2366.498
MIN_surface_methoxy_species_Al1.O.1.Si.2	-2317.854	TS_sms_formation_Al1.O.1.Si.2	-2331.602
MIN_surface_methoxy_species_Al2.O.1.Si.1	-2317.875	TS_sms_formation_Al2.O.1.Si.1	-2331.619
MIN_surface_methoxy_species_Al3.O.2.Si.2	-2317.794	TS_sms_formation_Al3.O.2.Si.2	-2331.715
MIN_surface_methoxy_species_Al4.O.4.Si.5	-2317.794	TS_sms_formation_Al4.O.4.Si.5	-2331.712
MIN_surface_methoxy_species_Al5.O.5.Si.6	-2317.715	TS_sms_formation_Al5.O.5.Si.6	-2331.594
MIN_surface_methoxy_species_Al6.O.5.Si.5	-2317.681	TS_sms_formation_Al6.O.5.Si.5	-2331.547
MIN_surface_methoxy_species_Al7.O.17.Si.4	-2317.809	TS_sms_formation_Al7.O.17.Si.4	-2331.61
MIN_surface_methoxy_species_Al8.O.7.Si.7	-2317.907	TS_sms_formation_Al8.O.7.Si.7	-2331.595
MIN_surface_methoxy_species_Al9.O.18.Si.6	-2317.736	TS_sms_formation_Al9.O.18.Si.6	-2331.58
MIN_surface_methoxy_species_Al10.O.15.Si.1	-2317.8	TS_sms_formation_Al10.O.15.Si.1	-2331.575
MIN_surface_methoxy_species_Al11.O.11.Si.12	-2317.728	TS_sms_formation_Al11.O.11.Si.12	-2331.543
MIN_surface_methoxy_species_Al12.O.20.Si.3	-2317.879	TS_sms_formation_Al12.O.20.Si.3	-2331.693
TS_1-butene_methylation_Al1.O.1.Si.2	-2383.078		
TS_1-butene_methylation_Al2.O.1.Si.1	-2383.112		
TS_1-butene_methylation_Al3.O.2.Si.2	-2383.084		
TS_1-butene_methylation_Al4.O.4.Si.5	-2383.124		
TS_1-butene_methylation_Al5.O.5.Si.6	-2383.124		
TS_1-butene_methylation_Al6.O.5.Si.5	-2383.034		
TS_1-butene_methylation_Al7.O.17.Si.4	-2383.089		
TS_1-butene_methylation_Al8.O.7.Si.7	-2383.089		
TS_1-butene_methylation_Al9.O.18.Si.6	-2383.107		
TS_1-butene_methylation_Al10.O.15.Si.1	-2383.097		
TS_1-butene_methylation_Al11.O.11.Si.12	-2383.066		
TS_1-butene_methylation_Al12.O.20.Si.3	-2383.221		

Table D.3: Computed reaction energies.

State	Energy (kJ/mol)	State	Energy (kJ/mol)
MIN_clean_sites_structure_Al1.O.1.Si.2	3.59	TS_1-butene_methylation_Al1.O.1.Si.2	3.73
MIN_clean_sites_structure_Al2.O.1.Si.1	3.27	TS_1-butene_methylation_Al2.O.1.Si.1	2.42
MIN_clean_sites_structure_Al3.O.2.Si.2	7.57	TS_1-butene_methylation_Al3.O.2.Si.2	-2.67
MIN_clean_sites_structure_Al4.O.4.Si.5	7.15	TS_1-butene_methylation_Al4.O.4.Si.5	-6.48
MIN_clean_sites_structure_Al5.O.5.Si.6	11.11	TS_1-butene_methylation_Al5.O.5.Si.6	-14.16
MIN_clean_sites_structure_Al6.O.5.Si.5	13.63	TS_1-butene_methylation_Al6.O.5.Si.5	-8.73
MIN_clean_sites_structure_Al7.O.17.Si.4	8.37	TS_1-butene_methylation_Al7.O.17.Si.4	-1.63
MIN_clean_sites_structure_Al8.O.7.Si.7	-0.56	TS_1-butene_methylation_Al8.O.7.Si.7	7.77
MIN_clean_sites_structure_Al9.O.18.Si.6	11.54	TS_1-butene_methylation_Al9.O.18.Si.6	-10.52
MIN_clean_sites_structure_Al10.O.15.Si.1	7.7	TS_1-butene_methylation_Al10.O.15.Si.1	-3.29
MIN_clean_sites_structure_Al11.O.11.Si.12	9.95	TS_1-butene_methylation_Al11.O.11.Si.12	-7.24
MIN_clean_sites_structure_Al12.O.20.Si.3	0.0	TS_1-butene_methylation_Al12.O.20.Si.3	-7.69
MIN_NH3_adsorption_Al1.O.1.Si.2	-138.44	TS_benzene_methylation_Al1.O.1.Si.2	11.37
MIN_NH3_adsorption_Al2.O.1.Si.1	-137.64	TS_benzene_methylation_Al2.O.1.Si.1	16.2
MIN_NH3_adsorption_Al3.O.2.Si.2	-141.62	TS_benzene_methylation_Al3.O.2.Si.2	14.45
MIN_NH3_adsorption_Al4.O.4.Si.5	-160.43	TS_benzene_methylation_Al4.O.4.Si.5	32.27
MIN_NH3_adsorption_Al5.O.5.Si.6	-143.87	TS_benzene_methylation_Al5.O.5.Si.6	-0.28
MIN_NH3_adsorption_Al6.O.5.Si.5	-149.72	TS_benzene_methylation_Al6.O.5.Si.5	5.07
MIN_NH3_adsorption_Al7.O.17.Si.4	-159.48	TS_benzene_methylation_Al7.O.17.Si.4	36.71
MIN_NH3_adsorption_Al8.O.7.Si.7	-145.04	TS_benzene_methylation_Al8.O.7.Si.7	16.02
MIN_NH3_adsorption_Al9.O.18.Si.6	-148.96	TS_benzene_methylation_Al9.O.18.Si.6	16.54
MIN_NH3_adsorption_Al10.O.15.Si.1	-143.69	TS_benzene_methylation_Al10.O.15.Si.1	4.23
MIN_NH3_adsorption_Al11.O.11.Si.12	-146.97	TS_benzene_methylation_Al11.O.11.Si.12	0.25
MIN_NH3_adsorption_Al12.O.20.Si.3	-147.83	TS_benzene_methylation_Al12.O.20.Si.3	10.21
TS_sms_formation_Al1.O.1.Si.2	27.31	MIN_methanol_adsorption_Al1.O.1.Si.2	-115.65
TS_sms_formation_Al2.O.1.Si.1	26.03	MIN_methanol_adsorption_Al2.O.1.Si.1	-115.84
TS_sms_formation_Al3.O.2.Si.2	12.49	MIN_methanol_adsorption_Al3.O.2.Si.2	-113.3
TS_sms_formation_Al4.O.4.Si.5	13.18	MIN_methanol_adsorption_Al4.O.4.Si.5	-122.85
TS_sms_formation_Al5.O.5.Si.6	20.66	MIN_methanol_adsorption_Al5.O.5.Si.6	-120.33
TS_sms_formation_Al6.O.5.Si.5	22.62	MIN_methanol_adsorption_Al6.O.5.Si.5	-120.74
TS_sms_formation_Al7.O.17.Si.4	21.78	MIN_methanol_adsorption_Al7.O.17.Si.4	-124.21
TS_sms_formation_Al8.O.7.Si.7	32.14	MIN_methanol_adsorption_Al8.O.7.Si.7	-116.81
TS_sms_formation_Al9.O.18.Si.6	21.51	MIN_methanol_adsorption_Al9.O.18.Si.6	-119.54
TS_sms_formation_Al10.O.15.Si.1	25.86	MIN_methanol_adsorption_Al10.O.15.Si.1	-122.97
TS_sms_formation_Al11.O.11.Si.12	26.7	MIN_methanol_adsorption_Al11.O.11.Si.12	-113.76
TS_sms_formation_Al12.O.20.Si.3	22.2	MIN_methanol_adsorption_Al12.O.20.Si.3	-123.8
TS_ethylene_methylation_Al1.O.1.Si.2	49.76	TS_sms_formation_intrinsic_Al1.O.1.Si.2	142.96
TS_ethylene_methylation_Al2.O.1.Si.1	49.41	TS_sms_formation_intrinsic_Al2.O.1.Si.1	141.87
TS_ethylene_methylation_Al3.O.2.Si.2	37.0	TS_sms_formation_intrinsic_Al3.O.2.Si.2	125.79
TS_ethylene_methylation_Al4.O.4.Si.5	32.69	TS_sms_formation_intrinsic_Al4.O.4.Si.5	136.03
TS_ethylene_methylation_Al5.O.5.Si.6	30.73	TS_sms_formation_intrinsic_Al5.O.5.Si.6	140.99
TS_ethylene_methylation_Al6.O.5.Si.5	36.69	TS_sms_formation_intrinsic_Al6.O.5.Si.5	143.36
TS_ethylene_methylation_Al7.O.17.Si.4	35.56	TS_sms_formation_intrinsic_Al7.O.17.Si.4	145.99
TS_ethylene_methylation_Al8.O.7.Si.7	49.52	TS_sms_formation_intrinsic_Al8.O.7.Si.7	148.95
TS_ethylene_methylation_Al9.O.18.Si.6	25.86	TS_sms_formation_intrinsic_Al9.O.18.Si.6	141.05
TS_ethylene_methylation_Al10.O.15.Si.1	44.29	TS_sms_formation_intrinsic_Al10.O.15.Si.1	148.83
TS_ethylene_methylation_Al11.O.11.Si.12	37.41	TS_sms_formation_intrinsic_Al11.O.11.Si.12	140.46
TS_ethylene_methylation_Al12.O.20.Si.3	33.79	TS_sms_formation_intrinsic_Al12.O.20.Si.3	146.0
TS_propylene_methylation_Al1.O.1.Si.2	17.32		
TS_propylene_methylation_Al2.O.1.Si.1	19.43		
TS_propylene_methylation_Al3.O.2.Si.2	8.99		
TS_propylene_methylation_Al4.O.4.Si.5	0.48		
TS_propylene_methylation_Al5.O.5.Si.6	1.67		
TS_propylene_methylation_Al6.O.5.Si.5	4.05		
TS_propylene_methylation_Al7.O.17.Si.4	9.16		
TS_propylene_methylation_Al8.O.7.Si.7	17.94		
TS_propylene_methylation_Al9.O.18.Si.6	-2.36		
TS_propylene_methylation_Al10.O.15.Si.1	11.09		
TS_propylene_methylation_Al11.O.11.Si.12	8.22		
TS_propylene_methylation_Al12.O.20.Si.3	8.83		

List of abbreviations

ARPES	Automated Relaxed Potential Energy Surface Scan
BAS	Brønsted acid site
BJ	Beck-Johnson
BO	Born-Oppenheimer
BFGS	Broyden-Fletcher-Goldfarb-Shanno
CBS	Complete basis set
CI	Configuration interaction
CCSD(T)	Coupled cluster singles, doubles and perturbative triples
CI-NEB	Climbing image nudged elastic band
def2-TZVPP	Karlsruhe basis set valence triple-zeta with two sets of polarisation functions
DFT	Density functional theory
DME	Dimethyl ether
D3	Grimmes' dispersion correction
GD	Gradient descent
HC	Heterogeneous catalysis
HF	Hartree-Fock
HK	Hohenberg-Kohn
HP	Hydrocarbon pool
HVA	Hessian vibrational analysis
KE	Kinetic energy
KS	Kohn-Sham
MAD	Mean absolute deviation
MTH	Methanol-to-hydrocarbons
MA	Methyl acetate
MD	Molecular dynamics
MEP	Minimum energy path
MOT	Molecular orbital theory
MP2	2nd order of the Møller-Plesset perturbation
NEB	Nudged elastic band
NRMSD	Normalised root mean squared deviation
PAW	Projector augmented wave
PBE	Perdew-Burke-Ernzerhof
PES	Potential energy surface
PHF	Post-Hartree-Fock
PHVA	Partial Hessian vibrational analysis
QNM	Quasi-Newton methods
QSM	Quantum statistical mechanics
RP	Reaction path
SCF	Self-consistent field
STO	Slater-type orbital
SMS	Surface methoxy species
TME	Tetramethylethylene
TS	Transition state
TST	Transition state theory
vdW	Van der Waals
VASP	The Vienna Ab initio Simulation Package
ZPE	Zero-point energy

List of publications

- 1) P.N. Plessow, A.Smith, S.Tischer, and F.Studt, "Identification of the reaction sequence of the mto initiation mechanism using ab initio-based kinetics", J. Am. Chem. Soc, vol. 141, no.14, pp. 5908-5915, 2019.
- 2) A.T.Smith, P.N.Plessow, and F.Studt, "Density functional theory calculations of diffusion barriers of organic molecules through the 8-ring of h-ssz-13", Chem. Phys, vol. 541, p. 111033, 2021.
- 3) A.T.Smith, P.N.Plessow, and F.Studt, Trends in the Reactivity of proximate Aluminum Sites in H-SSZ-13. J. Phys. Chem. C, *Accepted* 2021.
- 4) A.T.Smith, P.N.Plessow, and F.Studt, Acidity and Confinement of Aluminum T-site Substitution in H-ZSM-5. *In preparation*.

Acknowledgements

I would like to acknowledge the state of Baden-Württemberg for providing me with access to super computing resources (bwUniCluster and bwUniCluster 2.0 together with bwForCluster JUSTUS and JUSTUS 2). I would also like to acknowledge the financial support I received from the Helmholtz Association. I also thank Prof. Dr. Felix Studt for funding my travels to various conferences and summer schools, both in Germany and abroad. Lastly, thank you to both Prof. Dr. Felix Studt and Dr. Philipp Pleßow for supervising me.

Eidesstattliche Erklärung

Hiermit versichere ich eidesstattlich, dass ich die hier vorgelegte Dissertation selbständig angefertigt habe und keine anderen Quellen und Hilfsmittel genutzt habe als die hier angegebenen. Die wörtlich und inhaltlich übernommenen Stellen wurden als solche kenntlich gemacht. Die Regeln zur Sicherung guter wissenschaftlicher Praxis des Karlsruher Instituts für Technologie (KIT) in der gültigen Fassung wurden beachtet und Primardaten gemäß Abs. A(6) gesichert. Die elektronische Version der Arbeit stimmt mit der schriftlichen überein. Die Arbeit wurde in gleicher oder ähnlicher Form noch keiner anderen Prüfungsbehörde zur Erlangung eines akademischen Grades vorgelegt.

Karlsruhe, den

Ashley Smith